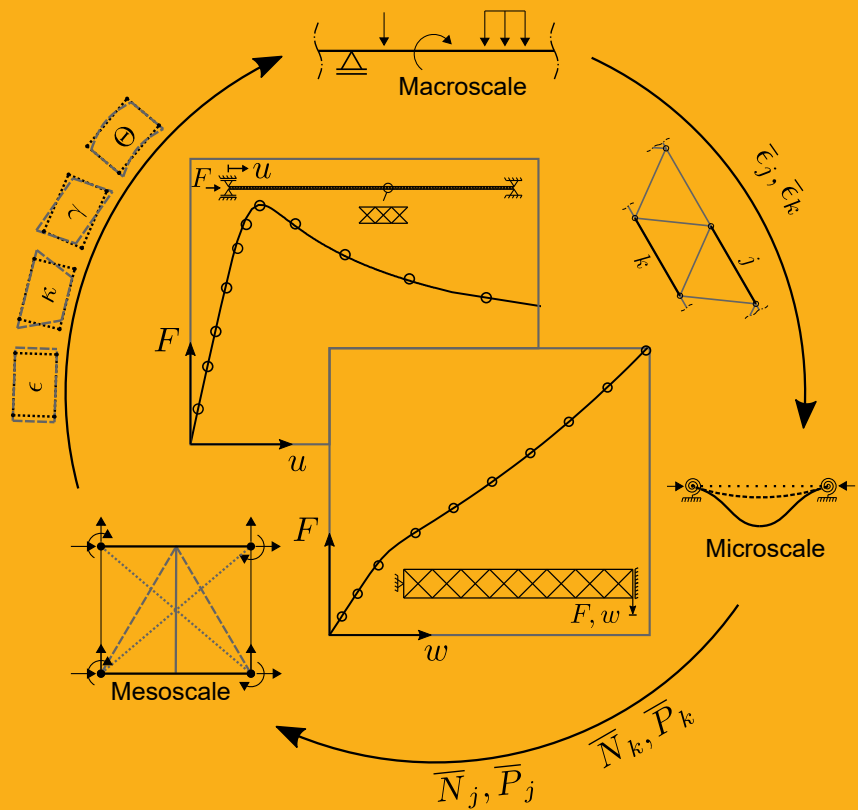


A nonlinear modeling approach for corrugated sandwich beams

Bruno Reinaldo Gonçalves



A nonlinear modeling approach for corrugated sandwich beams

Bruno Reinaldo Gonçalves

A doctoral dissertation completed for the degree of Doctor of Science (Technology) to be defended, with the permission of the Aalto University School of Engineering, at a public examination held at remote connection link <https://aalto.zoom.us/j/64377696949>, on 06 August 2021 at 12.

**Aalto University
School of Engineering
Department of Mechanical Engineering
Marine Technology**

Supervising professor

Professor Jani Romanoff, Aalto University, Finland

Thesis advisor

D.Sc. (Tech.) Anssi Karttunen

Preliminary examiners

Professor Arun R. Srinivasa, Texas A&M University, United States

Professor Jørgen Amdahl, Norwegian University of Science and Technology, Norway

Opponent

Professor Jørgen Amdahl, Norwegian University of Science and Technology, Norway

Aalto University publication series

DOCTORAL DISSERTATIONS 95/2021

© 2021 Bruno Reinaldo Gonçalves

ISBN 978-952-64-0445-5 (printed)

ISBN 978-952-64-0446-2 (pdf)

ISSN 1799-4934 (printed)

ISSN 1799-4942 (pdf)

<http://urn.fi/URN:ISBN:978-952-64-0446-2>

Picaset Oy

Helsinki 2021

Finland



Author

Bruno Reinaldo Gonçalves

Name of the doctoral dissertation

A nonlinear modeling approach for corrugated sandwich beams

Publisher School of Engineering

Unit Department of Mechanical Engineering

Series Aalto University publication series DOCTORAL DISSERTATIONS 95/2021

Field of research Marine Technology

Date of the defence 6 August 2021

Permission for public defence granted (date) 27 April 2021

Language English

☒ **Monograph**

☐ **Article dissertation**

☐ **Essay dissertation**

Abstract

Enhancements in structural efficiency are central in reducing the carbon footprint of the transport industry. With recent manufacturing advances, sandwich panels became viable to reduce the structural weight in large plated structures. Methodologies for their structural modeling and optimization have, however, limitations, as simplified models cannot predict scale interactions that arise in lightweight settings. This dissertation proposes a scale-dependent modeling approach to predict the geometrically nonlinear response of elastic sandwich beams. The approach can predict size effects and the influence of local elastic buckling in the global beam response.

In this work, a computationally efficient multiscale approach is defined. A couple stress-based beam model is employed to describe the global behavior, with constitutive relations that represent unit-cell deformation modes. Scale transitions are embedded in the beam constitutive matrix. Terms associated with the axial behavior of the sandwich face sheets are progressively adapted according to the global strain-state and an associated local model. Stress recovery is pursued consistently with the averaging rules, including recovery of periodic terms. A finite element based on previous works is presented along with adapted nonlinear root-finding schemes to solve the equilibrium equations. Stiffness properties of selected sandwich cells are derived and presented in closed form.

The results reveal that the modeling approach succeeds in predicting the nonlinear response of elastic sandwich panels under quasi-static loads. Accurate stress distributions were obtained for linear and moderately nonlinear responses. Bending and progressive buckling geometric failure paths were successfully traced, including the effect of progressive local face sheet buckling. The approach was tested against different combinations of structural parameters, revealing a wide applicability range.

With the present approach, accurate elastic response predictions result with low modeling and computational costs. Reliable output is obtained, from beams with lightweight local-buckling-prone to denser size-effect-sensitive unit cell setups. The approach offers substantial improvements in relation to other low-complexity models available in the literature. Unlike Cauchy-based models, it is able to describe size-dependent behavior through the couple stress-related parameters. In relation to conventional single-layer models, it incorporates nonlinear local scale information to the average global continuum. In the linear scale-independent case and for an antiplane core, the model reduces to the textbook thick-face sandwich theory.

Keywords Couple stress, sandwich structures, multiscale modeling, size effects, local buckling

ISBN (printed) 978-952-64-0445-5

ISBN (pdf) 978-952-64-0446-2

ISSN (printed) 1799-4934

ISSN (pdf) 1799-4942

Location of publisher Helsinki

Location of printing Helsinki

Year 2021

Pages 163

urn <http://urn.fi/URN:ISBN:978-952-64-0446-2>

Preface

The research in this doctoral dissertation was conducted in the Marine Technology group of Aalto University's Department of Mechanical Engineering. The work received financial support from the Aalto University School of Engineering and research projects: Finland Distinguished Professor (FiDiPro) "Nonlinear Response of Large, Complex and Thin-Walled Structures", funded by the Finnish Funding Agency for Innovation (Tekes), Deltamarin, Napa Ltd, Koneteknologiakeskus Turku, Ruukki and STX Finland, and "Ultra-Lightweight and Fracture Resistant Thin-Walled Structures through Optimization of Strain Paths", funded by the Academy of Finland. Their financial support is gratefully acknowledged. I also gratefully acknowledge the Merenkulun säätiö for the personal study grants provided and the CSC - IT Centre for Science Ltd. for the ABAQUS package license.

I want to express my gratitude to my supervisor, Professor Jani Romanoff, for the mentorship, support and patience throughout the years. The guidance provided by my thesis advisor D.Sc. Anssi Karttunen and former advisor Professor Jasmin Jelovica is also greatly appreciated. I want to thank Professor J.N. Reddy for having me as a visitor and providing valuable advices. I am grateful to Professor Heikki Remes and Professor Emeritus Petri Varsta for the encouragement and outstanding group support. I thank my preliminary examiner Professor Arun Srinivasa, and preliminary examiner and opponent Professor Jørgen Amdahl for the contributions to the work and valuable feedback. I was fortunate to have great colleagues and thank them for being part of this journey. I would like to thank Pauli Lehto, Sami Liinalampi (in memoriam, 11.2.1987-6.6.2018), Mihkel Kõrgesaar, Gonçalo Sorger, Pasquale Gallo, Kennie Berntsson, Federica Mancini, Halid Yıldırım, Ingrid Lillemäe-Avi, Eero Avi, Otto Puolakka, Osiris Valdez Banda and all other lab colleagues for the friendship and support.

Preface

I thank my parents, Benito Reinaldo Pajaro and Sonia Maria Gonçalves Reinaldo, for the upbringing and great relationship over my entire life. I thank them for investing in my education and well-being as a priority. My wife and life partner Aleksandra Smolarczyk is greatly acknowledged for the never-ending support and encouragement.

Espoo, July 18, 2021,

Bruno Reinaldo Gonçalves

Contents

Preface	1
Contents	3
Symbols	7
1. Introduction	11
1.1 Towards lightweight ship structures	11
1.1.1 Transport sector overview	11
1.1.2 Energy efficiency in the maritime industry	12
1.1.3 Lightweight ship design	13
1.2 Lightweight sandwich structures	16
1.2.1 Sandwich panels: an overview	16
1.2.2 ULS analysis of corrugated sandwich panels	19
1.3 Continuum models for corrugated sandwich panels	20
1.3.1 Overview	20
1.3.2 Equivalent single-layer (ESL) models	21
1.3.3 Non-classical continua	22
1.3.4 Multiscale models: failure and other local effects	23
1.4 Scope and novel features of the work	25
1.5 Structure of the dissertation	26
1.6 Author contribution	27
2. Original features	29
3. A multiscale modeling approach	31
3.1 General assumptions	31
3.2 Macroscale and mesoscale	34
3.2.1 Macroscopic kinematics and static equilibrium	35
3.2.2 Macroscopic constitutive relations	37

3.2.3	Mesosopic stiffness derivations	41
3.3	Microscale	45
3.3.1	Kinematics and static equilibrium	46
3.3.2	Local buckling analysis	47
3.4	Nonlinear scale transitions	50
3.4.1	Macro-to-micro scale transition	50
3.4.2	Micro-macro scale transitions	51
3.5	Downscaling: face sheet stress recovery	52
3.6	Finite element scheme	54
3.6.1	Finite element model	54
3.6.2	Nonlinear finite element solution	56
4.	Analysis of selected unit cells	59
4.1	Homogenized stiffness properties	59
4.1.1	Semi-rigid web-core unit cell	61
4.1.2	X-core unit cell	63
4.1.3	Triangular core unit cell	65
4.1.4	Y-core unit cell	67
4.1.5	Hexagonal cell	69
4.1.6	Cells with higher vertical corrugation order	71
4.2	Core rotational stiffnesses	72
5.	Linear model and validations	75
5.1	Two-scale linear model	75
5.1.1	Macroscale and constitutive relations	75
5.1.2	Linear finite element equations	76
5.2	Analogy with the thick-face sandwich theory	77
5.3	Numerical validations	79
5.3.1	Linear bending deflection analyses	80
5.3.2	Linear bending stress analyses	81
5.3.3	Linear buckling analyses	88
6.	Multiscale analyses	91
6.1	General assumptions	91
6.2	Nonlinear bending studies	92
6.2.1	X-core beam with variable core relative flexibility	92
6.2.2	Progressive bending failure and stress analysis	95
6.3	Nonlinear buckling studies	100
6.3.1	Post-buckling analysis of a X-core and size effects	100
6.4	Comparison between classical and present models	108
7.	Size effect sensitivity analyses	115

7.1	Effect of cell geometry and density	115
7.1.1	Governing ratios: a simple cell	116
7.1.2	Effect of core setup and governing ratios	117
7.1.3	Effect of stacking sequence	119
7.2	Effect of face-core connection stiffness	119
7.3	Effect of boundary conditions	121
8.	Discussion	125
8.1	On the assumptions and approach	125
8.2	On the structural response	128
8.3	Practical relevance and implications	130
8.4	Future work	130
9.	Conclusions	131
	References	135
A.	Finite element definitions	147
A.1	Lagrangian linear and Hermitian cubic polynomials	147
A.2	Strain-displacement interpolation matrices for the present model	147
A.3	Transformation matrix for the present model	148
A.4	Linear stiffness matrix	148
A.5	Nonlinear secant stiffness matrix	151
A.6	Nonlinear tangent stiffness matrix	155

Symbols

The main symbols utilized in the text are defined as follows. This list serves as a general guide, yet it is not comprehensive. Other symbols or modifications with sub- or superscripts are defined locally.

A, \bar{A}	Axial stiffness
\bar{B}_1, \bar{B}_2	Local buckling-related coupling stiffnesses
C_1, \bar{C}_1	Stretch to stretch-bending couple stiffness
C_2	Stretch to curvature coupling stiffness
C_3	Stretch-bending to curvature coupling
D, \bar{D}	Stretch-bending stiffness
D_f	Combined bending stiffness of the face sheets
D_Q	Transverse shear stiffness
E, \bar{E}	Elastic modulus
F_h, F_v, F_θ	Unit cell boundary forces
\bar{G}	Transverse shear modulus
K_s	Shear correction factor
L	Length
M	Stretch-bending moment
N	Normal force
N_g	Critical global buckling load
N_w	Critical wrinkling load
\hat{N}_i	Localized normal force over segment i
P	Bending moment
\hat{P}_i	Localized bending moment over segment i
Q	Shear force
Q_{ij}	Constitutive stress-to-strain coefficients

Symbols

S	Cell-bending stiffness
\underline{U}	Strain energy
U_x, U_z	Two-dimensional displacement field
V	Total shear force
\underline{V}	Work done by external forces
\underline{W}	Total work
b	Width
d	Vertical distance between centerline of the face sheets
h	Height
k_c	Core rotational spring coefficient
k_p	Couple-stress distribution factor
k_Q	Shear distribution factor
k_θ	Rotational stiffness of the face sheet-core interface
l	Length
\hat{l}	Arc length
m_{ij}	Deviatoric part of the couple stress tensor
m_{xy}	Couple stress
p	Core strut length
q	Distributed load
r	Iteration
s	Unit cell length
t	Step
t_f	Face sheet thickness
t_c	Core strut thickness
u, w	Mid-height axial and transverse displacements
x, y, z	Cartesian coordinate system
w_0	Initial transverse displacement (imperfection)
B	Linear strain-displacement matrix
B_σ	Geometric strain-displacement matrix
C	Constitutive matrix
F	Nodal force vector
K, K_{ij}	Secant stiffness matrix
K_σ	Geometric stiffness matrix
K₀	Linear stiffness matrix

\mathbf{R}	Residual force vector
$\hat{\mathbf{T}}$	Transformation matrix
\mathbf{T}, T_{ij}	Tangent stiffness matrix
\mathbf{u}	Nodal displacement vector
α_0	Imperfection amplitude
γ, γ_{xz}	Shear angle
Γ	Boundary
δ	Variational operator
Δ_i	Unit cell deformation case
ϵ_{ij}	Components of the strain tensor
ϵ_x	Axial strain
ϵ	Mid-height axial strain
ε	Percent error
θ	Sectional slope
Θ	Curvature
κ	Stretch-curvature
λ	Arc-length load multiplier
ν	Poisson's ratio
ρ	Relative density
ρ	End-fixity factor
σ_{ij}	Components of the Cauchy stress tensor
σ_x	Normal stress
σ_{xz}	Transverse shear stress
$\hat{\sigma}_i$	Localized stress over segment i
ϕ	Sectional rotation angle
ϕ_i	Hermitian cubic interpolation polynomials
χ_{ij}	Components of the curvature tensor
χ_{xy}	Macro-curvature, couple-stress macro-rotation
ψ_i	Lagrange linear interpolation polynomials
Ω	Representative unit cell, element domain
ω	Segment of a unit cell between hard points
ζ	Elastic size-effect sensitivity parameter

1. Introduction

1.1 Towards lightweight ship structures

1.1.1 Transport sector overview

The global energy consumption and greenhouse gas emissions have steadily increased over the past decades (Figure 1.1). While in the developed world the indicators plateaued in the 2000s, fast developing economies maintain the upward trend. IEA projections [3] see a 25% global energy demand increase by 2040, with new emerging markets expected to lead the growth throughout the 2020s [20]. The transport sector is a major player in this framework, amounting to over 20% of the energy demand worldwide [73, 170]. Optimizing the energy performance in the transport of people and goods is therefore a central challenge for our and next generations.

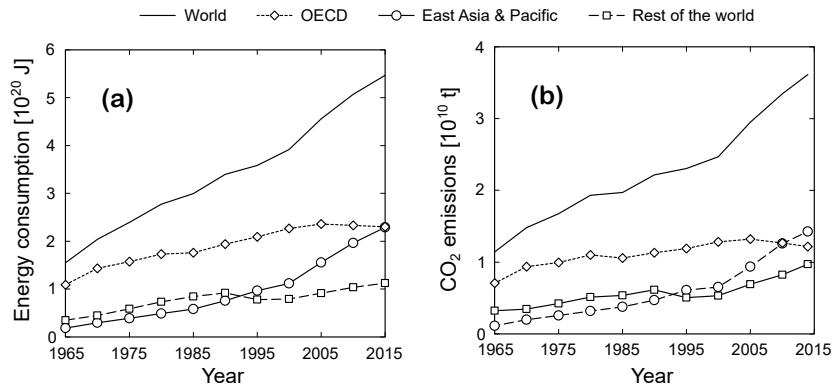


Figure 1.1. (a) Global primary energy consumption (Data from Ref. [138]) and b) global CO₂ emissions (Data from Ref. [165]) with regional shares indicated.

Several complementary changes are needed to impact the energy efficiency of the transport sector. Transport planning is crucial to identify and direct preferred transport modes (Figure 1.2) [157, 168]. Public regulations and taxation are tools that can induce the necessary behavioral changes [27]. Technological advances in equipment, vehicle shape and weight optimization are also central in reducing the energy footprint of the transport modes.

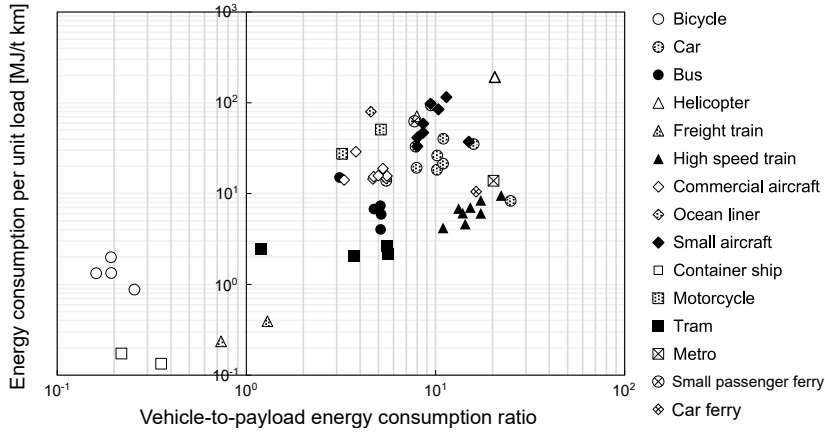


Figure 1.2. Energy consumption per unit load and ratio between vehicle and payload energy for different transport modes. Data extracted from Ref. [168].

1.1.2 Energy efficiency in the maritime industry

Waterborne transport is fundamental for the functioning of our society. It is estimated that circa 90% of the world trade volume is transported through waterways [113]; seaborne freight alone reached 10.7 billion tons in 2017, a more than two-fold increase from 1995 figures [169]. Waterborne transport is also essential for the movement of people and leisure. In recent times, over two billion ferry passengers have been carried every year [19], corresponding to nearly half the yearly volume of the airline industry. The last decades have also seen a surge in the recreational use of vessels. In 2017, 25.8 million cruise passengers were recorded worldwide, almost a 50% increase in a decade [45]. Improving the energy efficiency of water transport modes is crucial in reducing emissions given the freight scales involved and high specific energy consumption of passenger vessels (Figure 1.2).

Numerous recent studies addressed development areas towards energy-efficient ships, in the context of both, cargo and passenger vessels [61, 40, 131]. Significant efficiency improvements can be obtained by simply reduc-

ing the operational speed and designing larger, slenderer hulls [107, 131]. These basic strategies may be complemented by technological advances in different areas as summarized in Table 1.1 [40].

	Design	Operation	Procedures
Hull form optimization	x		
Propulsion efficiency devices	x	x	
New materials	x		
Anti-fouling and coatings		x	x
Waste heat recovery	x		
Auxiliary engine's economizers	x		
Engine/components tuning	x	x	
Electrification and DC grids	x		
Operational optimization		x	x
Speed control of pumps, fans, etc.	x	x	
Trim optimization		x	x
Weather routing		x	x
Speed optimization		x	x
Port/ship logistics			x
Performance/energy monitoring		x	x
Improved power management	x	x	x
Crew awareness			x

Table 1.1. Strategic areas for increasing the energy efficiency of ship structures. Reproduced from Ref. [40].

In Table 1.1, *Design* has two main connotations: I) innovation and optimization of systems and devices, and II) improvements in structural performance through design methodologies, manufacturing techniques and higher-performance materials and shapes. Improved structural performance can be obtained by optimizing the hull form to reduce the overall resistance to movement through water and/or reducing the overall structural weight. Resistance minimization often relies on model testing and computational tools such as the computational fluid dynamics [136, 137]. In turn, the overall structural weight can be reduced through novel materials such as high-strength steels [172], various forms of composites [118, 97] and by simply optimizing the structural topology according to the expected load paths.

1.1.3 Lightweight ship design

Over their lifetime, ship structures are subjected to loads with influence on one or more so-called structural levels (Figure 1.4). Hughes et al. [72] categorize loads in terms of time as

- Static: such as pressures, weights, drydocking loads or thermal loads

- Quasi-static: such as wave-induced pressures or sloshing
- Dynamic: such as slamming or forced vibrations

A structure with capacity R subjected to a load Q must be designed as to have a *sufficiently* low failure probability (Figure 1.3). *Limit state* design defines scenarios and criteria beyond which the structure no longer fulfills its intended purpose [44]. Partial safety factors are utilized to quantify uncertainties [132]. Capacity checks take the form

$$Q_d < R_d, \quad Q_d = \gamma_0 \sum_i Q_{ki}(F_{ki}, \gamma_{fi}), \quad R_d = R_k/(\gamma_m \cdot \gamma_c) \quad (1.1)$$

where Q_d is the design demand (F_{ki} is the characteristic load) and R_d the design capacity. The factor γ_0 accounts for the limit state seriousness, whereas γ_{fi}, γ_m and γ_c relate to uncertainties in load magnitude, material properties and structural capacity, respectively.

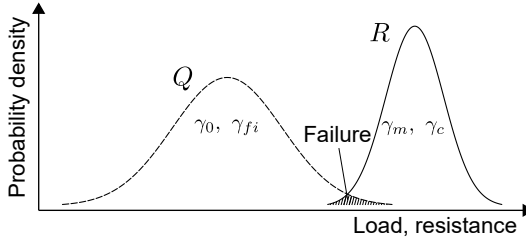


Figure 1.3. Probability density functions for the resistance and loads and their intersection implying structural failure.

Limit states are often classified into *serviceability* (SLS) and *ultimate* (ULS) limit states [44], referring, respectively, to maintained functionality under service loads and structural safety. In marine engineering, accident (ALS) and fatigue (FLS) limit states are also often referred to, given the utilization environment [132]. The limit states can be exemplified as [132]:

- Serviceability (SLS): local damage, excessive noise/vibrations, deformations that affect equipment functioning or aesthetics
- Ultimate strength (ULS): Loss of stability, equilibrium (e.g. capsizing, buckling) or attainment of the maximum strength capacity
- Accident (ALS): excessive structural damage due to collisions, fire, grounding or explosions
- Fatigue (FLS): crack accumulation under repeated load

Limit state design requires clear identification of the load scenarios, a probabilistic measure of uncertainties and methods to capture the structural

response. Given the complexity of the structures involved, the analysis is typically divided into levels, in which different structural scales are treated separately as shown in Figure 1.4.

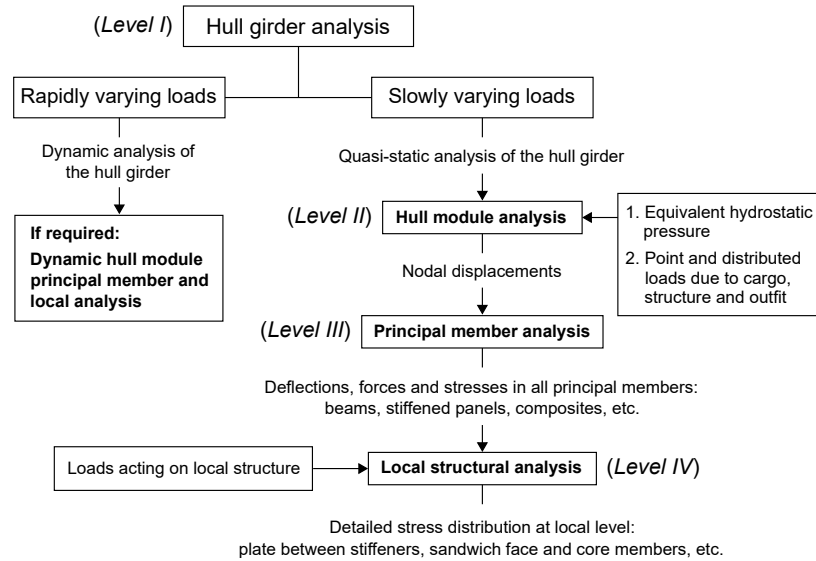


Figure 1.4. Framework for response analysis of ship structures in different structural scales. Adapted from Ref. [72].

Lightweight structures have particularities in their response when compared to standard design solutions, in particular:

- Different vibratory response (SLS): different mass-stiffness ratios, relevance of local vibration modes
- Proneness to instability (ULS): lower buckling capacity at different structural scales, possible geometric instability failure well into the elastic regime
- Influence from geometric imperfections: manufacturing-induced distortions have influence in buckling (ULS) and fatigue (FLS) capacities

In lightweight structures, the local member level often has significant influence on the principal member structural response and vice-versa. As a consequence of scale interactions, analysis methods for lightweight structures require greater sophistication.

In recent years, sandwich panels have been identified as a viable alternative to reduce the structural weight of marine structures. The next sections introduce lightweight sandwich panel design, applications and methods for their structural analysis.

1.2 Lightweight sandwich structures

Lightweight structural design implies employing novel materials and structural configurations to improve the weight-efficiency of a structure in terms of key parameters such as stiffness, strength and ductility. Materials are often compared through the ever-expanding Ashby performance diagrams [11]. Figure 1.5 illustrates the Ashby diagrams for stiffness and strength as function of density, as shown by Fleck et al. [50]. For structures primarily undergoing bending, lattice-type sandwich composites are shown to be a sensible material selection (Figure 1.5).

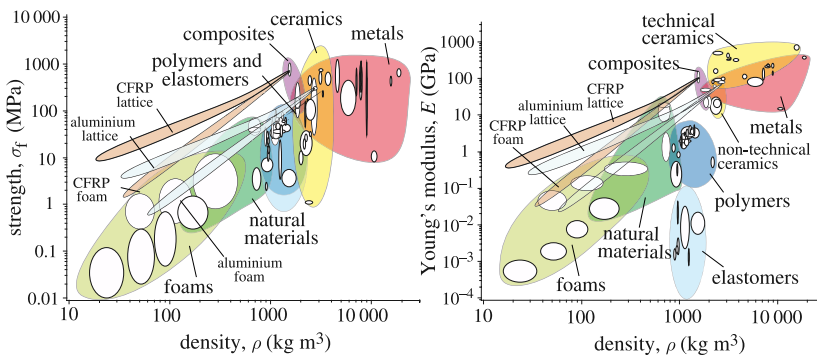


Figure 1.5. Material selection diagrams for elastic modulus and strength as function of density. Adapted from Ref. [50].

1.2.1 Sandwich panels: an overview

Sandwich panels are lightweight composite structures comprising two continuous thin face sheets separated by a comparatively thick low-density core. The assembled structure has high specific bending stiffness provided by the face sheets, which are positioned far from the neutral axis. The core has complementary properties, providing transverse shear stiffness, transverse compressive strength and stabilizing the face sheets. The advantages of sandwich construction have been known for at least two centuries [179], but their use only became widespread in the early-mid 1900s prompted by the aircraft industry's weight efficiency demand [65]. Sandwich panels can be broadly classified based on their general core setup as macro-homogeneous (for example, cellular foam or balsa wood), honeycomb or corrugated [179], with common examples shown in Figure 1.6.

Corrugated sandwich panels are sandwich structures whose core consists of interlaced lattice-type members as exemplified in Figure 1.7. The

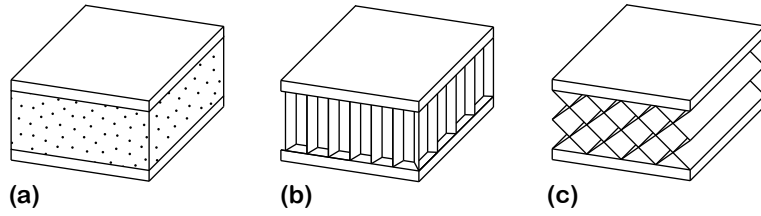


Figure 1.6. Sandwich structure classification according to general core setup (a) macro-homogeneous (b) Honeycomb (c) Corrugated.

face sheets and core can be composed of equal or different materials. The core can be either left void or incorporate macro-homogeneous filling for improved functionality such as increased transverse stiffness and strength [146, 17], or other functions, such as enhancing acoustic or thermal performances, to name a few [180]. Seminal contributions to the analysis and manufacturing of sandwich panels date back to the 1950s, and early works relate to the United States space program [105, 158]. To this date, structural applications are diverse, including marine/naval [97, 119] and aerospace [178] structural components, civil bridge decks [77, 14, 123] and corrugated cardboard for packaging [2, 129].

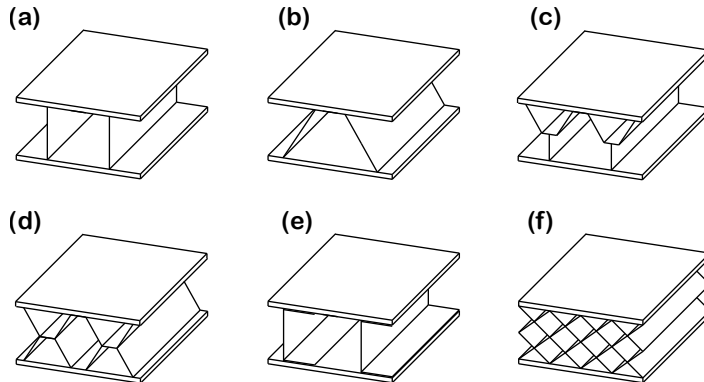


Figure 1.7. Common corrugated sandwich panel arrangements (a) Web-core (b) Hat core (c) Y-core (d) X-Core (e) C-Core (f) Diamond core.

Corrugated sandwich panels can be constructed using different techniques, which are based on either joining the face sheets to a core profile or creating a monolithic entity. The first may be accomplished by adhesive bonding [89], bolting or riveting [53, 54], spot welding [130], brazing [156] or laser-welding [149], whereas the latter is made possible by extrusion [109] and, more recently, various forms of additive manufacturing (3-D

printing) [71, 29]. In non-monolithic cells, the connection stiffness and strength may substantially influence the mechanical performance of the structure. In the realm of laser-welded corrugated panels, the influence of the joints has been object of extensive investigation in terms of transverse shear stiffness and fatigue strength [149, 51, 123, 82].

In the past few years, substantial research has been devoted to optimizing corrugated sandwich structures for pre-determined structural and non-structural functions [161]. Selection of geometric ratios can greatly impact their stiffness and quasi-static strength [18]. Their dynamic response such as in impact and blast attenuation [103, 174] has been a recurring object of study. Sandwich cores can also be optimized for superior thermal [60, 175] and acoustic [153] performances, incorporate fire-resistant materials and others. Improved functions can be obtained by optimizing the core shape [91], density and face sheet thickness, as well as through sensible material selection.

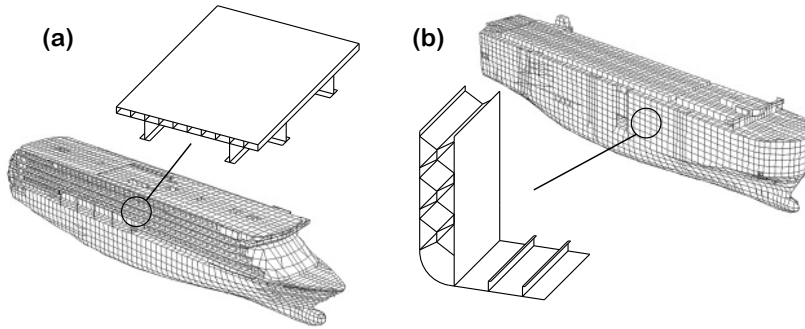


Figure 1.8. Sandwich panels integrated to ship structures (a) web-core cruise ship deck (b) X-core double side structure of a cargo vessel (ship images from Ref. [6]).

Multiple potential sandwich panel applications in marine engineering have been investigated in the past. Several authors described the use of laser-welded [97, 95] and adhesive bonded [89] sandwich panels as decks and bulkheads, substituting the conventional ribbed plate setups (Figure 1.8a). Brazed and laser-welded sandwich panels have been investigated for crashworthy hull designs [119]. In particular, Y-core [156, 152] and X-core [41, 92] sandwich panels (Figure 1.8b) were described to have great energy absorption capacity thanks to their hinged construction. Shape optimization was shown to play a pivotal role in achieving the desired performance [92].

1.2.2 ULS analysis of corrugated sandwich panels

The ultimate limit-state design of corrugated sandwich panels requires understanding of their critical failure modes. Failure under quasi-static loads may have various geometric and/or material modes depending on the core type and governing structural ratios. In lightweight corrugated panels, geometric instability requires careful assessment.

In light of their shear-flexibility, two interacting global failure modes are to be considered (Figure 1.9a): an Euler-type bending mode, and a shear mode related to the flexibility of the core. Local buckling (Figure 1.9b) refers to instability of discrete members (face sheet or core), whereas the global structure remains stable. Widespread local buckling is often referred to as wrinkling; in corrugated panels, the wrinkling wavelength is constrained by the core. Global buckling is observed in slender axially compressed panels. Local buckling may be normative in stocky panels composed of slender struts under axial or transverse compression. Geometric instabilities may occur in conjunction with material nonlinearities (such as plasticity or material rupture).

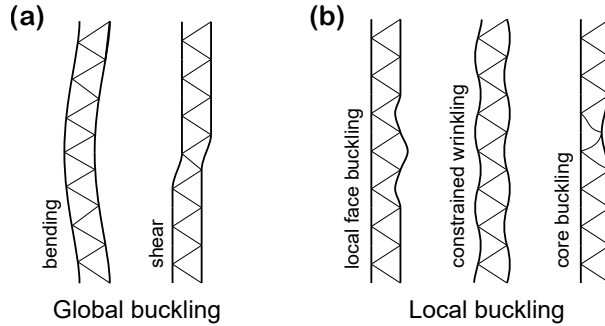


Figure 1.9. Buckling (elastic or plastic) modes of a typical corrugated sandwich beam.

Several studies investigated the progressive nonlinear response of corrugated sandwich beams subjected to quasi-static loads and traced analytical failure maps. Valdevit et al. [171] studied the failure of prismatic sandwich panels with different orders of corrugation under out-of-plane loading. Biagi and Bart-Smith [16] investigated the failure of triangular core sandwich columns under uniaxial compression and provided comparisons between experimental analyses and numerical models. Kooistra et al. [91] proposed a hierarchical corrugated sandwich panel concept and traced failure maps for the competing mechanisms. In Ref. [87], truss-type sandwich members were subjected to transverse compression and horizon-

tal shear and failure maps were traced. Progressive failure studies have been conducted for other analogous sandwich panels with prismatic cores [33, 39].

The failure analysis of corrugated sandwich panels often relies on analytical estimations and three-dimensional finite element analysis. Buckling equations for sandwich beams presented in early sandwich construction books [4, 139] and publications [68, 42] are still in use today. In this spirit, Refs. [110, 171, 34] utilized analytical equations to predict the failure of corrugated core and diamond-type core sandwich panels and compared them with physical tests. Kazemahvazi and Zenkert [88] created a geometrically nonlinear analytical approach for different failure modes of corrugated core sandwich beams, while Ref. [78] developed analytical failure predictions for woven corrugated cores. While analytical estimates have their practical importance, there are limitations in predicting interactive progressive failure modes.

1.3 Continuum models for corrugated sandwich panels

1.3.1 Overview

The structural performance assessment of corrugated sandwich panels requires mathematical models to describe their physical behavior. Discrete finite element models satisfactorily replicate physical tests; solid or beam/shell representations are chosen based on the application. Given the several scales involved, discrete modeling of large structures composed of corrugated panels poses challenges. Homogenized models with effective stiffness properties are thus preferred for preliminary response assessment and optimization. Early works founded the models on the first-order shear deformation theory (FSDT) [105, 104], as the shear deformation was identified to be significant. Conventional first-order theories were then extended to account for the effect of thick faces and horizontal sliding [4, 139, 179]. Since then, numerous theories have emerged with different degrees of complexity and accuracy.

In their generic sense, equivalent continuum models for sandwich structures can be categorized into single-layer or layerwise according to the dependency of layer-level variables [26]. Further, single-layer models may be classical (see [142] for Kirchhoff and FSDT theories for laminated structures) or take various forms of higher-order formulations [114, 81]. Higher-order theories are refinements of the classical theories and in-

clude additional kinematical terms, which can be determined for macro-homogeneous [52] and corrugated sandwich structures [64, 150, 76]. Both, single-layer and layerwise models can be modified to include zig-zag effects to describe complex through-thickness behavior. Comprehensive reviews on the computational modeling of sandwich structures are provided in Refs. [26, 126, 69, 22, 96].

1.3.2 Equivalent single-layer (ESL) models

Low-complexity equivalent single-layer models are suitable for the analysis of large structures composed of corrugated sandwich panels. Figure 1.10 shows a wide corrugated panel idealized into single-layer plate and beam models with effective stiffness properties. The assumptions needed for a meaningful model reduction in the context of a Timoshenko-type (FSDT) model will be discussed in detail in Chapter 3.

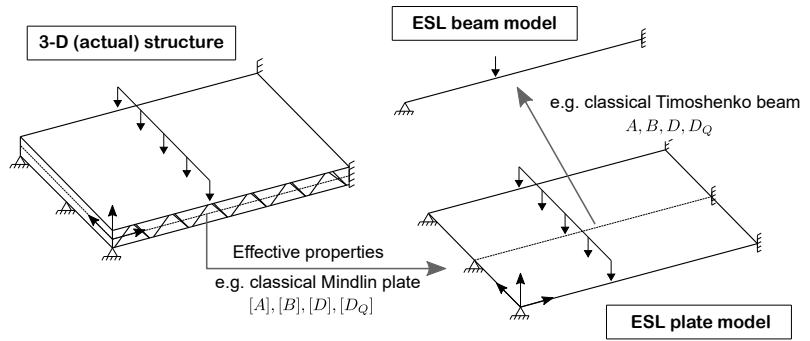


Figure 1.10. Idealization of wide corrugated sandwich panel as a single-layer plate or beam with effective stiffness properties.

Besides defining suitable kinematical assumptions, a central feature in the use of single-layer models is to derive effective properties. Stiffness formulations have been proposed starting from Ref. [105], and models for different sandwich cores are still under development today. In particular, the determination of equivalent transverse shear stiffness for first-order shear deformation theories has drawn substantial interest [53, 54, 109, 57, 124, 129]. Theoretical transverse shear formulations for discrete cores do not require additional correction factors and can include features other than the combined stiffness of the cell members, such as the effect of semi-rigid connections [149, 124] and contact interactions [54]. While most studies focus on analytical transverse shear derivations, some authors provided experimental validations [129]. Classical first-order-founded (FSDT) equivalent single-layer models can accurately describe the behavior

of most sandwich cells. Yet, due to the lack of a cell-related deformation measure, inaccuracies are observed once cell-structure scale interactions are present (as for relatively large, shear-flexible cells). Non-classical continua offer mechanisms to correct this limitation.

1.3.3 Non-classical continua

Non-classical theories increment the Cauchy continuum with additional parameters to model length scale interactions. Figure 1.11 shows a theory classification as proposed by Srinivasa and Reddy [155]. In the context of elastic solids, non-classical continua often converge to the various forms of couple stress [115, 90, 177, 62] and micropolar [43, 159] theories, whose fundamental difference lies in the presence or absence of additional kinematical variables other than the displacement field. Comprehensive reviews of developments in this respect are presented in Refs. [155, 63].

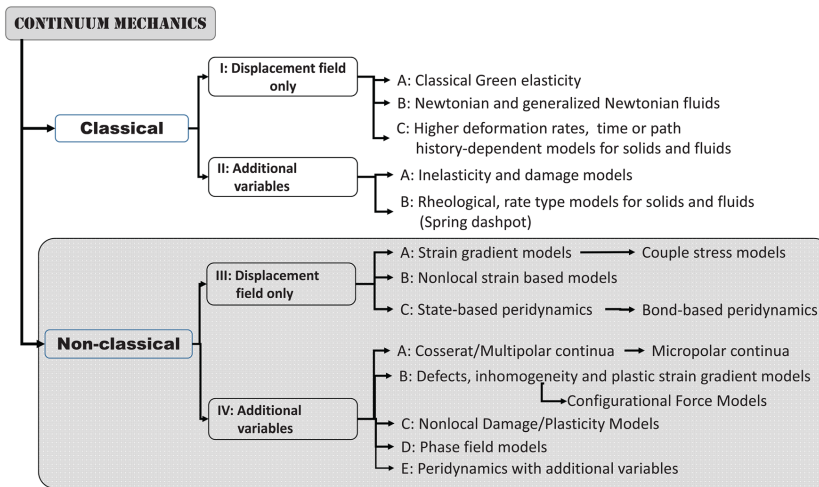


Figure 1.11. General classification of non-classical continuum models. Reproduced from Srinivasa and Reddy [155].

The seminal idea of a non-classical continuum was (presumably) first presented in Cosserat and Cosserat [32], who supplemented the Cauchy continuum with independent rotations. Decades later, the concepts gained interest and were further developed in a theoretical level [115, 167, 116]. In recent years, the non-classical theories reemerged and reached the spotlight prompted by size effect observations in micro- and nanoscale devices [99, 100, 106, 102, 162, 163] and cellular structures of complex topology [98, 108, 134]. Non-classical theories require the determination of length-scale parameters, which are analytically derived or fitted based

on experiments to describe scale interactions (see Ref. [101] for an experimental procedure).

Under the umbrella of non-classical continua, the modified couple stress theory (MCST) [177] has received great acceptance given its relative simplicity. Contrary to the early non-classical theories, the MCST requires a single length-scale parameter with sound physical interpretation. Euler-Bernoulli [133] and Timoshenko [111, 9] beam models for isotropic materials have been proposed within the MCST framework. The models were extended for the analysis of layered beams [143, 7, 10], in line with the standard analysis of laminated structures. Several finite element formulations were proposed for MCST-based beam and plates, some of which are presented in Refs. [7, 58, 57, 38, 85].

In the 1960s, revival of non-classical continua led to analogies with lattice structures [164] that prompted further research. In a seminal contribution, Bazant and Christensen [13] proposed a micropolar continuum parallel to describe large grid frameworks. Noor [127, 128, 125] developed micropolar models for several lattice-type structures of various shapes and provided basis for stiffness derivations through strain energy equivalence. In a recent contribution, Penta [135] used a similar micropolar analogy in the buckling analysis of Vierendeel trusses.

In the past few years, non-classical continua found application in the single-layer modeling of corrugated sandwich structures. Cell-structure stiffness interactions are observed in shear-flexible setups, and accurate continuum description requires the development of size-dependent models. Romanoff et al. [147] first proposed a MCST-based model for web-core sandwich beams and provided experimental validation for the size effects. Several studies then followed the condensed MCST perspective with extension to other sandwich unit cells [59, 58, 57, 148]. Karttunen and colleagues [83, 84, 86] created micropolar beam and plate models for corrugated sandwich panels, which provide more accurate transverse shear description than in the MCST models. A finite element for the micropolar beam model has been presented in [120]. A review on the utilization of non-classical continua to model corrugated sandwich panels (with marine applications) is provided in Ref. [145].

1.3.4 Multiscale models: failure and other local effects

Multiscale modeling incorporates interacting length scales into an average effective macroscopic continuum model. Multiscale methods require three basic components: a physical model for the microscale, a downscal-

ing rule as boundary condition for the microscale, and an upscaling rule to determine macroscopic stresses [47, 79]. The microscopic averaging rules and scale transitions must guarantee that the Hill-Mandel macro-homogeneity condition [66, 67, 112] is met. That is, energy conservation must be ensured.

Among the numerous multiscale methods available (see Refs. [80, 122] for comprehensive reviews), the so-called computational homogenization has received substantial attention [55]. A computational homogenization scheme transfers kinematical information from the macroscale as boundary conditions for the boundary value problem of a representative unit. Displacements and boundary tractions are obtained at the microscopic level, which are then averaged into a macroscopic stress tensor [55]. A FE2 method results if both scales are solved simultaneously using the finite element method [49, 48]. In recent years, schemes that include higher-order gradients of displacements have been defined. By Taylor expanding the macroscopic deformation measure and truncating after the second-order term, one obtains a *second-order homogenization* scheme [93, 94]. In similar manner, higher-order schemes may be obtained.

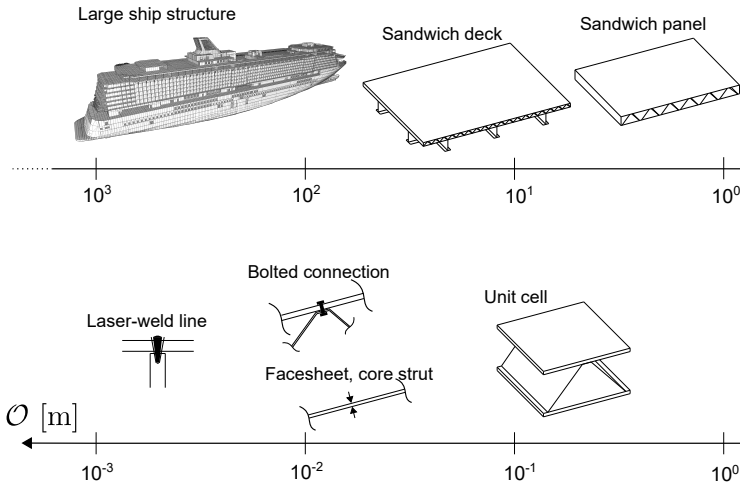


Figure 1.12. Scales involved in the design of a large ship structure constructed with sandwich panels and their orders of magnitude.

Figure 1.12 demonstrates the multiple scales present in large structures composed of corrugated sandwich panels. Microstructure-independent models fail to capture localized mechanisms at homogenized sub-scales [75, 120]. Multiscale concepts can be employed to condense nonlinearities in sub-panel scales into an effective equivalent single-layer model. To this

date, few authors attempted to derive corrugated sandwich panel models with multiple nonlinear scales. Rabczuk et al. [140] created a three-layer quasi-continuum that can handle nonlinear transverse behavior. In their model, an unit cell is modeled as two conventional beams representing the face sheets connected to a homogenized shell element that represents the core. The core element has effective nonlinear properties to incorporate member-level buckling in an average sense. Goncalves et al. [56] proposed an ESL model with nonlinear stiffness properties to predict local buckling, following the ideas of Byklum and colleagues for ribbed panels [24, 23, 25]. These models are, however, dissimilar from the conventional FE2 as the microscopic behavior is pre-determined by subjecting a representative cell of the structure to idealized displacement boundary conditions.

1.4 Scope and novel features of the work

Previous studies demonstrated the power of equivalent-single-layer models in predicting the stiffness response of corrugated sandwich structures under quasi-static loads. Classical first-order (FSDT) models are accurate in the absence of significant scale interactions. Cauchy-based models are, however, unable to describe the response of short, transversely shear-flexible structures due to the lack of size-dependent parameters. Moreover, models with linear microscale cannot predict local geometric instabilities that can substantially affect the global structural response.

In this context, this doctoral dissertation provides an homogenized modeling approach for corrugated sandwich beams that contains information from interdependent nonlinear scales. The main objectives are

- (I) To define a nonlinear size-dependent homogenized model for corrugated sandwich beams;
- (II) To create a constitutive approach that includes unit cell geometric parameters and nonlinear information from a sub-cell scale into the homogenized beam equilibrium;
- (III) To provide a finite element model, stiffness matrices and iterative scheme for the scale transitions;

The *macroscopic* equivalent single-layer model is founded on a couple stress-based (MCST) Timoshenko beam theory, providing theoretical basis for a size-dependent formulation. The macroscopic constitutive equations have analogy with boundary tractions on a structural cell (*mesoscale*) subjected to idealized displacements. Scale transitions are enforced within the

macroscopic stiffnesses, whose formulations are derived from a geometrically nonlinear *microscopic* face sheet model. Predictor-corrector iterations seek equilibrium between macroscopic and microscopic states.

The approach is validated in different configurations against equivalent three-dimensional finite element models and analytical equations. A linear version of the model is derived, compared with finite-element results and other state-of-art homogenized beam models. Progressive nonlinear bending and post-buckling analyses demonstrate the relevance of the nonlinear scale interactions and showcase the capability of the homogenized model in predicting them. Sensitivity analyses are conducted to identify the parameters governing the size-dependent response.

1.5 Structure of the dissertation

The doctoral dissertation is organized in chapters that are summarized as follows

- Chapter 2 summarizes the main novel contributions of the work.
- Chapter 3 introduces a nonlinear modeling approach for corrugated sandwich beams. The scales and their interrelationships are defined. A macroscopic couple stress model is derived with constitutive relations from unit cell analysis. The scale transitions are described and an analytical microscopic model developed. A homogeneous-to-discrete stress localization scheme is determined. A finite element is provided, along with an implicit scheme to solve the set of algebraic finite-element equations.
- Chapter 4 presents stiffness derivations for selected unit cells through conventional plane frame analysis. In the general case, the stiffnesses are function of the microscopic state. Core-related input parameters for the microscopic model are derived.
- Chapter 5 presents a two-scale linear model simplification. Comparison with the conventional thick-face sandwich beam theory is presented. Validations are conducted through bending (deflection and stress) and linear buckling analyses.
- Chapter 6 utilizes the multiscale modeling approach to predict the nonlinear response of corrugated sandwich beams. Nonlinear bending and buckling analyses are conducted to trace progressive failure

paths. Comparisons with conventional models and closed-form equations are provided.

- Chapter 7 provides size-effect sensitivity studies based on the couple stress model. The structural parameters that lead to size-dependency are identified. The suitability of the model in capturing size effects is assessed.
- Chapter 8 provides discussions on the assumptions, relevance, suitability and limitations of the present modeling approach, along with directions for future studies.
- Chapter 9 presents the main conclusions from the study.

1.6 Author contribution

The Author has carried out the research presented in this doctoral dissertation independently. The dissertation supervisor and advisor have contributed by providing constructive feedback and helped define the scope and extent of research. The doctoral dissertation has been partially based on journal publications by the Author. Minor direct reproductions from these documents are presented in the dissertation, with the source explicitly disclosed. The concepts in the entire dissertation are extended from Ref. [58], Ref. [59] and Ref. [57]. The treatment of geometric nonlinearities is based on the conclusions of Ref. [56].

2. Original features

As manufacturing evolves, lightweight corrugated sandwich panels become a viable design solution. Their stiffness behavior is, however, not accurately described with the conventional plane-stress theories. A modified couple stress model with nonlinear scale interactions is employed to predict their progressive bending and buckling response. In this context, the main contributions of this work are:

1. A scale-dependent nonlinear model for bending and buckling analysis of corrugated beams. The homogenized description represents superimposed two-dimensional cell deformation modes. The model has a fully coupled constitutive matrix to describe normal stresses. Stiffnesses are determined based on cell micromechanics. A finite element based on previous works and related stiffness matrices are provided.
2. A multiscale approach to incorporate micro-nonlinearities to the homogenized equilibrium equations. Nonlinear scale interactions are obtained via macroscopic stiffness updates. The nonlinear stiffnesses are function of the macroscopic strain state and of an embedded analytical microscopic model. Conventional implicit finite-element solvers are modified to incorporate nonlinear stiffness behavior.
3. An analytical nonlinear microscopic model to extract the average geometrically nonlinear stretch response of the sandwich face sheets. Equivalent homogenized stiffness terms are derived as function of the strain-state.
4. A stress localization scheme for the face sheets of corrugated sandwich cells. In addition to the averaging of macroscopic quantities, recovery of zero-average periodic terms and linear superposition of local stresses.

3. A multiscale modeling approach

In this chapter, a novel multiscale modeling approach for corrugated sandwich beams with arbitrary core is derived. The model supplements Ref. [57] by the Author with nonlinear sub-structural information via a scale transition scheme. First, the general assumptions needed for an equivalent model are discussed and the scale interrelationships are defined. The macroscale is derived along with constitutive relations, which result from mesoscale and microscale analyses. Localized stiffness effects are embedded via coordinate-dependent nonlinear coefficients, which are extracted from the microscale as function of the strain state. A homogeneous-to-discrete localization scheme is then determined and discussed. A finite element is provided in conjunction with iterative implicit schemes to attain energetic scale equilibrium.

3.1 General assumptions

A sandwich beam is an idealization of a three-dimensional sandwich panel, in which the response described by the Theory of Elasticity can be reduced as independent of the width coordinate (Figure 3.1). The plane-strain idealization applies to beam-like structures such as wide plates undergoing cylindrical bending. Corrugated sandwich beams are geometrically periodic, composed of two-dimensional repeating blocks named *unit cells*.

Figure 3.1 depicts a generic unit cell with horizontal and vertical dimensions s and h , respectively. Two continuous horizontal thin-walled members, namely the face sheets or simply the *faces*, are positioned at the vertical ends; in the present work, equal thickness $t_t = t_b = t_f$ is assumed for a condensed presentation. The beam width b , that is, the y -axis dimension, is unity ($b = 1.0$); forces are then implied to refer to as per unit width. The depth, namely the dimension between the centerline of the faces, is defined as $d = h - t_f$.

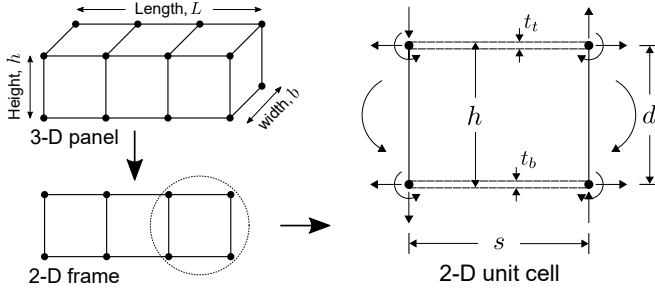


Figure 3.1. Corrugated sandwich beam as an idealization of the three-dimensional structure, and unit cell with general dimensions and boundary forces indicated.

Corrugated cores have thin-walled members interlaced in a single direction, see Figure 1.7 for examples. The discrete connection points between face sheets and core struts are denoted *hard points*. The local transverse deformation at the hard points is negligible. Rectangular corrugated cells are connected at least at their four outer corners, which transmit forces between consecutive cells (Figure 3.1). In the derivations presented, the core interface between neighboring cells is assumed to be void.

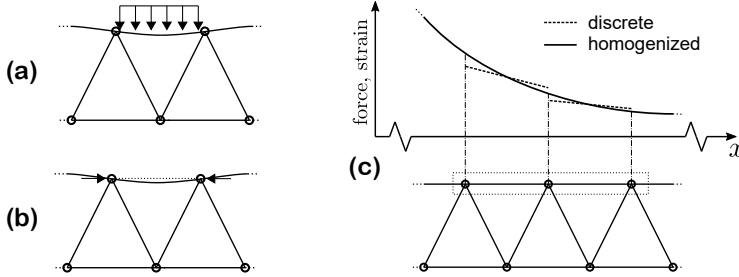


Figure 3.2. Localized effects due to (a) local loads (b) local buckling, and (c) face sheet discrete and homogenized bending descriptions.

Homogenization of two-dimensional cells into an one-dimensional continuum requires kinematic compatibility and the definition of scale averaging rules. The response is said purely *global* in the absence of localized loads (such as patch loads, Figure 3.2a) and local nonlinearities (such as local buckling, Figure 3.2b). As illustrated in Figure 3.2c, the global bending-induced response of corrugated sandwich face sheets is discontinuous piecewise linear and can be averaged into a two-scale size-dependent model through linear combination of unit cell representative modes. Localized effects introduce stress concentrations leading to higher-order piecewise response, and influence the global stiffness behavior. Their continuum modeling requires the incorporation of nonlinear sub-cell scale information into the homogenized description. For moderate localized effects, linear

superposition may be employed to recover the local response provided that the stiffness model is consistent.

The present approach describes the stiffness response of corrugated sandwich beams through three interacting scales:

- *Macroscale*: a 1-D representation of a 2-D sandwich beam;
- *Mesoscale*: a 2-D repeating unit cell of the structure;
- *Microscale*: a sub-cell member; here, a 1-D face sheet segment;

Four cell deformation modes are utilized to determine macroscopic stiffness and localize the averaged solution (Figure 3.3). Scale transitions are enforced by modifying the macroscopic constitutive law with nonlinear (coordinate- and state-dependent) stiffness terms. Small strains and moderate rotations are incorporated at macroscopic and microscopic scales through the von Kármán kinematics. Microscale-independency leads to a two-scale (macro-meso) *global* model with constant stiffnesses.

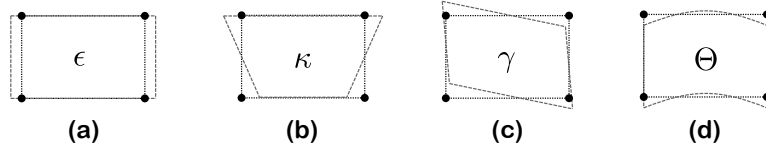


Figure 3.3. Cell deformation modes upon which constitutive relations are built (a) uniform stretch (b) stretch-bending (c) periodic shear deformation (d) curvature.

In this work, nonlinear geometric information is extracted from the a microscopic face sheet model to incorporate the effect of local buckling in the homogenized solution. Stretch-related face sheet stiffness terms are thus state-dependent. Nonlinearities are assumed to be sufficiently small as not to strongly influence the internal force distribution due to transverse loads. The effect of local loads is not object of this work; transverse loads are assumed to produce a transversely incompressible state and consequent periodic shear distribution. The validation models are built accordingly.

The approach is summarized in Figure 3.4. The macroscopic predictor displacement field is averaged over equal stiffness intervals. The average microscopic $\bar{\epsilon}_i$ strain is utilized to compute internal forces N_i and M_i from an analytical nonlinear microscopic model. The microscopic forces, along with Ω unit cell-dependent geometric and core material information, are used to obtain a macroscopic corrector constitutive matrix \mathbf{C} . For every load increment, iterations continue until the scales are in energetic equilibrium. The macroscale is post-processed to predict discrete stresses over the two-dimensional structure.

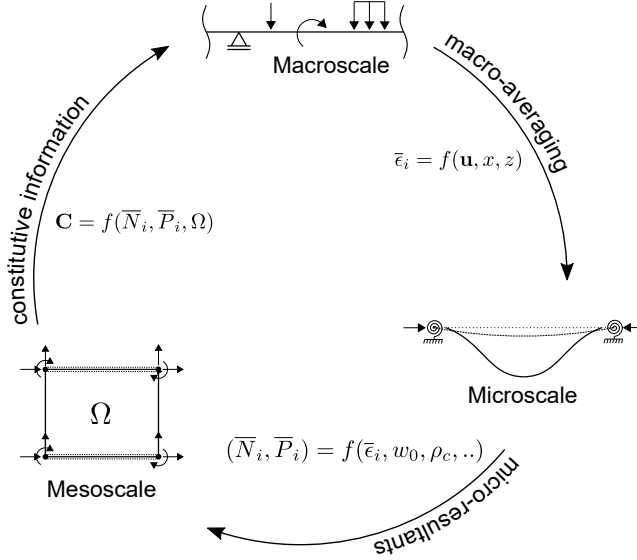


Figure 3.4. A novel multiscale approach with scale transitions and interrelationships indicated; iterations in a typical load increment.

3.2 Macroscale and mesoscale

The macroscale is based on the modified couple stress-based Timoshenko beam theory [143, 111]. Modifications are made in line with the model derived by the Author in Ref. [57], such that the constitutive relations and stress resultants have a direct correspondence with the boundary forces on an idealized corrugated two-dimensional sandwich unit cell. The macroscale describes the nonlinear response in terms of the undeformed configuration and does not consider changes in geometry in computing equilibrium. Macroscopic geometric nonlinearities are described based on the von Kármán assumption, implying validity limited to small strains and moderate rotations.

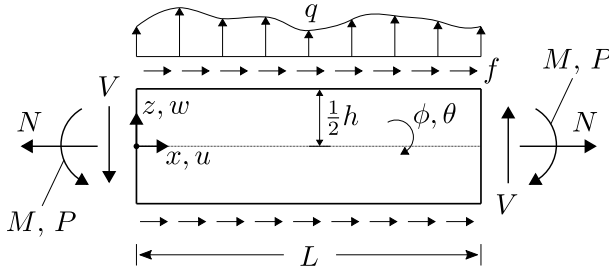


Figure 3.5. Conventions upon which the macroscopic couple stress beam model is constructed. Adapted from Gonçalves et al. [57].

3.2.1 Macroscopic kinematics and static equilibrium

Figure 3.5 shows the general conventions of a couple stress beam of length L and height h . The two-dimensional displacement field can be written as

$$U_x(x, z) = u(x) + z\phi(x) \quad (3.1a)$$

$$U_z(x, z) = w(x) \quad (3.1b)$$

where u , w and ϕ are the axial centerline and transverse displacements, and the cross-sectional rotation about the y -axis, respectively. The kinematics of deformation of the Timoshenko model is summarized in Figure 3.6.

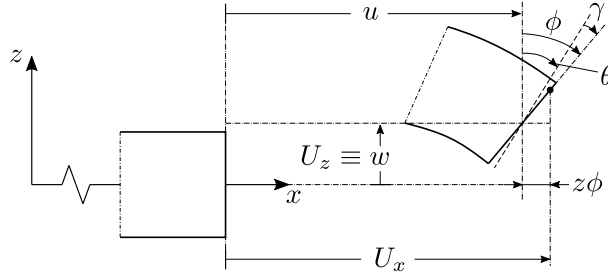


Figure 3.6. Kinematics of the Timoshenko-based beam model with 1-D and 2-D displacement components indicated (displacements are exaggerated).

The nonzero strains, which include the von Kármán nonlinear term in addition to the linear strains, as well as the curvature related to the macro-rotation of the couple stress model, are [143]

$$\epsilon_x = \frac{\partial u}{\partial x} + \frac{1}{2} \left(\frac{\partial w}{\partial x} \right)^2 + z \frac{\partial \phi}{\partial x} = \epsilon + z\kappa \quad (3.2a)$$

$$\gamma_{xz} \equiv \gamma = \phi - \theta \quad (3.2b)$$

$$\chi_{xy} = \frac{1}{4} \left(\frac{\partial \phi}{\partial x} - \frac{\partial^2 w}{\partial x^2} \right) = \frac{1}{4} (\kappa + \Theta) \quad (3.2c)$$

where

$$\theta = -\frac{\partial w}{\partial x}, \quad \kappa = \frac{\partial \phi}{\partial x}, \quad \Theta = \frac{\partial \theta}{\partial x} = -\frac{\partial^2 w}{\partial x^2} \quad (3.3)$$

The principle of virtual displacements for the static case yields

$$\delta \underline{W} = \delta \underline{U} + \delta \underline{V} = 0 \quad (3.4)$$

where $\delta \underline{W}$ is the total virtual work, $\delta \underline{U}$ is the virtual strain energy and $\delta \underline{V}$

the virtual work done by applied forces.

The virtual strain energy of the modified couple stress theory [177] can be written as the volume integral

$$\delta \underline{U} = \int_v (\sigma_{ij} \delta \epsilon_{ij} + m_{ij} \delta \chi_{ij}) dv \quad (3.5)$$

where m_{ij} is the deviatoric part of the couple stress tensor and χ_{ij} the components of the curvature tensor. Considering only the non-zero stress and strain components, the virtual strain energy becomes [143]

$$\begin{aligned} \delta \underline{U} &= \int_0^L \int_A (\sigma_x \delta \epsilon_x + \sigma_{xz} \delta \gamma_{xz} + 2m_{xy} \delta \chi_{xy}) dA dx \\ &= \int_0^L \left[N \left(\frac{\partial \delta u}{\partial x} + \frac{\partial w}{\partial x} \frac{\partial \delta w}{\partial x} \right) + M \frac{\partial \delta \phi}{\partial x} + Q \left(\delta \phi + \frac{\partial \delta w}{\partial x} \right) - P \frac{\partial^2 \delta w}{\partial x^2} \right] dx \end{aligned} \quad (3.6)$$

The virtual work done by external forces in absence of body couples is given by [143]

$$\begin{aligned} \delta \underline{V} &= - \int_0^L (f \delta u + q \delta w) dx + [N(0) \delta u(0) + V(0) \delta w(0) + M(0) \delta \phi(0) \\ &\quad + P(0) \delta \theta(0) - N(L) \delta u(L) - V(L) \delta w(L) - M(L) \delta \phi(L) - P(L) \delta \theta(L)] \end{aligned} \quad (3.7)$$

where

$$V = Q + \frac{\partial P}{\partial x} + N \frac{\partial w}{\partial x} \quad (3.8)$$

The axial N , shear Q and two independent bending stress resultants (stretch-bending) M and (local bending) P utilized in Eq. 3.6 and Eq. 3.7 are the internal forces of the beam per unit width, defined as (Figure 3.5) [57]

$$N = \int_z \sigma_x dz \quad (3.9a)$$

$$Q = K_s \int_z \sigma_{xz} dz \quad (3.9b)$$

$$M = \int_z \left(\sigma_x z + \frac{1}{2} m_{xy} \right) dz \quad (3.9c)$$

$$P = \frac{1}{2} \int_z m_{xy} dz \quad (3.9d)$$

where K_s is the shear correction factor of the Timoshenko beam theory.

The static equilibrium equations are obtained as

$$\frac{\partial N}{\partial x} = -f \quad (3.10a)$$

$$\frac{\partial V}{\partial x} = -q \quad (3.10b)$$

$$Q - \frac{\partial M}{\partial x} = 0 \quad (3.10c)$$

The boundary conditions are one of each following duality pairs

$$N \text{ or } u, \quad V \text{ or } w, \quad M \text{ or } \phi, \quad P \text{ or } \theta \quad (3.11)$$

and must be specified at the beam end coordinates $x = 0$ and $x = L$.

3.2.2 Macroscopic constitutive relations

A nonlinear constitutive model is defined as proposed by the Author [57]. Stresses and strains are coupled by coefficients Q_{ij} , which are, in the general case, nonlinear

$$\sigma_x = Q_{11}\epsilon_x + Q_{13}\chi_{xy} \quad (3.12a)$$

$$2m_{xy} = Q_{31}\epsilon_x + Q_{33}\chi_{xy} \quad (3.12b)$$

$$\sigma_{xz} = Q_{22}\gamma_{xz} \quad (3.12c)$$

The stresses have an analogy with the tractions at a representative section of the structure. Homogenized constitutive relations are demonstrated for a simplified antiplane core and extended for a generic structure.

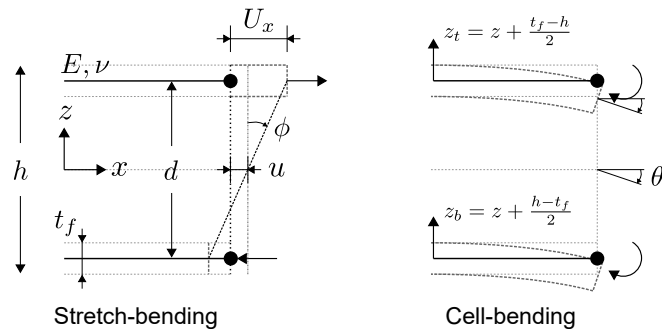


Figure 3.7. Compatibility between displacement of the faces and homogenized cross-sectional properties.

Antiplane core

An antiplane sandwich cell has a negligible effective core elastic modulus ($\bar{E}_c \approx 0$). As consequence, the transverse shear stresses are independent of the height coordinate [4]. Consider the antiplane cell section with $E_t = E_b = E$ and $t_t = t_b = t_f$ depicted in Figure 3.7. The homogenized normal and couple-stress distributions are derived from independent conventional Euler-Bernoulli beams.

The stretch (κ) and local (Θ) bending components of the couple stress model are decoupled by enforcing

$$4Q_{13}z + Q_{33} = 0 \quad (3.13)$$

The coefficients Q_{11} and Q_{33} describe independent stretch- and cell bending-related stress components based on the model in Fig. 3.7

$$Q_{11}z^2 - \frac{Q_{33}}{16} = E(z^2 - zz_i) \quad (3.14a)$$

$$Q_{33} = 16Ez_iz \quad (3.14b)$$

where

$$z_t = z - \frac{h}{2} + \frac{t_f}{2}, \quad z_b = z + \frac{h}{2} - \frac{t_f}{2} \quad (3.15)$$

The constitutive coefficients reduce to

$$Q_{11} = E \quad (3.16a)$$

$$Q_{13} = -4Ez_i(z) \quad (3.16b)$$

$$Q_{33} = 16Ez_i(z) \quad (3.16c)$$

And the corresponding 2-D normal stress distribution becomes

$$\sigma_x = E[\epsilon + (z - z_i)\kappa - z_i\Theta] \quad (3.17a)$$

$$m_{xy} = 2Ez_i[z\Theta - \epsilon] \quad (3.17b)$$

where m_{xy} is the cell-bending component. The stretch-related bending component in Eq. 3.9 becomes

$$\sigma_x z + \frac{1}{2}m_{xy} = E(z - z_i)(\epsilon + z\kappa) \quad (3.18)$$

The transverse shear stress is represented by an independent linear equa-

tion

$$\sigma_{xz} = \bar{G}\gamma, \rightarrow Q_{22} = \bar{G} \quad (3.19)$$

where \bar{G} is a core-dependent property that represents the effective combined behavior of the composite phases.

Substituting Eq. 3.17 and Eq. 3.19 into Eq. 3.9, and solving the through-thickness integrals, the constitutive matrix for a beam composed of antiplane cells with equal face sheets is obtained

$$\begin{Bmatrix} N \\ M \\ Q \\ P \end{Bmatrix} = \begin{bmatrix} A & 0 & 0 & 0 \\ 0 & D & 0 & 0 \\ 0 & 0 & D_Q & 0 \\ 0 & 0 & 0 & S \end{bmatrix} \begin{Bmatrix} \epsilon \\ \kappa \\ \gamma \\ \Theta \end{Bmatrix} \quad (3.20)$$

The antiplane stiffnesses are defined as

$$A = \int_{-\frac{h}{2}}^{\frac{h}{2}} E dz = 2Et_f \quad (3.21a)$$

$$D = D_G - S = \int_{-\frac{h}{2}}^{\frac{h}{2}} Ez^2 dz - \int_{-\frac{h}{2}}^{\frac{h}{2}} Ezz_i(z) dz = \frac{1}{2}Et_f d^2 \quad (3.21b)$$

$$S = \int_{-\frac{h}{2}}^{\frac{h}{2}} Ezz_i(z) dz = \frac{1}{6}Et_f^3 \quad (3.21c)$$

$$D_Q = \int_{-\frac{h}{2}}^{\frac{h}{2}} \bar{G} dz \quad (3.21d)$$

where A is the axial, D the stretch-bending, S the unit cell bending, and D_Q the transverse shear stiffness. Integration of the bending stresses result in zero axial couplings, as expected for a symmetric setup where neutral axis and mid-plane coincide.

The constitutive matrix for a sandwich beam with antiplane core and equal face sheets is diagonal. The linearized antiplane-core non-classical model results equal to the thick-face sandwich theory [4, 139] as demonstrated in Section 5.2.

Arbitrary corrugated core, linear microscale

For a generic corrugated cell where the core in-plane stress is non-zero, $\bar{E}_c \neq 0$, macroscopic normal and couple stresses are fully coupled to the axial strain and macro-rotation-related curvature (Eq. 3.12). In relation to

Eq. 3.20, three coupling constitutive coefficients (C_i) emerge in the general case. The macroscopic constitutive relations becomes

$$\begin{pmatrix} N \\ M \\ Q \\ P \end{pmatrix} = \begin{bmatrix} A & C_1 & 0 & C_2 \\ C_1 & D & 0 & C_3 \\ 0 & 0 & D_Q & 0 \\ C_2 & C_3 & 0 & S \end{bmatrix} \begin{pmatrix} \epsilon \\ \kappa \\ \gamma \\ \Theta \end{pmatrix} \quad (3.22)$$

The constitutive matrix is symmetric. Linear unit cells with a horizontal symmetry line have $C_1 = 0$. Direct height integration analogous to Eq. 3.21 is cumbersome for complex corrugated sandwich beams. A mesoscopic unit cell analysis is generally preferred for stiffness computations, as demonstrated in Section 3.2.3. The same stiffnesses could be defined by energy considerations as described in Ref. [125].

Arbitrary corrugated core, nonlinear microscale

Local buckling is embedded into the macroscopic equilibrium by modification of the constitutive coefficients. The constitutive matrix becomes

$$\begin{pmatrix} N \\ M \\ Q \\ P \end{pmatrix} = \begin{bmatrix} \bar{A} & \bar{C}_1 & 0 & C_2 \\ \bar{C}_1 & \bar{D} & 0 & C_3 \\ 0 & 0 & D_Q & 0 \\ C_2 + \bar{B}_1 & C_3 + \bar{B}_2 & 0 & S \end{bmatrix} \begin{pmatrix} \epsilon \\ \kappa \\ \gamma \\ \Theta \end{pmatrix} \quad (3.23)$$

where \bar{A} , \bar{C}_1 and \bar{D} are effective coefficients, which incorporate the axial stiffness degradation of the face sheets based on a microscopic model.

The constitutive matrix has symmetric hyperelastic components and two pseudo coefficients that yield asymmetry. The coefficients \bar{B}_1 and \bar{B}_2 transfer the strain energy related to the secondary local bending to the macroscopic equilibrium equations. In relation to Eq. 3.9d, the local bending resultant P is supplemented by an artificial stress component

$$P = \frac{1}{2} \int_z m_{xy} dz + \int_z \sigma_{x;2} dz \quad (3.24)$$

where $\sigma_{x;2}$ denotes a secondary bending-related normal stress. Analogously, an artificial force-displacement pair emerges in the macroscopic strain energy (Eq. 3.6).

Equilibrium in terms of displacements

The equilibrium equations, written as function of generalized displacements and homogenized stiffnesses are, in the general case, given by

$$(i): \quad \frac{\partial}{\partial x} \left\{ \bar{A} \left[\frac{\partial u}{\partial x} + \frac{1}{2} \left(\frac{\partial w}{\partial x} \right)^2 \right] + \bar{C}_1 \frac{\partial \phi}{\partial x} - C_2 \frac{\partial^2 w}{\partial x^2} \right\} = -f \quad (3.25a)$$

$$(ii): \quad \frac{\partial}{\partial x} \left\{ \bar{A} \left[\frac{\partial u}{\partial x} + \frac{1}{2} \left(\frac{\partial w}{\partial x} \right)^2 \right] \frac{\partial w}{\partial x} + \bar{C}_1 \frac{\partial \phi}{\partial x} \frac{\partial w}{\partial x} + D_Q \left(\phi + \frac{\partial w}{\partial x} \right) - S \frac{\partial^3 w}{\partial x^3} + (C_2 + \bar{B}_1) \frac{\partial^2 u}{\partial x^2} + \bar{B}_1 \frac{\partial w}{\partial x} \frac{\partial^2 w}{\partial x^2} + (C_3 + \bar{B}_2) \frac{\partial^2 \phi}{\partial x^2} \right\} = -q \quad (3.25b)$$

$$(iii): \quad D_Q \left(\phi + \frac{\partial w}{\partial x} \right) - \frac{\partial}{\partial x} \left\{ \bar{C}_1 \left[\frac{\partial u}{\partial x} + \frac{1}{2} \left(\frac{\partial w}{\partial x} \right)^2 \right] + \bar{D} \frac{\partial \phi}{\partial x} + C_3 \frac{\partial^2 w}{\partial x^2} \right\} = 0 \quad (3.25c)$$

For negligible microscopic stiffness, $S, C_2, C_3, \bar{B}_1, \bar{B}_2 \rightarrow 0$, Eq. 3.25a-c reduce to the equilibrium equations of the classical Timoshenko beam theory with von Kármán nonlinearity.

3.2.3 Mesoscopic stiffness derivations

The micromechanics of an arbitrarily placed unit cell $\Omega = [x_a, x_b]$ is analyzed to compute homogenized macroscopic stiffnesses. Figure 3.8 shows the conventions adopted, consistent with the two-dimensional displacement field of the macroscopic model. The four outer corners represent the cell connectivity at the centerline of the face sheets. The outward normal vector to the boundary $\partial\Omega$ is n . Displacements are assumed to be small relative to the cell general dimensions. Constitutive relations are determined from linear Euler-Bernoulli frame models, as demonstrated in Section 4.1 for selected corrugated cells. Macroscopic geometric nonlinearity (von Kármán) is neglected to estimate stiffnesses.

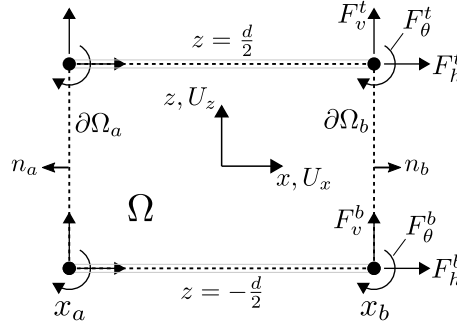


Figure 3.8. Conventions adopted to determine equivalent macroscopic stiffnesses from a 2-D unit cell.

Antiperiodic boundary displacements U^Γ are enforced (Figure 3.9) inducing modes Δ_i that fulfill the Hill-Mandel macrohomogeneity condition [66, 67, 112]. Unit cell average strains $\bar{\varepsilon}_\Omega$ are computed from boundary displacements U_i ($U_x, U_z, \partial U_z / \partial x$) and related to the macroscopic strains

$$\bar{\varepsilon}_\Omega = \frac{1}{2sd} \int_{x_a}^{x_b} \int_{z_a}^{z_b} [U_i(x_b, z)n_b + U_i(x_a, z)n_a] dz dx \rightarrow \bar{\varepsilon}, \bar{\kappa}, \bar{\gamma}, \bar{\chi} \quad (3.26)$$

Boundary forces that are equal in magnitude and opposite in direction emerge

$$F_{[v,h,\theta]}(x_b, d/2) = -F_{[v,h,\theta]}(x_a, d/2) = F_{[v,h,\theta]}^t \quad (3.27a)$$

$$F_{[v,h,\theta]}(x_b, -d/2) = -F_{[v,h,\theta]}(x_a, -d/2) = F_{[v,h,\theta]}^b \quad (3.27b)$$

which translate into macroscopic stress resultants through

$$N = F_h^t + F_h^b \quad (3.28a)$$

$$M = (F_h^t - F_h^b) \frac{d}{2} - \frac{(F_v^t + F_v^b)s}{2} \quad (3.28b)$$

$$Q = F_v^t + F_v^b \quad (3.28c)$$

$$P = F_\theta^t + F_\theta^b \quad (3.28d)$$

The unit cell boundary conditions related to modes Δ_i , equivalent macroscopic strains and resulting homogenized stiffnesses are presented in the following sub-sections for each idealized mode.

Axial, bending and coupling stiffnesses, modes Δ_1 and Δ_2

Figure 3.9a and Figure 3.9b depict antiperiodic axial translations that produce zero local curvature. The displacement conditions that define modes Δ_1 and Δ_2 are

$$\Delta_1: \quad U^\Gamma = U_x(x_b, z) = -U_x(x_a, z) \quad (3.29a)$$

$$\Delta_2: \quad U^\Gamma = U_x\left(x_b, \frac{d}{2}\right) = -U_x\left(x_b, -\frac{d}{2}\right) \quad (3.29b)$$

in either case subjected to

$$\frac{\partial U_z}{\partial x}(x_b, z) = \frac{\partial U_z}{\partial x}(x_a, z) = 0 \quad (3.30)$$

that is, the local curvature is zero. Vertical boundary displacement is free to maintain the plane stress condition $\therefore F_v^t = F_v^b = 0$.

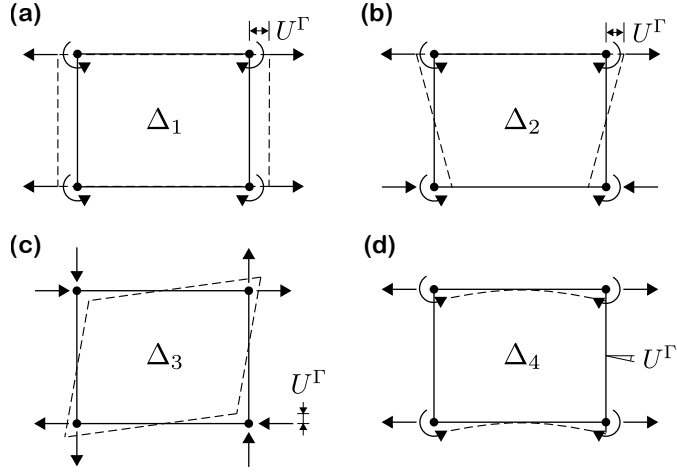


Figure 3.9. Mesoscopic displacement boundary conditions employed for macroscopic stiffness computations (a) uniform stretch (b) stretch-bending (c) shear (d) unit cell bending modes.

The strains, which represent relative changes in length ($\Delta l/l_0$) uniformly over the boundary $\partial\Omega$ (ϵ) or linearly varying over the depth d at $\partial\Omega$ (κ), can be written as

$$\Delta_1: \quad \epsilon = \frac{2U^\Gamma}{s} \quad (3.31a)$$

$$\Delta_2: \quad \kappa = \frac{4U^\Gamma}{sd} \quad (3.31b)$$

Combinations define equivalent axial, bending and coupling macroscopic stiffnesses, in the general case, as

$$\Delta_1: \quad \bar{A} = \frac{N}{\epsilon} = \frac{(F_h^t + F_h^b)s}{2U^\Gamma}, \quad \bar{C}_1 = \frac{M}{\epsilon} = \frac{(F_h^t - F_h^b)sd}{4U^\Gamma} \quad (3.32a)$$

$$C_2 = \frac{P}{\epsilon} = \frac{(F_\theta^t + F_\theta^b)s}{2U^\Gamma} \quad (3.32b)$$

$$\Delta_2: \quad \bar{C}_1 = \frac{N}{\kappa} = \frac{(F_h^t + F_h^b)sd}{4U^\Gamma}, \quad \bar{D} = \frac{M}{\kappa} = \frac{(F_h^t - F_h^b)sd^2}{8U^\Gamma} \quad (3.32c)$$

$$C_3 = \frac{P}{\kappa} = \frac{(F_\theta^t + F_\theta^b)sd}{4U^\Gamma} \quad (3.32d)$$

Face sheet nonlinearities are embedded into the stretch-related stiffnesses by progressively adapting the forces F_h and F_θ according to the microscopic model. For linear microscale, the stiffnesses are denoted without overline and the relations are solved in closed-form.

Transverse shear stiffness, mode Δ_3

Figure 3.9c shows a cell undergoing periodic transverse shear deformation due to acting internal vertical forces. Vertical boundary displacements U^Γ are enforced

$$U^\Gamma = U_z(x_b, z) = -U_z(x_a, z) \quad (3.33)$$

The unit cell is subjected to zero-average forces that restore moment equilibrium, which induce a periodic horizontal displacement without stretch

$$U_x(x_b, z) = U_x(x_a, z), \quad F_h^t = -F_h^b = \frac{(F_v^t + F_v^b)s}{2d} \quad (3.34)$$

Zero local curvature is implied from the conditions proposed. The equivalent transverse shear strain has vertical and horizontal components, which are defined as

$$\gamma = \frac{2U^\Gamma}{s} + \frac{1}{d} \left[U_x\left(x, \frac{d}{2}\right) - U_x\left(x, -\frac{d}{2}\right) \right] \quad (3.35)$$

The macroscopic transverse shear stiffness results into

$$D_Q = \frac{Q}{\gamma} = \frac{(F_v^t + F_v^b)sd}{2U^\Gamma d + \left[U_x\left(x, \frac{d}{2}\right) - U_x\left(x, -\frac{d}{2}\right) \right] s} \quad (3.36)$$

Local cell bending and coupling stiffnesses, mode Δ_4

Figure 3.9d shows an unit cell bending locally in absence of horizontal stretch. The enforced displacements Γ are

$$U^\Gamma = \frac{\partial U_z}{\partial x}(x_b, z) = -\frac{\partial U_z}{\partial x}(x_a, z) \quad (3.37)$$

subjected to the zero-stretch condition

$$U_x(x_b, z) = U_x(x_a, z) = 0 \quad (3.38)$$

The average unit cell curvature is given by

$$\Theta = \frac{2U^\Gamma}{s} \quad (3.39)$$

Vertical boundary displacement is free to maintain the plane stress condition $\therefore F_v^t = F_v^b = 0$. The cell bending stiffness S and related couplings are defined

$$\begin{aligned}
 S &= \frac{P}{\Theta} = \frac{(F_{\theta}^t + F_{\theta}^b)s}{2U^{\Gamma}}, & C_2 &= \frac{N}{\Theta} = \frac{(F_h^t + F_h^b)s}{2U^{\Gamma}} \\
 C_3 &= \frac{M}{\Theta} = \frac{(F_h^t - F_h^b)sd}{4U^{\Gamma}}
 \end{aligned} \tag{3.40}$$

The cell bending stiffness is also related to the local shear force $\partial P/\partial x$.

3.3 Microscale

Figure 3.10 shows a microscopic beam model representing the i th face between arbitrary consecutive hard points of the two-dimensional structure. The face sheet is assumed to be vertically supported on the core, $w_i(x_a) = w_i(x_b) = 0$. Reaction forces N_i and P_i develop due to the imposed macroscopic average stretch (Figure 3.10b).

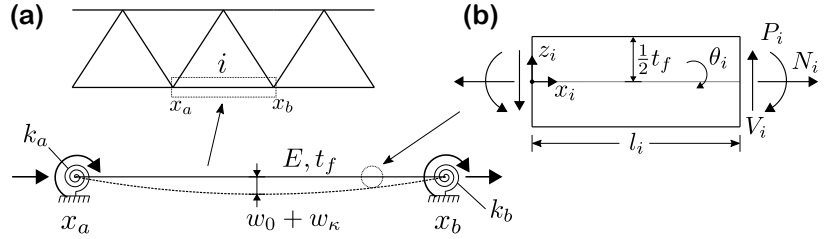


Figure 3.10. Idealization of an imperfect face segment as a simply supported 1-D beam with end rotational springs.

Rotational springs represent attached core struts. Their effective behavior is described via semi-rigidity factors [117]

$$\varrho = \left(1 + \frac{3EI_f}{k_c l_i}\right)^{-1} \tag{3.41}$$

where $I_f = t_f^3/12$ and k_c is the effective core rotational restraint, which depends on the core setup and expected load paths. The basic concept is demonstrated in Figure 3.11. Estimates of k_c for selected corrugated cores are presented in Section 4.2.

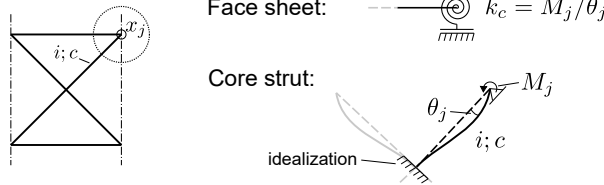


Figure 3.11. Concept of effective core bending stiffness in the derivation of nonlinear microscopic relations.

3.3.1 Kinematics and static equilibrium

Following the von Kármán nonlinear Euler-Bernoulli theory, the microscopic two-dimensional displacement field is given by

$$U_{x;i} = u_i(x_i) + z_i \theta_i(x_i) \quad (3.42a)$$

$$U_{z;i} = w_i(x_i) \quad (3.42b)$$

where u_i, w_i are the axial and transverse micro-displacements, $\theta_i = -\frac{dw_i}{dx}$ the slope and z_i the vertical coordinate. The axial strain, the only non-zero component, is given by

$$\epsilon_{x;i} = \frac{\partial u_i}{\partial x_i} + \frac{1}{2} \left(\frac{\partial w_i}{\partial x_i} \right)^2 + z_i \frac{\partial \theta_i}{\partial x_i} \quad (3.43)$$

The microscopic internal forces are defined as

$$N_i = Et_f \left[\frac{\partial u_i}{\partial x_i} + \frac{1}{2} \left(\frac{\partial w_i}{\partial x_i} \right)^2 \right] \quad (3.44a)$$

$$P_i = -\frac{Et_f^3}{12} \left(\frac{\partial^2 w_i}{\partial x_i^2} \right) \quad (3.44b)$$

$$V_i = \frac{\partial M_i}{\partial x_i} + N_i \frac{\partial w_i}{\partial x_i} \quad (3.44c)$$

Employing the principle of virtual displacements (see e.g. Ref. [144] for details) and assuming quasi-static conditions, the equilibrium equations become, in absence of axial or transverse distributed loads

$$\frac{\partial N_i}{\partial x_i} = 0 \quad (3.45a)$$

$$\frac{\partial P_i^2}{\partial x_i^2} + \frac{\partial}{\partial x_i} \left[N_i \left(\frac{\partial w_i}{\partial x_i} + \frac{\partial w_0}{\partial x_i} \right) \right] = 0 \quad (3.45b)$$

where w_0 is the initial micro-deflection, whose imposition is needed for nonlinear buckling analysis. The boundary conditions are defined at the beam end coordinates x_a and x_b

$$N_i \text{ or } u_i, \quad V_i \text{ or } w_i, \quad P_i \text{ or } \theta_i \quad (3.46)$$

Equation 3.45 is solved using the slope-deflection method and second-order coefficients to determine moment reactions [8, 166, 12]. Equation 3.45b is evaluated separately, as it can be solved independently of u_i . Derivations for $P_i(x_b) = -P_i(x_a)$ are then conducted.

Integrating Eq. 3.45b twice and enforcing the support conditions, the equilibrium expression obtained is

$$N_i(w_i + w_0) + P_i(x_a) = \frac{Et_f^3}{12} \left(\frac{\partial^2 w_i}{\partial x_i^2} \right) \quad (3.47)$$

3.3.2 Local buckling analysis

The macroscopic stiffness implications of local face sheet buckling are estimated by subjecting the microscopic model to unit stretch and recovering the resulting internal forces. The internal forces are embedded into the mesoscopic unit cell models as later described.

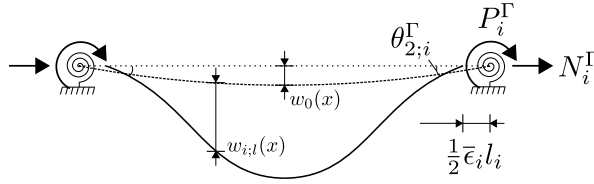


Figure 3.12. End-shortening microscopic boundary value problem, with nodal force conventions and displacement boundary conditions indicated.

The average macroscopic stretch over the face sheet domain $\bar{\epsilon}_i$ is enforced at the beam boundaries as demonstrated in Figure 3.12. The macroscopic curvature $\bar{\Theta}_i$ has minor impact in the progressive instability and is thus neglected.

The displacement boundary conditions for a typical periodic segment i become

$$u_i(x_b) = -u_i(x_a) = \frac{\bar{\epsilon}_i l_i}{2} \quad (3.48a)$$

$$w_i(x_b) = w_i(x_a) = 0 \quad (3.48b)$$

$$\theta_i(x_b) = \theta_{2,i}(x_b) + \frac{\bar{\Theta}_i l_i}{2} \approx \theta_{2,i}(x_b) = \theta_{2,i}^\Gamma \quad (3.48c)$$

$$\theta_i(x_a) = \theta_{2,i}(x_a) - \frac{\bar{\Theta}_i l_i}{2} \approx \theta_{2,i}(x_a) = -\theta_{2,i}^\Gamma \quad (3.48d)$$

where $\theta_{2,i}$ is the secondary-bending (local buckling-related) slope. Equal core rotational stiffness at x_a and x_b is implied.

The related boundary forces can be written as

$$N_i(x_b) = -N_i(x_a) = N_i^\Gamma \quad (3.49a)$$

$$P_i(x_b) = -P_i(x_a) = P_i^\Gamma \quad (3.49b)$$

The assumed conditions are met in nearly all practical sandwich cells.

The face sheet is assumed to have an initial shallow half-sine imperfect shape. The imperfection of amplitude α_0 is described by

$$w_0(x) = \alpha_0 \sin\left(\frac{\pi x_i}{l_i}\right) \quad (3.50)$$

Auxiliary terms are defined as

$$\eta = \sqrt{\frac{12|N_i^\Gamma|l_i^2}{Et_f^3}}, \quad \zeta = \frac{P_i^\Gamma}{N_i^\Gamma} \quad (3.51)$$

In axial compression, $N_i^\Gamma < 0$ and $\int \epsilon_i dx < 0$, the solution to Eq. 3.45b is

$$w_i(x_i) = A_1 \sin\left(\frac{\eta x_i}{l_i}\right) + A_2 \cos\left(\frac{\eta x_i}{l_i}\right) + \frac{\eta^2 w_0}{\pi^2 - \eta^2} \sin\left(\frac{\pi x_i}{l_i}\right) + P_i^\Gamma \quad (3.52)$$

Applying the boundary conditions $w_i(0) = w_i(s) = 0$ the deflection becomes, in the general case

$$w_i(x_i) = \zeta \left\{ \frac{[1 - \cos(\eta)]}{\sin(\eta)} \sin\left(\frac{\eta x_i}{l_i}\right) + \cos\left(\frac{\eta x_i}{l_i}\right) - 1 \right\} + \frac{\eta^2 w_0}{\pi^2 - \eta^2} \sin\left(\frac{\pi x_i}{l_i}\right) \quad (3.53)$$

and the slope $\theta_i = -dw_i/dx_i$

$$\theta_i(x_i) = \zeta \left\{ \frac{\eta[1 - \cos(\eta)]}{l_i \sin(\eta)} \cos\left(\frac{\eta x_i}{l_i}\right) - \frac{\eta}{l_i} \sin\left(\frac{\eta x_i}{l_i}\right) \right\} + \frac{\eta^2 w_0 \pi}{(\pi^2 - \eta^2) l_i} \cos\left(\frac{\pi x_i}{l_i}\right) \quad (3.54)$$

The bending moment distribution results in

$$P_i(x_i) = \frac{\zeta Et_f^3}{12} \left\{ \frac{\eta^2}{l_i^2} \cos\left(\frac{\eta x_i}{s}\right) + \frac{\eta^2 [1 - \cos(\eta)]}{l_i^2 \sin(\eta)} \sin\left(\frac{\eta x_i}{l_i}\right) + \frac{\eta^2 w_0 \pi^2}{(\pi^2 - \eta^2) \zeta l_i} \sin\left(\frac{\pi x_i}{l_i^2}\right) \right\} \quad (3.55)$$

where the boundary reaction is

$$P_i^\Gamma = -\frac{Et_f^3 \rho \pi \eta^3 w_0 [1 + \cos(\eta)]}{4l_i^2 (\pi^2 - \eta^2) [\eta(\rho - 1) \cos(\eta) - 3 \sin(\eta) \rho + (\rho - 1) \eta]} \quad (3.56)$$

The strain due to micro-stretch is computed

$$\bar{\epsilon}_i = \frac{N_\Gamma}{Et_f} - \frac{1}{2l_i} \int_0^{l_i} \left(\frac{dw_i}{dx} \right)^2 dx = -\frac{\eta [a_1 \cos(\eta) - a_2 \zeta^2 \sin(\eta) + a_3 \eta]}{2a_2 l_i^2 (1 + \cos(\eta))} \quad (3.57)$$

where

$$\begin{aligned} a_1 &= \frac{1}{2}\pi\eta^3 w_0(\pi w_0 + 8\zeta), \quad a_2 = (\pi - \eta)^2(\pi + \eta)^2 \\ a_3 &= \pi^4 \zeta^2 + \eta^4 \zeta^2 + \eta^2 \left[4\zeta\pi w_0 + \pi^2 \left(\frac{w_0^2}{2} - 2\zeta^2 \right) \right] \end{aligned} \quad (3.58)$$

The equivalent macroscopic normal force is given by

$$\bar{N}_i = N_i^\Gamma = \frac{1}{l_i} \int_0^{l_i} N_i dx \quad (3.59)$$

The secondary-bending effect is transferred to the macroscale by defining an energetically equivalent constant bending setup as (Figure 3.13)

$$\bar{P}_i = \sqrt{\frac{1}{l_i} \int_0^{l_i} P_i^2 dx} \quad (3.60)$$

The relation between Eq. 3.57, and Eq. 3.59, Eq. 3.60 describes the force-strain progressive local buckling response of a corrugated sandwich face sheet segment. The microscopic support conditions $w(x_a) = w(x_b) = 0$ imply non-zero vertical reactions arising along the secondary bending, but these are not transferred to the macroscale given the plane stress condition, which requires $\sigma_z = 0$. As the domain-average bending moment is transferred, energy conservation is not substantially violated.

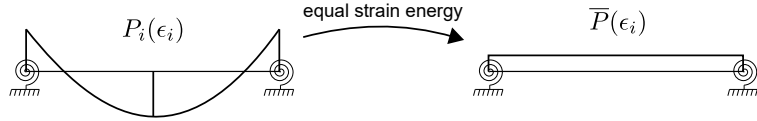


Figure 3.13. Determination of effective local face bending macroscopic stiffness term based on the microscopic state.

The relations presented are valid for a typical periodic segment i . The effect of local slope boundary conditions in the face sheet axial stiffness may be incorporated by setting $\theta_i(x_a) = 0$, resulting in $\theta_{2,i}(x_b) \neq \theta_{2,i}(x_a)$ in Eq. 3.48. The derivations that have been presented may be pursued analogously.

In tension, the microscopic equations output an approximately constant, state-independent response, with a generally minor imperfection straightening effect. Stiffnesses derived from a tensioned microscale under the boundary conditions of Eq. 3.48 usually result approximately equal to the theoretically computed counterparts. Thus, a practical approach may only consider geometric nonlinearities in compression.

3.4 Nonlinear scale transitions

A scale interaction scheme incorporates nonlinear face sheet stiffness effects due into the macroscopic equilibrium equations:

1. *Macro-to-micro transition*: average face sheet strains are computed from the macroscopic solution and enforced as microscopic boundary displacement conditions;
2. *Micro-to-macro transition*: effective face sheet resultants are derived from the microscopic model and the related macroscopic stiffness terms are updated;

A predictor-corrector scheme (see Figure 3.4) iterates the scales for energetic equilibrium at every load increment.

3.4.1 Macro-to-micro scale transition

Figure 3.14a defines the internal segment ω of an arbitrary two-dimensional corrugated beam, where face sheets j and k are located. A cross-sectional cut shows the related internal forces (Figure 3.14b) in typical top and bottom face sheet segments j and k .

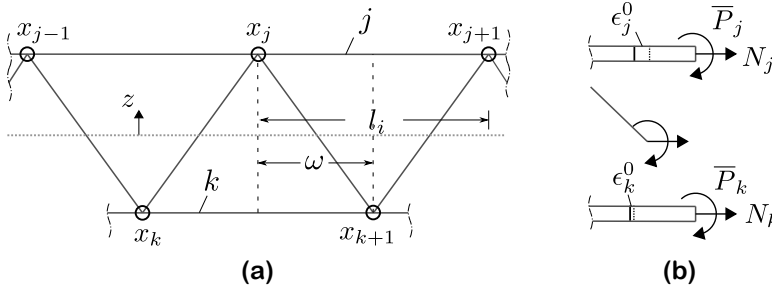


Figure 3.14. (a) Segment ω of a two-dimensional corrugated sandwich beam and (b) a sectional cut in Ω with related internal forces indicated.

Recovering the average axial face sheet strains due to the cell stretch modes in ω from the homogenized macroscopic solution

$$\bar{\epsilon}_j = \frac{1}{l_i} \int_{x_j}^{x_{j+1}} \left(\epsilon + \frac{d}{2} \kappa \right) dx \quad (3.61a)$$

$$\bar{\epsilon}_k = \frac{1}{l_i} \int_{x_k}^{x_{k+1}} \left(\epsilon - \frac{d}{2} \kappa \right) dx \quad (3.61b)$$

The strains are imposed to the microscopic model through displacement boundary conditions (Eq. 3.48).

3.4.2 Micro-macro scale transitions

The micro-macro transition consists in determining macroscopic stiffnesses based on microscopic force-strain relations. The boundary force N_i^Γ and moment distribution $P_i(x_i)$ are obtained when solving Eq. 3.57 for the boundary conditions of Eq. 3.48, and the segment averages are computed using Eq. 3.59 and Eq. 3.60.

In compression, the effective axial modulus and pseudo-stiffness for the secondary-bending energy are given by ($i = j, k$)

$$\bar{E}_i = \frac{1}{t_f} \frac{\bar{N}_i}{\bar{\epsilon}_i} \quad (3.62a)$$

$$\bar{B}_i = \left| \frac{\bar{P}_i}{\bar{\epsilon}_i} \right| \quad (3.62b)$$

In a pre-buckling compressive state, the microscopic equations yield $\bar{E}_i \approx E$ and $\bar{B}_i \approx 0$. In tension $\bar{E}_i = E$ and $\bar{B}_i = 0$ may be taken.

The effective face sheet-related macroscopic stiffnesses associated with the stretch-related mesoscopic modes Δ_1 and Δ_2 are computed for an internal segment ω

$$\bar{A}(\epsilon, \omega) = (\bar{E}_j + \bar{E}_k) t_f \quad (3.63a)$$

$$\bar{D}(\epsilon, \omega) = (\bar{E}_j + \bar{E}_k) \frac{t_f d^2}{4} \quad (3.63b)$$

$$\bar{C}_1(\epsilon, \omega) = (\bar{E}_j - \bar{E}_k) \frac{t_f d}{2} \quad (3.63c)$$

$$\bar{B}_1(\epsilon, \omega) = \pm(\bar{B}_j + \bar{B}_k) \quad (3.63d)$$

$$\bar{B}_2(\epsilon, \omega) = \pm(\bar{B}_j + \bar{B}_k) \frac{d}{2} \quad (3.63e)$$

to which the linear core contribution terms are added. Secondary bending related to local buckling effectively *stiffens* the macroscopic beam, as it offsets the energy balance by the portion spent in bending the related face sheet. The pseudo-stiffness coefficients \bar{B}_1 (Eq. 3.63d) and \bar{B}_2 (Eq. 3.63e) must have their signs chosen as to produce the desired effect. A practical approach is to select $\bar{B}_1 = 0$ and \bar{B}_2 as positive, as $\kappa \approx \Theta$ in local buckling-prone structures.

The relations presented imply that the macroscopic beam is composed of piecewise constant stiffness intervals that depend on the two-dimensional geometry and strain state.

3.5 Downscaling: face sheet stress recovery

In this section, a scheme to recover the discrete two-dimensional response from the average homogenized solution based on the homogenization rules and microscopic strain state is defined. In this section, face sheet stresses are studied. Core strut stress distributions may be reasoned from equilibrium as exemplified in Section 5.3.2 for a web-core beam.

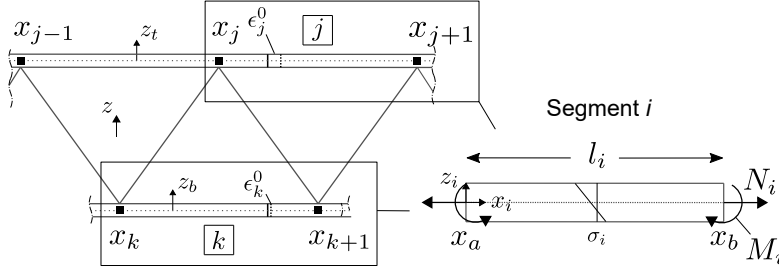


Figure 3.15. Conventions adopted in the stress analysis of a sandwich face segment based on the 1-D homogenized model.

Figure 3.15 shows the i th face sheet interval between hard points of the two-dimensional structure. Segment conventions follow the microscopic model of Section 3.3. Localized stresses denoted l are obtained by linear mode superposition

- Stresses due to (i) stretch, (ii) *stretch-bending* and (iii) *unit cell bending* are extracted from the homogenized 1-D solution and averaged over discrete face sheet intervals
- Macroscopic (iv) *shear-induced* stresses averaged in the macroscopic level through the stiffnesses D_Q and $\partial P/\partial x$ are recovered based on the unit cell shear distribution
- Nonlinear (v) *second-order* face sheet stresses have their strain energy averaged into effective macroscopic stiffnesses; recovery is based on the macroscopic state and microscopic relations

The discrete normal face sheet resultant is obtained by macroscopic averaging as

$$\hat{N}_i = \frac{Et_f}{l_i} \int_{x_a}^{x_b} \left(\epsilon_0 + \frac{d^2}{4d_i} \kappa_0 \right) dx \quad (3.64)$$

where d_i is defined as $d_j = d/2$ (top segment) and $d_k = -d/2$ (bottom segment).

The bending resultant has average cell-bending, local buckling and periodic shear components

$$\hat{P}_i(x_i) = \frac{Et_f^3}{12l_i} \int_{x_a}^{x_b} \Theta dx + P_i(x_i) + P_{Q;i}(x_i) \quad (3.65)$$

where P_i is extracted from the face sheet model of segment i as function of the macroscopic strain (Eq. 3.61 and Eq. 3.55) and

$$P_{Q;i}(x_i) = \frac{x_i}{l_i} \int_{x_a}^{x_b} \left(k_Q D_Q \gamma + k_P S \frac{\partial \Theta}{\partial x} \right) dx \quad (3.66)$$

The parameter k_Q is a shear force distribution factor, which estimates the share of shear forces Q carried by the face sheet i . In analogous manner, k_P is the shear distribution factor related to the first derivative of local cell bending moment P .

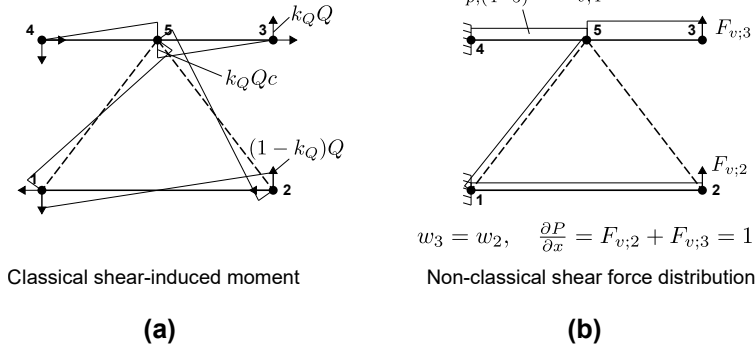


Figure 3.16. Shear analysis of a triangular core unit cell (a) concept of shear distribution factor k_Q and related shear-induced bending distribution (b) estimate of local face sheet shear factor $k_{\partial P}$ through an auxiliary frame model.

Assuming a linear transverse shear mechanism, k_Q may be estimated in an energy-consistent manner based on the mesoscopic mode Δ_3 . Figure 3.16 demonstrates the shear distribution factor for a triangular core cell and related shear-induced bending moment. Distribution factors for selected cells are presented in Chapter 4. The second term in the right-hand side of Eq. 3.66 is the face sheet component of the cell bending-related shear. From the macroscopic equations, $k_P = Et_f^3/(12S)$ is implied, yet this estimate is observed not to be generally accurate. An auxiliary model may be utilized to determine a more consistent k_P (Figure 3.16b), or alternatively $k_P \approx k_Q$ may be taken for simplicity.

The total stress at segment i is computed assuming the face sheets to

behave as conventional Euler-Bernoulli beams, that is

$$\hat{\sigma}_i(x_i, z_i) = \frac{\hat{N}_i}{t_f} + \frac{12\hat{P}_i z_i}{t_f^3} \quad (3.67)$$

where z_i is the local face coordinate (see Figure 3.15). Writing the microscopic stress distribution in the macroscopic coordinate system is straightforward by relating x_i to x . This way, the face sheet stress equation may be implemented as a direct macroscopic output.

3.6 Finite element scheme

The macroscopic equations of the present approach are solved using the finite element method in conjunction with an implicit solver for nonlinear algebraic equations. In the sections that follow, a finite element model is presented along with a modified Newton-Raphson implementation that includes scale iterations. Auxiliary finite element matrices and resulting secant and tangent stiffness matrices are presented in Appendix A.

3.6.1 Finite element model

Consider the two-noded couple stress finite element $\Omega^e(x_a, x_b)$ derived in Ref. [57] as an extension of the element in Arbind and Reddy [7]. The element is demonstrated in Figure 3.17.

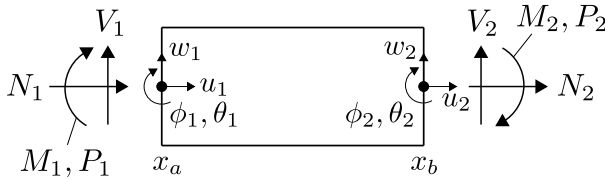


Figure 3.17. Finite element model as utilized to solve the macroscopic equilibrium equations [57].

The generalized displacements at the elemental end nodes 1 and 2 are given by

$$u_1 = u(x_a), \quad u_2 = u(x_b) \quad (3.68a)$$

$$\phi_1 = \phi(x_a), \quad \phi_2 = \phi(x_b) \quad (3.68b)$$

$$w_1 = \bar{\Delta}_1 = w(x_a), \quad w_2 = \bar{\Delta}_3 = w(x_b) \quad (3.68c)$$

$$\theta_1 = \bar{\Delta}_2 = \theta(x_a), \quad \theta_2 = \bar{\Delta}_4 = \theta(x_b) \quad (3.68d)$$

and, similarly, the generalized forces are obtained [57]

$$N_1 = -N(x_a), \quad N_2 = N(x_b) \quad (3.69a)$$

$$M_1 = -M(x_a), \quad M_2 = M(x_b) \quad (3.69b)$$

$$V_1 = -V(x_a), \quad V_2 = V(x_b) \quad (3.69c)$$

$$P_1 = -P(x_a), \quad P_2 = P(x_b) \quad (3.69d)$$

The generalized displacement vector can be written as

$$\mathbf{u}_e = \{u_1 \ \phi_1 \ w_1 \ \theta_1 \ u_2 \ \phi_2 \ w_2 \ \theta_2\}^T \quad (3.70)$$

whereas the generalized nodal force vector is given by

$$\mathbf{F}_e = \{N_1 \ M_1 \ V_1 \ P_1 \ N_2 \ M_2 \ V_2 \ P_2\}^T \quad (3.71)$$

The primary variables u , w and ϕ are approximated within the elemental domain as follows

$$u(x) = \sum_{i=1}^2 u_i \psi_i, \quad \phi(x) = \sum_{i=1}^2 \phi_i \psi_i, \quad w(x) = \sum_{i=1}^4 \bar{\Delta}_i \varphi_i \quad (3.72)$$

where ψ_i and φ_i are, respectively, the Lagrange linear polynomials and Hermitian cubic polynomials, whose definitions are reproduced in Appendix A. The finite element equations are developed following the approach in Wood and Zienkiewicz [176]. Only nodal forces are assumed to be present.

The strain vector is approximated from nodal displacements as

$$\epsilon = \left(\mathbf{B} + \frac{1}{2} w' \mathbf{B}_\sigma \right) \mathbf{u}_e \quad (3.73)$$

where the prime denotes differentiation with respect to x . The elemental secant stiffness matrix can be determined from the virtual work statement (Eq. 3.4) as

$$\mathbf{K}_e = \int_{x_a}^{x_b} \left(\mathbf{B} + w' \mathbf{B}_\sigma \right)^T \mathbf{C}_e \left(\mathbf{B} + \frac{1}{2} w' \mathbf{B}_\sigma \right) dx \quad (3.74)$$

and shown element-wise in Appendix A. The force-displacement equilibrium is given by

$$\mathbf{F}_e = \mathbf{K}_e(\mathbf{u}_e) \mathbf{u}_e \quad (3.75)$$

In the general case, the internal elemental force $\mathbf{K}_e \mathbf{u}_e$ is function of the displacement vector due to macroscopic and/or microscopic nonlinearities.

3.6.2 Nonlinear finite element solution

The nonlinear finite element equations depart from the notion that the internal and external force vector balance fulfills global equilibrium

$$\mathbf{R} = \mathbf{F}_{int} - \mathbf{F}_{ext} \rightarrow 0 \quad (3.76)$$

Equilibrium is sought using the Newton iterative method. Time discretization is employed and the residual expanded using Taylor series to the first-order term. Based on the known solution $\mathbf{u}^{(r-1)}$ the updated residual at iteration r is estimated as [144]

$$\mathbf{R}(\mathbf{u}^{(r)}) = \mathbf{R}(\mathbf{u}^{(r-1)}) + \left. \frac{\partial \mathbf{R}}{\partial \mathbf{u}} \right|_{\mathbf{u}^{(r-1)}} \delta \mathbf{u} + \mathcal{O}(\Delta \mathbf{u})^2 \quad (3.77)$$

where $\delta \mathbf{u} = \mathbf{u}^{(r)} - \mathbf{u}^{(r-1)}$. Therefore,

$$\delta \mathbf{u} = -\mathbf{T}^{-1} \mathbf{R} \quad (3.78)$$

and

$$\mathbf{u}^{(r)} = \mathbf{u}^{(r-1)} + \delta \mathbf{u} \quad (3.79)$$

The tangent stiffness matrix is defined for the element $\Omega^e(x_a, x_b)$ as

$$\mathbf{T}_e = \frac{\partial \mathbf{R}_e}{\partial \mathbf{u}_e} \equiv \frac{\partial \mathbf{F}_e}{\partial \mathbf{u}_e} = \mathbf{K}_e + \frac{\partial \mathbf{K}_e}{\partial \mathbf{u}_e} \mathbf{u}_e \quad (3.80)$$

and shown in detail in Appendix A. Equation 3.80 implies that the exact tangent stiffness matrix depends on constitutive matrix variations, which are assumed to be small in consecutive iterations, $\partial \mathbf{C} / \partial \mathbf{u} \rightarrow 0$.

The global finite element equations result from assembling individual elements. Numerical integration (Gauss quadrature) is utilized to compute the matrix elements. Membrane and shear locking are avoided by utilizing selective Gauss quadrature for the affected terms. Details on the element assembly procedure or numerical integration are omitted as they follow concepts for conventional finite elements, see Ref. [144] for a comprehensive description.

Algorithm 1 summarizes the main concepts for a Newton-Raphson implementation of the approach with embedded scale transitions. The constitutive matrix update procedure is summarized in Algorithm 2. In a simplified methodology, constitutive updates are conducted once per increment based on the predictor solution, what may require small increments for convergence.

Algorithm 1: Arbitrary step of the Newton-Raphson iterative method with scale transitions.

Data: Displacement vector $\mathbf{u}^{(t-1)}$ and external force vector $\mathbf{F}_{ext}^{(t-1)}$ at step $t - 1$.

Result: Updated $\mathbf{u}^{(t)}$, step t .

Do $\mathbf{F}_{ext}^{(t)} = \mathbf{F}_{ext}^{(t-1)} + \Delta \mathbf{F}_{ext}$, set iteration $r = 1$;

while $\|\mathbf{R}\| > \varepsilon_{tol}$ **do**

1. Compute elemental tangent stiffness $\mathbf{T}_e(\mathbf{u}_e^{(r-1)}, \mathbf{C}^{(r-1)})$ and residual $\mathbf{R}_e(\mathbf{u}_e^{(r-1)}, \mathbf{C}^{(r-1)})$, assemble global \mathbf{T} and \mathbf{R} ;
2. Apply boundary conditions to global system, solve $\mathbf{u}^{(r)} = \mathbf{u}^{(r-1)} - \mathbf{T}^{-1} \mathbf{R}$;
3. Update constitutive matrix $\mathbf{C}^{(r)} = f(\mathbf{u}^{(r)}, \omega)$ (Algorithm 2) ;
4. Compute force vector $\mathbf{F}_{int;e}$ and assemble global \mathbf{F}_{int} ;
5. Apply boundary conditions and evaluate residual $\mathbf{R} = \mathbf{F}_{int} - \mathbf{F}_{ext}^{(t)}$;
5. Update $r = r + 1$;

end

Write converged step parameters: $\mathbf{u}^{(t)}$, $\mathbf{C}^{(t)}$;

Obtain internal forces and post-process ω_i stresses (Section 3.5)

Algorithm 2: Constitutive matrix update procedure

Data: Displacement vector $\mathbf{u}^{(r-1)}$, 2-D geometry ($\omega(x)$), unit cell stiffness relations (Section 3.2.3, Section 4), microscopic equations (Section 3.3).

Result: Updated $\mathbf{C}^{(r)}$ at increment r .

1. Compute strains ϵ based on the displacement field, average over intervals $\bar{\epsilon}_j$ and $\bar{\epsilon}_k$ (Eq. 3.61) ;
 2. Compute average microscopic forces $\bar{N}_i(\mathbf{u}^{(r)})$ and $\bar{P}_i(\mathbf{u}^{(r)})$ (Eq. 3.59) ;
 3. Update $\mathbf{C}^{(r)}(\mathbf{u}^{(r)}, \omega)$ (Eq. 3.63) ;
-

Algorithm 3 summarizes an arc-length implementation based on the Riks Method that can overcome limit points. The arc-length solver uses the Feng continuation criterion to determine the increment direction, as described in Refs. [37, 46]. Details of Newton-type solvers in their standard format may be found, for instance, in Refs. [35, 36, 144]. The steps provided are mainly based on Ref. [144] and Ref. [37].

Algorithm 3: Arbitrary step of an arc-length method with scale transitions.

Data: Displacement vector $\mathbf{u}^{(t-1)}$, reference force vector $\bar{\mathbf{F}}_{ext}$, load multiplier $\lambda^{(t-1)}$.

Result: Updated $\mathbf{u}^{(t)}$, step t .

Set iteration $r = 1$;

while $\|\mathbf{R}\| > \varepsilon_{tol}$ **do**

if $r = 1$ **then**

1. Compute elemental tangent stiffness $\mathbf{T}_e(\mathbf{u}_e^{(t-1)}, \mathbf{C}_e^{(t-1)})$ and assemble global \mathbf{T} . Set residual vector \mathbf{R} due to load increment. Compute load-controlled displacement increment $\delta \bar{\mathbf{u}}^{(r)} = -\mathbf{T}^{-1} \mathbf{R}$;
2. Apply boundary conditions and compute the tangential displacement increment $\delta \hat{\mathbf{u}}^{(r)} = \mathbf{T}^{-1} \bar{\mathbf{F}}_{ext}$;
3. Calculate the predictor increment $\delta \lambda^{(r)} = \pm \hat{l} (\delta \hat{\mathbf{u}}^{(r)} \delta \hat{\mathbf{u}}^{(r)})^{-1}$, where $\hat{l} = \hat{l}_0 \sqrt{[\delta \hat{\mathbf{u}}^{(r)}]^T \delta \hat{\mathbf{u}}^{(r)}}$ is the arc-length increment. Define the increment sign: $\text{sign}(\delta \lambda) = \text{sign}(\delta \mathbf{u}^{(t-1)} \delta \hat{\mathbf{u}}^{(r)})$;
4. Compute the displacement increment $\delta \mathbf{u}^{(r)} = \delta \bar{\mathbf{u}}^{(r)} + \delta \lambda \delta \hat{\mathbf{u}}^{(r)}$;
5. Update the global variables $\mathbf{u}^{(r)} = \mathbf{u}^{(t-1)} + \delta \mathbf{u}^{(r)}$, $\lambda^{(r)} = \lambda^{(t-1)} + \delta \lambda^{(r)}$;
6. Update constitutive matrix $\mathbf{C}^{(r)} = f(\mathbf{u}^{(r)}, \omega)$ (Algorithm 2) ;
7. Compute force vector $\mathbf{F}_{int;e}$ and assemble global \mathbf{F}_{int} ;
8. Apply boundary conditions and evaluate residual $\mathbf{R} = \mathbf{F}_{int} - \lambda^{(r)} \bar{\mathbf{F}}_{ext}$;
9. Update $r = r + 1$;

else

1. Update the tangent stiffness matrix $\mathbf{T}(\mathbf{u}^{(r-1)}, \mathbf{C}^{(r-1)})$;
2. Compute $\delta \bar{\mathbf{u}}^{(r)} = -\mathbf{T}^{-1} \mathbf{R}$ and $\delta \hat{\mathbf{u}}^{(r)} = \mathbf{T}^{-1} \bar{\mathbf{F}}$;
3. Compute the incremental load parameter $a_1(\delta \lambda)^2 + 2a_2\delta \lambda + a_3 = 0$, where $a_1 = [\delta \hat{\mathbf{u}}^{(r)}]^T \delta \hat{\mathbf{u}}^{(r)}$, $a_2 = [\delta \bar{\mathbf{u}}^{(r)} + \Delta \mathbf{u}^{(r-1)}]^T \delta \hat{\mathbf{u}}^{(r)}$, $a_3 = [\delta \bar{\mathbf{u}}^{(r)} + \Delta \mathbf{u}^{(r-1)}]^T (\delta \bar{\mathbf{u}}^{(r)} + \Delta \mathbf{u}^{(r-1)}) - \hat{l}^2$. Select the root that provides the largest dot product between previous and current solution $\delta \lambda^{t,r} = \arg \max \{ [\Delta \mathbf{u}^{(r-1)}]^T (\Delta \mathbf{u}^{(r-1)} + \delta \bar{\mathbf{u}}^{(r)} + \delta \lambda_i \delta \hat{\mathbf{u}}^{(r)}) \}$;
4. Compute the displacement increment $\delta \mathbf{u}^{(r)} = \delta \bar{\mathbf{u}}^{(r)} + \delta \lambda^{(r)} \delta \hat{\mathbf{u}}^{(r)}$;
5. Update the global variables $\mathbf{u}^{(r)} = \mathbf{u}^{(t-1)} + \Delta \mathbf{u}^{(r-1)} + \delta \mathbf{u}^{(r)}$;
5. Update constitutive matrix $\mathbf{C}^{(r)} = f(\mathbf{u}^{(r)}, \omega)$ (Algorithm 2) ;
6. Compute force vector $\mathbf{F}_{int;e}$ and assemble global \mathbf{F}_{int} ;
7. Apply boundary conditions and evaluate residual $\mathbf{R} = \mathbf{F}_{int} - \lambda^{(r)} \bar{\mathbf{F}}_{ext}$;
8. Update $r = r + 1$;

end

Write converged step parameters: $\mathbf{u}^{(t)}$, $\lambda^{(t)}$, $\mathbf{C}^{(t)}$. Adjust arc-length ;

Obtain internal forces and post-process ω_i stresses (Section 3.5)

end

4. Analysis of selected unit cells

This chapter employs the definitions of Chapter 3 in the analysis of selected corrugated sandwich cells. Conventional linear frame analysis is employed along the mesoscopic relations and microscopic properties as to define homogenized stiffnesses of semi-rigid web-core and rigid triangular core, X-core, Y-core and hexagonal core cells. An approach extension for cells with higher vertical corrugation order is discussed. Shear distribution factors that result from the transverse shear boundary problems are provided. The core rotational restraint that is input to the microscopic equations is presented for selected unit cells.

4.1 Homogenized stiffness properties

Stiffness properties are determined for selected unit cells based on the definitions and assumptions of Section 3.2.3. Unit cells with length s and depth d are discretized with linear elastic Euler-Bernoulli frame elements. All cells are symmetric about their mid-length vertical plane. Displacement boundary conditions (Eq. 3.29, Eq. 3.34 and Eq. 3.39) are enforced to the cell corner nodes **1-4** (Figs. 4.1-4.5), and the resulting boundary tractions are utilized in conjunction with Eq. 3.32, Eq. 3.36 and Eq. 3.40 to compute macroscopic stiffnesses. The unit cells are selected given their practical relevance and relative simplicity, what allows short stiffness expressions to be presented. Extension for other corrugated unit cells is straightforward when applying the same basic principles.

Considering the idealized micromechanical modes $\Delta_1 - \Delta_4$ (see Figure 3.9), boundary displacements are applied along conditions to prevent rigid-body motion. In mode Δ_3 , horizontal forces $F_{h,i}$ are enforced to the boundary nodes as to fulfill moment equilibrium. The boundary conditions for unit displacement $U^T = 1$ can be summarized as

Boundary conditions, idealized case Δ_1 :

$$U_{x;3} = U_{x;2} = -U_{x;4} = -U_{x;1} = 1 \quad (4.1a)$$

$$U_{z;5} = \frac{\partial U_{z;1}}{\partial x} = \frac{\partial U_{z;2}}{\partial x} = \frac{\partial U_{z;3}}{\partial x} = \frac{\partial U_{z;4}}{\partial x} = 0 \quad (4.1b)$$

Boundary conditions, idealized case Δ_2 :

$$U_{x;3} = U_{x;1} = -U_{x;2} = -U_{x;4} = 1 \quad (4.2a)$$

$$U_{z;5} = \frac{\partial U_{z;1}}{\partial x} = \frac{\partial U_{z;2}}{\partial x} = \frac{\partial U_{z;3}}{\partial x} = \frac{\partial U_{z;4}}{\partial x} = 0 \quad (4.2b)$$

Boundary conditions, idealized case Δ_3 :

$$U_{z;3} = U_{z;2} = -U_{z;1} = -U_{z;4} = 1 \quad (4.3a)$$

$$U_{x;5} = U_{z;5} = \frac{\partial U_{z;5}}{\partial x} = 0 \quad (4.3b)$$

$$F_{h;2} = F_{h;1} = -F_{h;3} = -F_{h;4} = \frac{s(F_v^t + F_v^b)}{2d} \quad (4.3c)$$

Boundary conditions, idealized case Δ_4 :

$$\frac{\partial U_{z;3}}{\partial x} = \frac{\partial U_{z;2}}{\partial x} = -\frac{\partial U_{z;1}}{\partial x} = -\frac{\partial U_{z;4}}{\partial x} = 1 \quad (4.4a)$$

$$U_{z;5} = \frac{\partial U_{z;5}}{\partial x} = U_{x;1} = U_{x;2} = U_{x;3} = U_{x;4} = 0 \quad (4.4b)$$

The reaction forces are defined according to Section 3.2.3. In relation to the nodal numbering adopted, the forces become

$$F_h^t = F_{h;3} = -F_{h;4}, \quad F_h^b = F_{h;2} = -F_{h;1} \quad (4.5a)$$

$$F_\theta^t = F_{\theta;3} = -F_{\theta;4}, \quad F_\theta^b = F_{\theta;2} = -F_{\theta;1} \quad (4.5b)$$

In modes Δ_1 , Δ_2 and Δ_4 , vertical forces $F_{v;i}$ are zero, and vertical displacements are unconstrained to fulfill the plane stress macroscopic condition. In the transverse shear derivations (Δ_3), boundary forces $F_{\theta;i}$ are zero, and rotations are unconstrained; the slopes are equal at opposite boundaries due to the mid-length vertical symmetry. The face sheet-related reaction force $F_{h,f}$ is function of the effective axial modulus \bar{E}_i . The subscript j refers to the top face sheet, while k refers to the bottom counterpart. In the linear case $\bar{E}_i = E$, whereas for a geometrically nonlinear microstructure it describes the axial stiffness reduction due to the progressive instability.

The following sections present stiffness analyses of selected unit cells. Boundary forces F_h, F_v, F_θ are presented per unit displacement U^Γ and per unit width. Stiffness expressions obtained are simplified by acknowledging that the members are thin-walled, that is, $t_f, t_c \ll s, d$.

4.1.1 Semi-rigid web-core unit cell

A web-core unit cell is analysed as a frame with 7 nodes and 6 elements. The connection between face sheets and core struts at nodes 6 and 7 is semi-rigid, implemented through a modification matrix (see, for example, Eq. 23.11 in Ref. [28]). The additional independent variable k_θ represents the connection rotational stiffness per unit width. The reaction forces related to the enforced displacement boundary conditions are provided as follows.

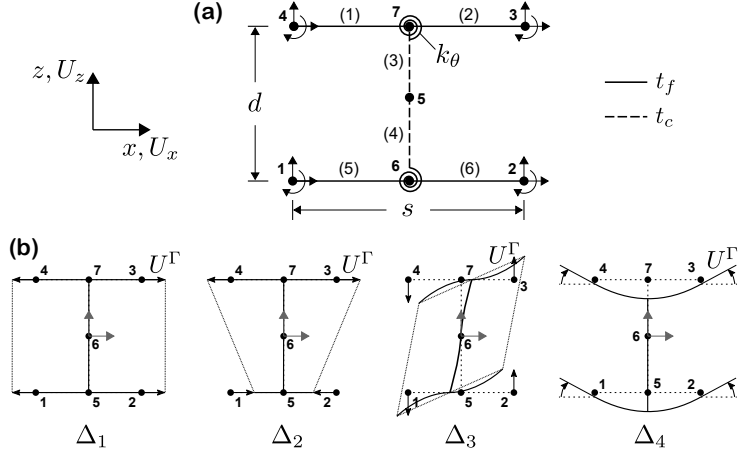


Figure 4.1. Mesoscale analysis of a web-core cell with semi-rigid joints (a) geometry and boundary forces (b) deformation modes.

Boundary reaction forces, idealized case Δ_1 :

$$F_h^t = \frac{2\bar{E}_j t_f}{s}, \quad F_h^b = \frac{2\bar{E}_k t_f}{s} \quad (4.6a)$$

$$F_\theta^t = F_\theta^b = 0 \quad (4.6b)$$

Boundary reaction forces, idealized case Δ_2 :

$$F_h^t = \frac{2\bar{E}_j t_f}{s}, \quad F_h^b = -\frac{2\bar{E}_k t_f}{s} \quad (4.7a)$$

$$F_\theta^t = F_\theta^b = 0 \quad (4.7b)$$

Boundary applied and reaction forces, idealized case Δ_3 :

The force boundary conditions for moment equilibrium are given by

$$F_{h;3} = F_{h;4} = -F_{h;1} = -F_{h;2} = \frac{2Ek_\theta t_f^3 t_c^3}{sd(Et_f^3 t_c^3 + 3dk_\theta t_f^3 + k_\theta s t_c^3)} \quad (4.8)$$

The boundary vertical reaction forces are

$$F_v^t = F_v^b = \frac{2Ek_\theta t_f^3 t_c^3}{s^2(Et_f^3 t_c^3 + 3dk_\theta t_f^3 + k_\theta s t_c^3)} \quad (4.9)$$

The face sheet shear distribution factor is $k_Q = 1/2$.

Boundary reaction forces, idealized case Δ_4 :

$$F_\theta^t = F_\theta^b = \frac{Et_f^3}{6s} \quad (4.10a)$$

$$F_h^t = F_h^b = 0 \quad (4.10b)$$

The stretch and local bending relations depend only on the face mechanical properties, implying that the core is an antiplane. The normal and couple stress-related stiffnesses can be written as

$$\bar{A} = (\bar{E}_j + \bar{E}_k)t_f \quad (4.11a)$$

$$\bar{D} = (\bar{E}_j + \bar{E}_k) \frac{t_f d^2}{4} \quad (4.11b)$$

$$S = \frac{Et_f^3}{6} \quad (4.11c)$$

$$\bar{C}_1 = (\bar{E}_j - \bar{E}_k) \frac{t_f d}{2} \quad (4.11d)$$

$$C_2 = C_3 = 0 \quad (4.11e)$$

The transverse shear stiffness D_Q [58] is given by

$$D_Q = \frac{2Ed^2 t_f^3 t_c^3}{s[k_1 d^2 t_f^3 t_c^3 + 2d^3 t_f^3 + s t_c^3 (d^2 + t_f^2)]}, \quad k_1 = \frac{E}{k_\theta} \quad (4.12)$$

The expression is function of face sheet and core strut bending stiffnesses. The transverse shear-carrying mechanism involves bending of the members, and the resulting stiffness is highly dependent on the rotational rigidity of the connection.

For a rigid thin-walled cell ($k_1 \rightarrow \infty$, $t_f \ll d$), the expression reduces to

$$D_{Q,rigid} \approx \frac{2Et_f^3 t_c^3}{s(2d t_f^3 + s t_c^3)} \quad (4.13)$$

The transverse stiffness relations are function of t_f^3, t_c^3 , indicating that the shear deformation results entirely from bending of the face sheet and core (web).

4.1.2 X-core unit cell

A regular X-core unit cell is analysed as a rigid frame with 5 nodes and 6 elements as represented in Figure 4.2. The core strut length is defined as $p = (1/2)\sqrt{d^2 + s^2}$. The boundary reaction forces related to the enforced displacement boundary conditions are presented as follows.

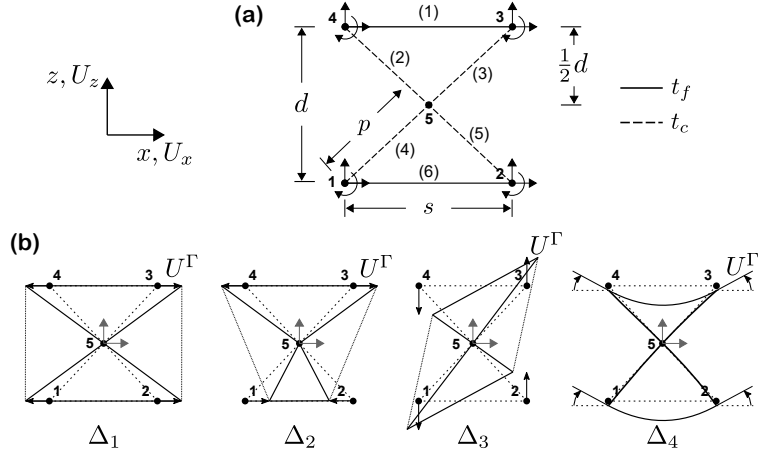


Figure 4.2. Mesoscale analysis of a X-core cell with rigid joints (a) geometry and boundary forces (b) deformation modes.

Boundary reaction forces, idealized case Δ_1 :

$$F_h^t = \frac{2\bar{E}_j t_f}{s} + \frac{4E p t_c^3}{d^2 p^2 + s^2 t_c^2}, \quad F_h^b = \frac{2\bar{E}_k t_f}{s} + \frac{4E p t_c^3}{d^2 p^2 + s^2 t_c^2} \quad (4.14a)$$

$$F_\theta^t = -\frac{E p d t_c^3}{p^2 d^2 + s^2 t_c^2}, \quad F_\theta^b = \frac{E p d t_c^3}{p^2 d^2 + s^2 t_c^2} \quad (4.14b)$$

Boundary reaction forces, idealized case Δ_2 :

$$F_h^t = \frac{2\bar{E}_j t_f}{s} + \frac{4E p t_c^3}{d^2 p^2 + s^2 t_c^2}, \quad F_h^b = -\frac{2\bar{E}_k t_f}{s} - \frac{4E p t_c^3}{d^2 p^2 + s^2 t_c^2} \quad (4.15a)$$

$$F_\theta^t = -\frac{E p d t_c^3}{p^2 d^2 + s^2 t_c^2}, \quad F_\theta^b = -\frac{E p d t_c^3}{p^2 d^2 + s^2 t_c^2} \quad (4.15b)$$

Boundary applied and reaction forces, idealized case Δ_3 :

The force boundary conditions for moment equilibrium are given by

$$F_{h;3} = F_{h;4} = -F_{h;1} = -F_{h;2} = \frac{E t_c (d^2 t_f^3 t_c^2 + 4s^2 p^2 t_f^3 + 2ps^3 t_c^3)}{2p^2 s d (3p t_f^3 + s t_c^3)} \quad (4.16)$$

The boundary vertical reaction forces are

$$F_v^t = F_v^b = \frac{Et_c(d^2t_f^3t_c^2 + 4s^2p^2t_f^3 + 2ps^3t_c^3)}{2p^2s^2(3pt_f^3 + st_c^3)} \quad (4.17)$$

The face sheet shear distribution factor for the X-core is obtained as

$$k_Q = \frac{2p^2t_f^3t_c^2}{(4s^2p^2 + d^2t_c^2)t_f^3 + 2ps^3t_c^3} \quad (4.18)$$

Boundary reaction forces, idealized case Δ_4 :

$$F_\theta^t = F_\theta^b = \frac{Et_f^3}{6s} + \frac{Et_c^3(4d^2p^2 + s^2t_c^2)}{12p(s^2t_c^2 + d^2p^2)} \quad (4.19a)$$

$$F_h^t = -F_h^b = -\frac{Epd t_c^3}{d^2p^2 + s^2t_c^2} \quad (4.19b)$$

Stiffness relations

Simplifying the force-strain relations, the stretch- and curvature-related stiffnesses result into

$$\bar{A} = (\bar{E}_j + \bar{E}_k)t_f + A_c \quad (4.20a)$$

$$\bar{D} = (\bar{E}_j + \bar{E}_k)\frac{t_f d^2}{4} + \frac{A_c d^2}{4} \quad (4.20b)$$

$$S = \frac{Et_f^3}{6} + \frac{Est_c^3}{3p} \quad (4.20c)$$

$$\bar{C}_1 = (\bar{E}_j - \bar{E}_k)\frac{t_f d}{2} \quad (4.20d)$$

$$C_2 = 0 \quad (4.20e)$$

$$C_3 = -\frac{A_c d^2}{8} \quad (4.20f)$$

where the face sheet terms are generally given in Eq. 4.11 and

$$A_c = \frac{4Est_c^3}{pd^2} \quad (4.21)$$

In absence of geometric nonlinearities, couplings between stretch modes Δ_1 and Δ_2 are zero, as the unit cell is symmetric about the horizontal axis. Coupling between stretch Δ_1 and curvature Δ_4 modes also become zero, as the reaction forces at top and bottom nodes are equal in magnitude and inverse sign, to a zero boundary average.

The transverse shear stiffness D_Q [59] may be simplified into

$$D_Q = \frac{Esd^2t_c}{4p^3} \quad (4.22)$$

a linear function of t_c , implying a core strut stretch-dominated transverse shear mechanism. The simplified shear stiffness is independent of the face sheet properties, as the transverse shear-carrying core struts of consecutive cells are directly connected.

4.1.3 Triangular core unit cell

A triangular core cell is analysed as a rigid frame with 5 nodes and 5 elements as represented in Figure 4.3. The core strut length is $p = \sqrt{c^2 + d^2}$. The boundary reaction forces related to the enforced displacement boundary conditions are presented as follows.

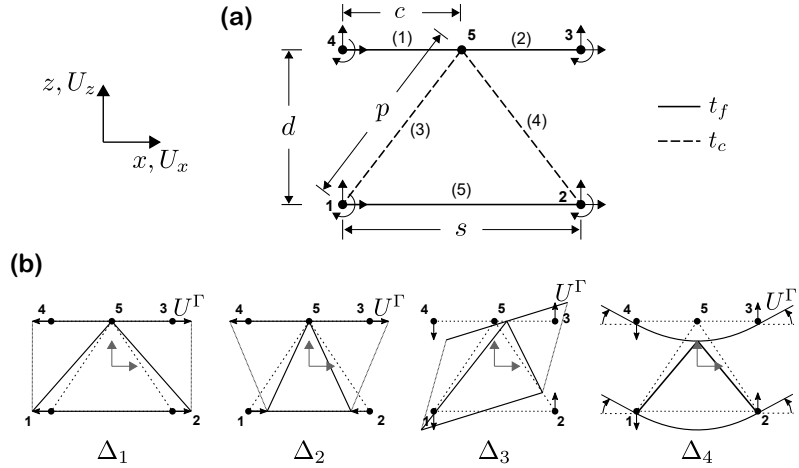


Figure 4.3. Mesoscale analysis of a triangular core cell with rigid joints (a) geometry and boundary forces (b) deformation modes.

Boundary reaction forces, idealized case Δ_1 :

$$F_h^t = \frac{2\bar{E}_j t_f}{s}, \quad F_h^b = \frac{2\bar{E}_k t_f}{s} + \frac{E p t_c^3}{d^2 p^2 + c^2 t_c^2} \quad (4.23a)$$

$$F_\theta^t = 0, \quad F_\theta^b = \frac{E p d t_c^3}{2(d^2 p^2 + c^2 t_c^2)} \quad (4.23b)$$

Boundary reaction forces, idealized case Δ_2 :

$$F_h^t = \frac{2\bar{E}_j t_f}{s}, \quad F_h^b = -\frac{2\bar{E}_k t_f}{s} - \frac{E p t_c^3}{d^2 p^2 + c^2 t_c^2} \quad (4.24a)$$

$$F_{\theta}^t = 0, \quad F_{\theta}^b = -\frac{Epd t_c^3}{2(d^2 p^2 + c^2 t_c^2)} \quad (4.24b)$$

Boundary applied and reaction forces, idealized case: Δ_3

The force boundary conditions for moment equilibrium are given by

$$F_{h;3} = F_{h;4} = -F_{h;2} = -F_{h;1} = -\frac{E(2c^3 p t_c^3 + c^2 p^2 t_f^3 + d^2 t_f^3 t_c^2)}{c^2 d p^2 t_c^2} \quad (4.25)$$

The boundary vertical reaction forces are

$$F_v^t = -\frac{E t_f^3}{2c^3} \quad (4.26a)$$

$$F_v^b = -\frac{E[2c^2 p^2 t_f^3 + (d^2 - c^2) t_c^2 t_c^3 + 4c^3 p t_c^3]}{2c^3 p^2 t_c^2} \quad (4.26b)$$

The shear distribution factor for the triangular core may be simplified as

$$k_Q = \frac{p t_f^3 t_c^2}{2c^2(p t_f^3 + 2c t_c^3)} \quad (4.27)$$

Boundary reaction forces, idealized case Δ_4 :

$$F_{\theta}^t = \frac{E t_f^3}{12c}, \quad F_{\theta}^b = \frac{E t_f^3}{12c} + \frac{E t_c^3(4d^2 p^2 + c^2 t_c^2)}{12p(c^2 t_c^2 + d^2 p^2)} \quad (4.28a)$$

$$F_h^t = 0, \quad F_h^b = \frac{Epd t_c^3}{2(c^2 t_c^2 + d^2 p^2)} \quad (4.28b)$$

Stiffness relations

Simplifying the force-strain relations, the stretch- and curvature-related stiffnesses result into

$$\bar{A} = (\bar{E}_j + \bar{E}_k) t_f + A_c \quad (4.29a)$$

$$\bar{D} = (\bar{E}_j + \bar{E}_k) \frac{t_f d^2}{4} + \frac{A_c d^2}{4} \quad (4.29b)$$

$$S = \frac{E t_f^3}{6} + \frac{E c t_c^3}{3p} \quad (4.29c)$$

$$\bar{C}_1 = (\bar{E}_j - \bar{E}_k) \frac{t_f d}{2} - \frac{A_c d}{2} \quad (4.29d)$$

$$C_2 = \frac{A_c d}{2} \quad (4.29e)$$

$$C_3 = -\frac{A_c d^2}{4} \quad (4.29f)$$

where

$$A_c = \frac{Ect_c^3}{pd^2} \quad (4.30)$$

Even at the linear case, all coupling stiffnesses are non-zero as the unit cell does not have a horizontal symmetry plane.

The transverse shear stiffness D_Q may be simplified into [59]

$$D_Q = \frac{Ecd^2t_ft_c}{p^3t_f + c^3t_c} \quad (4.31)$$

The resulting expression is a linear function of t_f and t_c , implying face sheet and core stretch-dominated shear deformation.

4.1.4 Y-core unit cell

A Y-core cell with 6 nodes and 6 elements is shown in Figure 4.4. The Y-core frame is said *regular*; the inclined core struts connect to neighboring cells at nodes 3 and 4, and node 5 is located at $z = d/2$. In comparison with a generic Y-core (see Figure 5.2), the amount of independent parameters is reduced and closed-form equations are short. The reaction forces relate to the enforced boundary displacements are presented as follows.

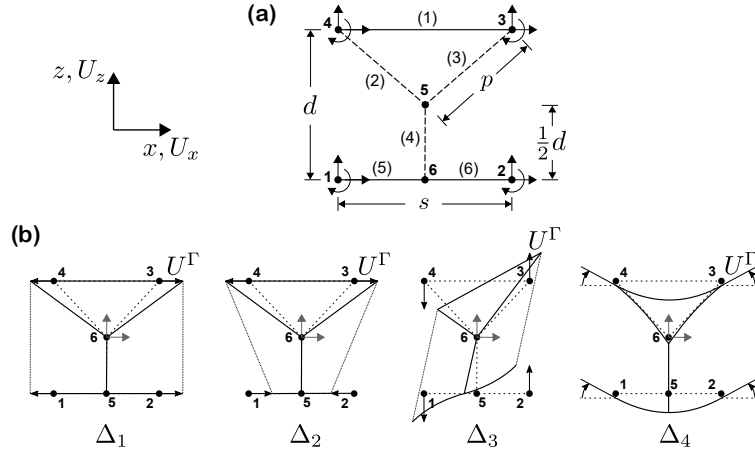


Figure 4.4. Mesoscale analysis of a Y-frame cell with rigid joints (a) geometry and boundary forces (b) deformation modes.

Boundary reaction forces, idealized case Δ_1 :

$$F_h^t = \frac{2\bar{E}_j t_f}{s} + \frac{4Ept_c^3}{d^2 p^2 + s^2 t_c^2}, \quad F_h^b = \frac{2\bar{E}_k t_f}{s} \quad (4.32a)$$

$$F_\theta^t = \frac{Epd t_c^3}{d^2 p^2 + s^2 t_c^2}, \quad F_\theta^b = 0 \quad (4.32b)$$

Boundary reaction forces, idealized case Δ_2 :

$$F_h^t = \frac{2\bar{E}_j t_f}{s} + \frac{4E p t_c^3}{d^2 p^2 + s^2 t_c^2}, \quad F_h^b = -\frac{2\bar{E}_k t_f}{s} \quad (4.33a)$$

$$F_\theta^t = \frac{E p d t_c^3}{d^2 p^2 + s^2 t_c^2}, \quad F_\theta^b = 0 \quad (4.33b)$$

Boundary applied and reaction forces, idealized case: Δ_3

The force boundary conditions for moment equilibrium are given by

$$F_{h;3} = F_{h;4} = -F_{h;2} = -F_{h;1} = \frac{E \{3[4p^2 s^2 (4d+p) + 4d^2 t_c^2 (d+p)] t_f^6 + 4[2ps^3 (3d+2p) + d^2 s t_c^2] t_f^3 t_c^3 + 4ps^4 t_c^6\}}{s^2 d \{ (3[2p^2 s^2 (p+2d) + t_c^2 (d^3 + 2d^2 p + 4p^3)] t_f^3 + [s t_c^2 (d^2 + 4p^2) + 2ps^3 (2p+3d)] t_c^3 \}} \quad (4.34)$$

The boundary reaction forces are given by

$$F_v^t = \frac{E \{ [6t_c^2 [d^2 (3d+p) - ps^2] + 12p^2 s^2 (6d+p)] t_f^6 + [2st_c^3 (2d^2 - s^2)] t_f^3 t_c^3 + 8ps^4 t_c^6 \}}{[3ps^2 + d^2 (d+3p)] t_c^2 + 6p^2 s^2 (2d+p)] t_f^3 + [2p(3d+2p)s^3 + st_c^2 (d^2 + 4p^2)] t_c^3} \quad (4.35a)$$

$$F_v^b = \frac{2E t_f^3}{s^3} \quad (4.35b)$$

The shear distribution factor may be simplified as

$$k_Q = \frac{3p(2d+p)t_f^6 + s(3d+2p)t_f^3 t_c^3}{6p(4d+p)t_f^6 + 4(3d+2p)st_f^3 t_c^3 + 2s^2 t_c^6} \quad (4.36)$$

Boundary reaction forces, idealized case Δ_4 :

$$F_\theta^t = \frac{E t_f^3}{6s} + \frac{E t_c^3 (4d^2 p^2 + s^2 t_c^2)}{12p(d^2 p^2 + s^2 t_c^2)}, \quad F_\theta^b = \frac{E t_f^3}{6s} \quad (4.37a)$$

$$F_h^b = 0, \quad F_h^t = \frac{E p d t_c^3}{d^2 p^2 + s^2 t_c^2} \quad (4.37b)$$

Stiffness relations

Simplifying the force-strain relations, the stretch- and curvature-related stiffnesses result into

$$\bar{A} = (\bar{E}_j + \bar{E}_k) t_f + A_c \quad (4.38a)$$

$$\bar{D} = (\bar{E}_j + \bar{E}_k) \frac{t_f d^2}{4} + \frac{A_c d^2}{4} \quad (4.38b)$$

$$S = \frac{E t_f^3}{6} + \frac{E s t_c^3}{6p} \quad (4.38c)$$

$$\bar{C}_1 = (\bar{E}_j - \bar{E}_k) \frac{t_f d}{2} + \frac{A_c d}{2} \quad (4.38d)$$

$$C_2 = \frac{A_c d}{4} \quad (4.38e)$$

$$C_3 = \frac{A_c d^2}{8} \quad (4.38f)$$

where

$$A_c = \frac{2E s t_c^3}{p d^2} \quad (4.39)$$

Even in a linear formulation, all coupling stiffnesses are non-zero as the unit cell does not have a horizontal symmetry plane.

The transverse shear stiffness D_Q may be simplified into

$$D_Q = \frac{8E t_c^3}{s} \left[\frac{3p(4d+p)t_f^6 + 2s(3d+2p)t_f^3 t_c^3 + s^2 t_c^6}{12pd(d+p)t_f^6 + 2s(3d^2+8dp+3p^2)t_f^3 t_c^3 + 4s^2(d+p)t_c^6} \right] \quad (4.40)$$

The expression implies that the transverse shear mechanism is governed by the bending of the face sheets and core struts. Connection semi-rigidity may be relevant for the stiffness response, and may be incorporated in analogous way as for the web-core cell.

4.1.5 Hexagonal cell

For a regular hexagonal cell with corrugation order $n = 1$ as shown in Figure 4.5, the side length p is the only independent variable. The side length relates to the general unit cell dimensions by $s = 3p$ and $d = \sqrt{3}p$. Unlike the unit cells previously shown, the face sheet and core stiffnesses are coupled due to the discontinuous core. The core struts have, however, limited impact in the stretch- and curvature-related stiffnesses. The reaction forces relate to the enforced boundary displacements are presented for the linear case as follows. The geometric nonlinear case may be considered based on an antiplane core approximation.

Boundary reaction forces, idealized case Δ_1 (linear):

$$F_h^{t;l} = F_h^{b;l} = \frac{2E t_f [(9p^2 + 15t_c^2)t_f^4 + 12t_f^3 t_c^3 + (12p^2 + 5t_c^2)t_f^2 t_c + 4t_c^6]}{p[(27p^2 + 45t_c^2)t_f^4 + 12t_c^3 t_f^3 + (36p^2 + 15t_c^2)t_f t_c^3 + 4t_c^6]} \quad (4.41a)$$

$$F_\theta^{t;l} = -F_\theta^{b;l} = \frac{4\sqrt{3}E t_f^4 t_c^3}{(27p^2 + 45t_c^2)t_f^4 + 12t_c^3 t_f^3 + (36p^2 + 15t_c^2)t_f t_c^3 + 4t_c^6} \quad (4.41b)$$

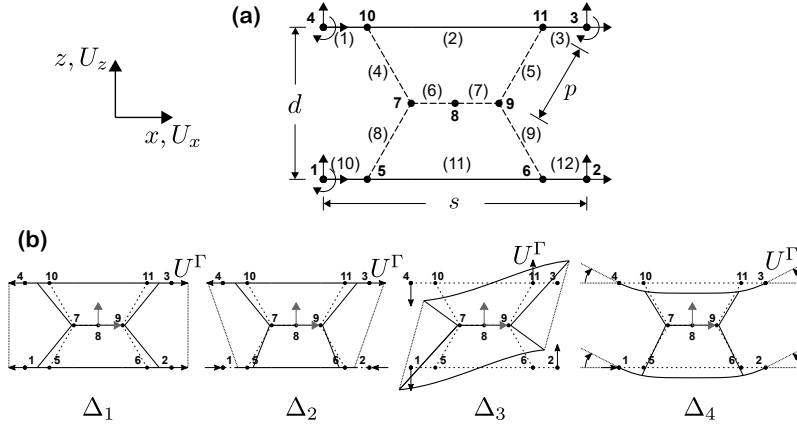


Figure 4.5. Mesoscale analysis of a hexagonal cell with rigid joints (a) geometry and boundary forces (b) deformation modes.

Boundary reaction forces, idealized case Δ_2 (linear):

$$F_h^{t;l} = -F_h^{b;l} = \frac{2Et_f[(45p^2 + 6t_c^2)t_f^4 + 24t_f^3t_c^3 + (48p^2 + t_c^2)t_ft_c^3 + 4t_c^6]}{p[(135p^2 + 18t_c^2)t_f^4 + 24t_f^3t_c^3 + (144p^2 + 3t_c^2)t_ft_c^3 + 4t_c^6]} \quad (4.42a)$$

$$F_\theta^{t;l} = F_\theta^{b;l} = \frac{12\sqrt{3}E_f^4t_c^3}{(135p^2 + 18t_c^2)t_f^4 + 24t_f^3t_c^3 + (144p^2 + 3t_c^2)t_ft_c^3 + 4t_c^6} \quad (4.42b)$$

Boundary applied and reaction forces, idealized case Δ_3 :

The force boundary conditions for moment equilibrium are given by

$$F_{h;3} = F_{h;4} = -F_{h;1} = -F_{h;2} = \frac{2\sqrt{3}Et_f^3t_c^3(16p^2t_c^3 + 32p^2t_f^3 + 3t_f^3t_c^2)}{16p^5t_c^6 - 96p^5t_f^3t_c^3 - 216p^5t_f^6 + 51p^3t_f^3t_c^5 + 189p^3t_f^6t_c^2} \quad (4.43)$$

The boundary vertical reaction forces are

$$F_v^t = F_v^b = \frac{2Et_f^3t_c^3(16p^2t_c^3 + 32p^2t_f^3 + 3t_f^3t_c^2)}{16p^5t_c^6 - 96p^5t_f^3t_c^3 - 216p^5t_f^6 + 51p^3t_f^3t_c^5 + 189p^3t_f^6t_c^2} \quad (4.44)$$

The shear distribution factor over the boundary segments is $k_Q = 1/2$.

Boundary reaction forces, idealized case Δ_4 :

$$F_\theta^t = F_\theta^b = \frac{Et_f^3[(45p^2 + 6t_c^2)t_f^4 + 8t_f^3t_c^3 + (144p^2 + 3t_c^2)t_ft_c^3 + 4t_c^6]}{6p[(135p^2 + 18t_c^2)t_f^4 + 24t_f^3t_c^3 + (144p^2 + 3t_c^2)t_ft_c^3 + 4t_c^6]} \quad (4.45a)$$

$$F_h^t = F_h^b = -\frac{12\sqrt{3}Et_f^4t_c^3}{(135p^2 + 18t_c^2)t_f^4 + 24t_f^3t_c^3 + (144p^2 + 3t_c^2)t_ft_c^3 + 4t_c^6} \quad (4.45b)$$

Stiffness relations

Considering a linear microscale, the stiffnesses may be approximated as

$$A \approx 2Et_f \quad (4.46a)$$

$$D \approx \frac{3Et_f p^2}{2} \quad (4.46b)$$

$$S = \frac{Et_f^3(5t_f^3 + 16t_c^2)}{30t_f^3 + 32t_c^3} \quad (4.46c)$$

$$C_1 = C_2 = 0 \quad (4.46d)$$

$$C_3 = -\frac{6Et_f^3 t_c^3}{15t_f^3 + 16t_c^3} \quad (4.46e)$$

An order of magnitude analysis reveals that the face sheets strongly command the response under idealized stretches.

The transverse shear stiffness D_Q may be simplified into

$$D_Q = \frac{48E(2t_f^3 + t_c^3)t_f^3 t_c^3}{p^2(63t_f^6 + 48t_f^3 t_c^4 + 8t_c^6)} \quad (4.47)$$

which contains combinations of the bending stiffness of the face sheets and core struts; the transverse shear mechanism is bending-dominated. Connection semi-rigidity may be relevant for the stiffness response, and may be incorporated in analogous way as for the web-core cell.

4.1.6 Cells with higher vertical corrugation order

The stiffness derivations as presented are valid for cores with a single order of corrugation, $n = 1$, that is, connected to neighboring cells through top and bottom corners with a void core interface. Stiffnesses for cells with higher corrugation order (i.e. $n > 1$, see Figure 4.6) may be derived following the same basic instructions, with few additional observations.

In relation to the micromechanical approach proposed, the boundary displacements U^Γ must be applied as to produce a constant displacement ($\Delta_1, \Delta_3, \Delta_4$) or linear variation (Δ_2) over the unit cell height. Analogously, boundary forces or the induced moment are summed over the boundary. Horizontal forces for moment equilibrium in Δ_3 must be assessed over the entire boundary. The general averaging rules presented are, in general, equally applicable.

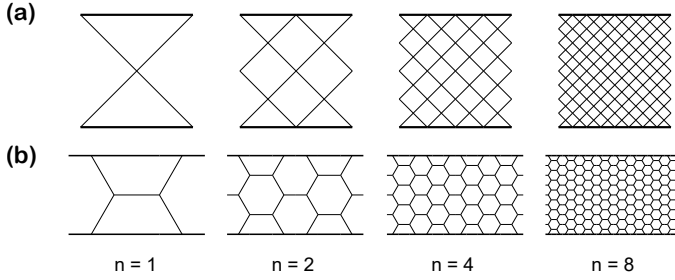


Figure 4.6. (a) Diamond (X-core, ≥ 1) and (b) honeycomb (Hexagonal, ≥ 1) unit cells with different vertical corrugation orders.

4.2 Core rotational stiffnesses

The nonlinear microscopic equations contain a core-dependent spring constant k_c , which accounts for the rotational restraint of the core. The stiffness provided by the core is function of the strut length and connectivity, and may be described using bounds, as it depends on the global behavior of the structure. Generally, for a cell without internal hard points

$$k_c = \frac{M_i(x_a)}{\theta_i(x_a)} = \frac{M_i(x_b)}{\theta_i(x_b)} \quad (4.48)$$

where M_i is the bending moment and θ_i the slope at the core support, respectively. The equality at the opposite ends results from a periodic or antiperiodic behavior assumption.

The bound idealizations for three simple cores are shown in Figure 4.7 and a qualitative description presented next; lower-bounds may be conservatively chosen in practical design. Derivation for other cores is analogous.

Web-core cell

Figure 4.7a shows a web-core *box* cell. The webs act as pinned beams with end-moments, with signs depending on the shear and second-order deformations. When secondary bending is dominant, k_c lies within

$$k_{asym} \leq k_c \leq k_{sym}, \quad k_{asym} = \frac{2EI_c}{d} = \frac{Et_c^3}{12d}, \quad k_{sym} = \frac{6EI_c}{d} = \frac{Et_c^3}{4d} \quad (4.49)$$

where I_c corresponds to half the bending stiffness of each web. The bounds depend whether local buckling is symmetric (k_{sym} , Fig. 4.7a;i), anti-symmetric (k_{asym} , Fig. 4.7a;ii) or present in a single face sheet (intermediate case).

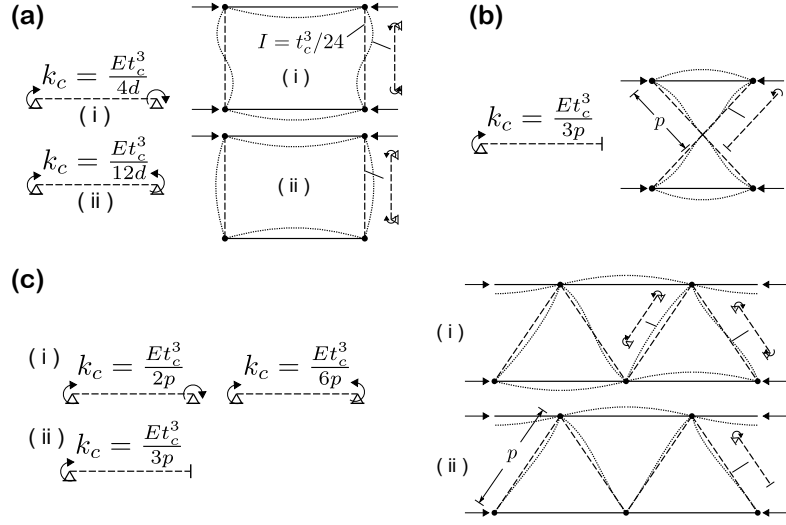


Figure 4.7. Idealizations to estimate effective core spring constants k_c (a) web-core (b) X-core (c) triangular-core.

X-core cell

The core rotational restraint k_c is estimated by considering the central node (Figure 4.7b) as a rigid due to the converging core struts (pinned-fixed)

$$k_c \approx \frac{4EI_c}{p} = \frac{Et_c^3}{3p} \quad (4.50)$$

Triangular-core cell

For case (i) in (Figure 4.7c, k_c may be estimated based on the modes related to the horizontal offset (average between symmetric and anti-symmetric)

$$k_c \approx \frac{1}{2} \left(\frac{6EI_c}{p} + \frac{2EI_c}{p} \right) = \frac{4EI_c}{p} = \frac{Et_c^3}{3p} \quad (4.51)$$

If buckling is confined to a single face sheet (case ii)

$$k_c \approx \frac{4EI_c}{p} = \frac{Et_c^3}{3p} \quad (4.52)$$

a fixed-pinned idealization that leads to the same k_c as Eq. 4.51.

5. Linear model and validations

This chapter defines a macroscopically linear couple stress sandwich model that is also independent of microscopic nonlinear effects. The macroscale in Section 3.2 and the related finite element of Section 3.6 are simplified as defined in Ref. [57]. An eigenvalue problem is set up to predict global buckling loads. Equivalence with the classical thick-face sandwich beam model is discussed. Validations in linear bending (deflections and stress distributions) and critical buckling loads are conducted along with comparisons with other homogenized beam models.

5.1 Two-scale linear model

The approach presented in Chapter 3 contains three interacting scales, two of which are nonlinear. Linearization demands simplifications:

- The von Kármán nonlinear term is removed from the macroscopic couple stress model;
- Strain-independent face sheet stiffness terms are analytically determined, implying a constant macroscopic constitutive matrix;

5.1.1 Macroscale and constitutive relations

The macroscopic changes for a linear model are summarized in this section; all other derivations therein included remain equal to Section 3.2.

The axial strain of the couple-stress model (Eq. 3.2) becomes linear

$$\epsilon_x^l = \frac{\partial u}{\partial x} + z \frac{\partial \phi}{\partial x} = \epsilon^l + z\kappa \quad (5.1)$$

and, consequently, the virtual strain energy (Eq. 3.6) reduces to

$$\delta U^I = \int_0^l \left[N \frac{\partial \delta u}{\partial x} + M \frac{\partial \delta \phi}{\partial x} + Q \left(\delta \phi + \frac{\partial \delta w}{\partial x} \right) - P \frac{\partial^2 \delta w}{\partial x^2} \right] dx \quad (5.2)$$

The total shear force (Eq. 3.8) becomes

$$V = Q + \frac{\partial P}{\partial x} \quad (5.3)$$

The linear constitutive relations for a linear macroscopic model with linear microscale can be written as

$$\begin{Bmatrix} N \\ M \\ Q \\ P \end{Bmatrix} = \begin{bmatrix} A & C_1 & 0 & C_2 \\ C_1 & D & 0 & C_3 \\ 0 & 0 & D_Q & 0 \\ C_2 & C_3 & 0 & S \end{bmatrix} \begin{Bmatrix} \epsilon^I \\ \kappa \\ \gamma \\ \Theta \end{Bmatrix} \quad (5.4)$$

The constitutive matrix is symmetric in the linear case, that is, $C_{41} = C_{14}$ and $C_{52} = C_{25}$.

5.1.2 Linear finite element equations

In the linear case, adaptations are required for the element of Section 3.6. The generalized nodal shear force is based on Eq. 5.3 and terms containing $\left(\frac{dw}{dx}\right)$ are removed from the stiffness matrix. The definitions for quasi-static linear elastic and linear buckling analyses are provided as follows.

Linear axial and bending analyses

The elemental stiffness matrix in the linear case results into

$$\mathbf{K}_0^e = \int_{x_a}^{x_b} \mathbf{B}^T \mathbf{C} \mathbf{B} dx \quad (5.5)$$

as shown component-wise in Appendix A.4. The system of equations $\mathbf{F} = \mathbf{K}\mathbf{u}$ is solved for \mathbf{u} upon assembling the global force vector and stiffness matrix.

Eigenvalue (linear) buckling

Assume that the sandwich beam is subjected to a constant axial force N that induces transverse displacements. Following the basic steps in Ref. [31], the geometric stiffness matrix becomes [57]

$$\mathbf{K}_\sigma^e = \int_{x_a}^{x_b} N \mathbf{B}_\sigma^T \mathbf{B}_\sigma dx \quad (5.6)$$

The conventional eigenvalue buckling problem is then solved upon assembling the global matrices

$$(\mathbf{K}_0 - \lambda \mathbf{K}_\sigma) \mathbf{d}_\sigma = \mathbf{0} \quad (5.7)$$

where the eigenvalues λ correspond to the buckling load factors and the eigenvector \mathbf{d}_σ provides the buckling modes.

The linear buckling equations can be employed in the analysis of corrugated sandwich beams that display clear macroscopic failure.

5.2 Analogy with the thick-face sandwich theory

Consider the thick-face sandwich beam theory according to the conceptual framework of Allen [4] and Plantema [139]. In their works, the effect of thick faces is included by studying the shear deformation compatibility between core and faces. Take the case where horizontal sliding, denoted γ_0 in Allen [4] is zero. The global sandwich beam response is defined by a set of forces q_1 [4]

$$q_1 = -\frac{\partial Q_1}{\partial x} \quad (5.8a)$$

$$Q_1 = \frac{\partial M_1}{\partial x} \quad (5.8b)$$

$$M_1 = -D_g \frac{\partial^2 w_1}{\partial x^2} \quad (5.8c)$$

Near discontinuities, the faces must bend to a finite curvature for the face sheets and core to remain attached. Thus, they are locally subjected to a set of loads, shear forces and bending moments denoted q_2 , that is [4]

$$q_2 = -\frac{\partial Q_2}{\partial x} \quad (5.9a)$$

$$Q_2 = \frac{\partial M_2}{\partial x} \quad (5.9b)$$

$$M_2 = -D_f \frac{\partial^2 w_2}{\partial x^2} \quad (5.9c)$$

where $D_f \equiv S$ for an antiplane-core cell. The corresponding total quantities are given by

$$q_g = q_1 + q_2 \quad (5.10a)$$

$$Q_g = Q_1 + Q_2 \quad (5.10b)$$

$$M_g = M_1 + M_2 \quad (5.10c)$$

$$w_g = w_1 + w_2 \quad (5.10d)$$

Shear strain compatibility between face and core results in the following relations [4]

$$-Q_1 = D_g \frac{\partial^3 w_1}{\partial x^3} = -D_Q \frac{\partial w_2}{\partial x} + D_f \frac{\partial^3 w_1}{\partial x^3} \quad (5.11)$$

where D_Q has the same meaning as in the present work and $D_g = D + D_f$. The face sheet-related stiffnesses for an antiplane core are defined in Eq. 3.21. After some rearranging, the relations become

$$\frac{\partial^2 Q_1}{\partial x^2} - a^2 Q_1 = -a^2 Q_g, \quad a^2 = \frac{D_Q D_g}{D_f D} \quad (5.12)$$

Recall the couple stress beam equilibrium equations, Eq. 3.25. Following the modifications towards a linear model (Section 5.1.1), axial and bending responses are decoupled; here only the latter is of interest.

Substituting the relations in Eq. 5.4 into the shear force equilibrium (Eq. 3.25b, neglecting the von Kármán term), the relation between shear angle and cross-sectional rotation angle becomes

$$\gamma = \frac{D}{D_Q} \frac{\partial^2 \phi}{\partial x^2} \quad (5.13)$$

Writing the equilibrium equation related to the shear force derivative (Eq. 3.25b) in terms of displacements, and substituting the shear angle definition of Eq. 3.2b, also reckoning that $S \equiv D_f$ for an antiplane core, the following relation is obtained

$$-q = D_g \frac{\partial^3 \phi}{\partial x^3} - D_f \frac{\partial^3 \gamma_{xz}}{\partial x^3} \quad (5.14)$$

Integrating Eq. 5.14 and recalling that $\int q dx = -V$

$$V = D_g \frac{\partial^2 \phi}{\partial x^2} + C - D_f \frac{\partial^2 \gamma}{\partial x^2} = \bar{Q} + Q_\gamma \quad (5.15)$$

where the constant of integration obtained is included in the global shear term defined as \bar{Q} . Substituting \bar{Q} into Eq. 5.13 and differentiating twice

$$\frac{\partial^2 \gamma}{\partial x^2} = \frac{D}{D_Q D_g} \frac{\partial^2 \bar{Q}}{\partial x^2} \quad (5.16)$$

Isolating $\partial^2 \gamma / \partial x^2$ in Eq. 5.15 and substituting in Eq. 5.16, the following differential equation is obtained

$$\frac{D_f D_0}{D_g D_Q} \frac{\partial^2 \bar{Q}}{\partial x^2} = -V + \bar{Q} \rightarrow \frac{\partial^2 \bar{Q}}{\partial x^2} - a^2 \bar{Q} = -a^2 V, \quad a^2 = \frac{D_Q D_g}{D_f D_0} \quad (5.17)$$

Eq. 5.17 is equal to the governing equation of the thick-face sandwich theory, Eq. 5.12, acknowledging that $\bar{Q} = Q_1$ and $V = Q_a$. Therefore, the two theories are shown to be equivalent in bending for the basic assumptions of Ref. [4]. The equivalence is lost when couplings are included in the constitutive matrix (as in Eq. 5.4) or when geometric nonlinearities are considered.

5.3 Numerical validations

The two-scale model is demonstrated through linear analyses of selected elastic corrugated sandwich beams. The beams represent wide panels along the y -axis, whose response is two-dimensional; results are shown for a unit-width beam, $b = 1.0$ m. Plane strain is then assumed for the panels, with elastic modulus set to $E = E_s/(1 - \nu_s^2)$. To simplify geometric comparisons, the material properties $E_s = 206$ GPa and $\nu_s = 0.3$ are taken for face sheets and core struts in all cases. Considering the linear microscopic behavior, stiffnesses are computed using the relations presented in Chapter 4 for $\bar{E}_j = \bar{E}_k = E$.

The examples are validated using finite element models that represent the three-dimensional geometry (denoted 3-D FE), which are constructed with four-node reduced integration shell elements (Abaqus S4R) as illustrated in Figure 5.1. Boundary idealizations are consistent with the kinematics of the macroscopic homogenized beam.

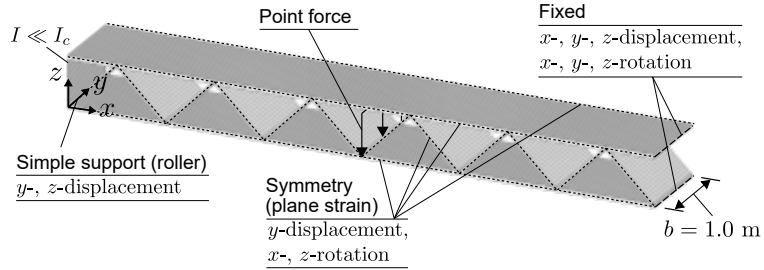


Figure 5.1. Examples of boundary conditions utilized in the 3-D FE validation models. Reproduced from [57].

Percent deflection error of a given homogenized beam model m is defined with respect to an equivalent three-dimensional finite element reference model

$$\varepsilon(\%) = 100 \left(\frac{w_m - w_{(3-D)}}{w_{(3-D)}} \right) \quad (5.18)$$

Percent buckling load error is defined analogously (that is, substituting w

by the constant axial force N in Eq. 5.18).

Relative core densities referred in this Chapter are taken as

$$\text{Web-core: } \rho_c = \frac{t_c}{s} \quad (5.19a)$$

$$\text{Triangular core: } \rho_c = \frac{t_c}{s} \left[\frac{2(p - t_f)}{d - t_f} \right] \quad (5.19b)$$

$$\text{X-core: } \rho_c = \frac{t_c}{s} \left[\frac{4(p - t_f)}{d - t_f} \right] \quad (5.19c)$$

$$\text{Y-core: } \rho_c = \frac{t_c}{s} \left[\frac{(4p + d - 3t_f)}{2(d - t_f)} \right] \quad (5.19d)$$

which are based on the cell geometric relations defined in Chapter 4.

5.3.1 Linear bending deflection analyses

Validation table

The linear bending response of sandwich beams composed of truss-core cells of length $s = 4a + 2c = 0.2$ m (Figure 5.2a) and corrugation angle defined as $\alpha = \arctan(d/c)$ is investigated in a parametric fashion. The boundary conditions utilized in the validation models are sketched in Figure 5.3. Deflections obtained with the present model are compared to the validation models in Table 5.1 for a 2.0 m beam with $d/t_c = 20$ under three-point bending ($F = 10$ kN). The stiffnesses utilized in each cases are provided. The results are also validated against the thick-face sandwich theory solution (as defined in Ref. [4]).

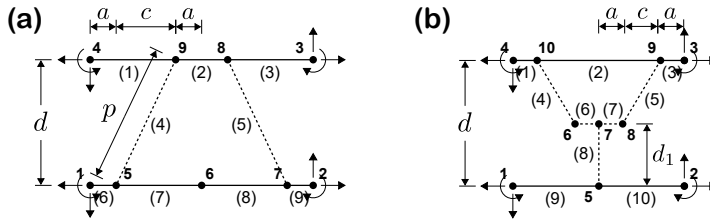


Figure 5.2. Frame unit cell models of (a) a generic truss-core (b) Y-core sandwich beam.

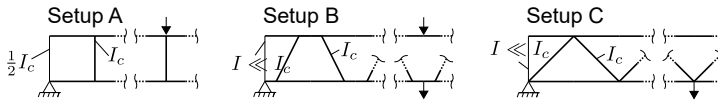


Figure 5.3. Schematic view on validation model (3-D FE) details as utilized in the deflection analyses of Section 5.3.

In the homogenized model, the following boundary conditions are valid for a symmetric half-beam of length $L = L_0/2$

$$\begin{aligned} x = 0: \quad w(0) = N(0) = M(0) = P(0) &= 0 \\ x = L/2: \quad u(L) = \phi(L) = \theta(L) &= 0, \quad V(L) = F/2 = 5kN \end{aligned} \quad (5.20)$$

Accurate predictions are obtained in all cases. The present model predicts strictly the same deflections as the thick-face sandwich theory for the antiplane setup A. Minor differences are seen in setups B and C due to interactions between face sheets and inclined core struts, which are neglected in the thick-face sandwich theory but included in the present constitutive equations. The present model is slightly stiffer than the model in Ref. [4].

Deflection analyses

Sandwich beams composed of four unit cells with geometric relations defined in Section 4 are analyzed next in terms of deflection distributions. The cells have dimensions $s = d = 0.1$ m, $t_f = d/20$ and core relatively densities $\rho_c = 0.05$ or $\rho_c = 0.15$. Twelve cell repetitions compose the beams ($L = 12s$), which are subjected to three-point bending. Exploiting the beam symmetry, the same general boundary conditions as in Eq. 5.20 are utilized for $F = -100$ kN.

The deflection lines obtained are shown in Figure 5.4. For the transversely asymmetric cores, values obtained from three-dimensional finite element models are shown for top and bottom face sheets. Overall, the present model is able to predict the average deflection accurately against the validation models for all combinations of stiff, flexible, low- and high-density cores. Changes in core density lead to limited response changes in the shear-stiff X-core and triangular core cells. Web-core and Y-core unit cells have their bending response highly influenced by ρ_c , as their transverse shear moduli are function of t_c^3 . Local fluctuations seen in the 3D-FE lines could be retrieved from the homogenized model by localization of the shear deformation.

5.3.2 Linear bending stress analyses

The following examples utilize the equations of Section 3.5 to predict face sheet and core stress distributions. Different unit cell arrangements and various loading conditions are studied.

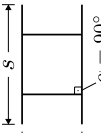
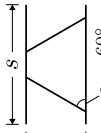
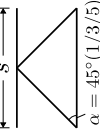
Corrugated cells			Stiffness parameters						Max. deflection, w_{max} [mm]			
Setup	Core	t_f/t_c	s/d	A [MN/m]	$C_2 = -C_1$ [kN]	D [kNm]	S [kNm]	C_3 [kNm]	D_Q [kN/m]	3-D FE	Sandwich theory [10]	Present, (\bar{E})
A.1		2	2	4527.5	0	11318.7	37.7	0	2661.65	1.804	1.791	1.791 (-0.7%)
A.2		4	4	2263.7	0	1414.84	4.72	0	628.118	8.400	8.398	8.398 (0.0%)
A.3		1	2	2263.7	0	5659.34	4.72	0	1884.88	2.843	2.810	2.810 (-1.1%)
A.4			4	1131.9	0	707.418	0.590	0	353.267	16.053	15.907	15.907 (-0.9%)
A.5		0.5	2	1131.9	0	2829.67	0.59	0	565.651	9.337	9.139	9.139 (-2.1%)
A.6			4	565.93	0	353.709	0.074	0	78.5583	67.826	66.383	66.383 (-2.1%)
B.1		2	2	4528.2	63.8	11324.2	43.9	-5.5	37311.7	0.277	0.276	0.275 (-0.8%)
B.2		4	4	2263.9	13.58	1416.01	5.93	-1.18	1318.12	4.678	4.717	4.689 (0.2%)
B.3		1	2	2264.2	37.94	5662.62	8.53	-3.28	11455.5	0.714	0.721	0.718 (0.6%)
B.4			4	1131.9	5.213	707.870	1.066	-0.453	543.032	11.089	11.244	11.138 (0.4%)
B.5		0.5	2	1132.0	8.939	2830.44	1.57	-0.77	3462.50	1.970	2.013	2.001 (1.6%)
B.6			4	565.94	0.879	353.785	0.156	-0.079	124.647	42.753	43.833	43.389 (1.5%)
C.1		2	2	4529.5	99.9	11323.7	44.4	-5.0	340061	0.160	0.161	0.161 (0.8%)
C.2		4	4	2265.0	31.57	1415.62	5.77	-0.79	74561.4	1.229	1.240	1.240 (0.9%)
C.3		1	2	2265.7	99.92	5664.34	11.39	-5.00	295648	0.308	0.311	0.311 (0.9%)
C.4			4	1133.1	31.574	708.207	1.644	-0.789	59011.9	2.414	2.438	2.437 (1.0%)
C.5		0.5	2	1133.9	99.92	2834.67	7.26	-5.00	234418	0.604	0.610	0.610 (1.0%)
C.6			4	567.20	31.574	354.498	1.128	-0.789	41642.9	4.780	4.831	4.827 (1.0%)

Table 5.1. Cell setups, dimensions, corresponding stiffness parameters and maximum deflections predicted with present and validation models for $L = 2.0$ m beams subjected to three-point bending ($F = 10$ kN).

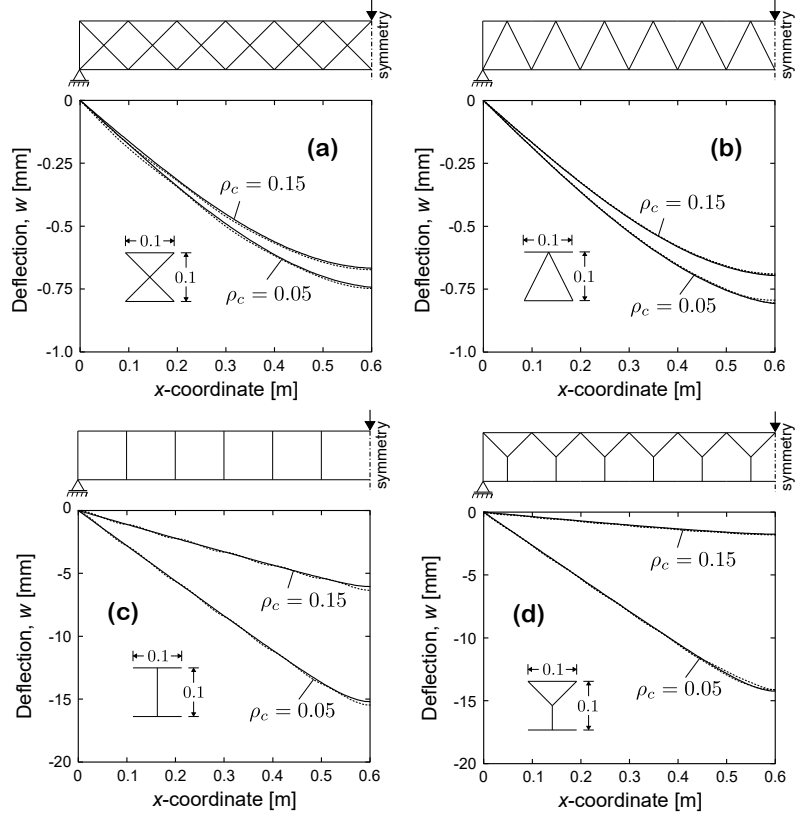


Figure 5.4. Three-point linear bending deflections with the present (linear two-scale) model and validation (3-D FE) (a) X-core (b) triangular core (c) web-core (d) Y-core.

Cantilevered X-core beam under end vertical force

A X-core sandwich beam of length $L = 1.2$ m is fixed at one end while free and subjected to a vertical concentrated force $F = -10$ kN at the opposite end. The unit cell dimensions are $d = s = 0.12$ m, and $t_f = t_c = 0.006$ m, see Figure 4.2c for reference. The homogenized beam boundary conditions are

$$\begin{aligned} x = 0: \quad & u(0) = w(0) = \phi(0) = \theta(0) = 0 \\ x = L: \quad & N(L) = M(L) = P(L) = 0, \quad V(L) = F \end{aligned} \quad (5.21)$$

The maximum deflection obtained with the validation model is $w(L_0/2) = -5.982 \cdot 10^{-4}$ m, whereas the homogenized couple-stress model predicts $w(L_0/2) = -5.975 \cdot 10^{-4}$ m ($\epsilon \approx 0.1\%$).

The stress distribution within cell $n = 1..10$ at $i = t, b$ face sheet is pre-

dicted based on the homogenized macroscopic solution as

$$\hat{\sigma}_i = \frac{E}{s} \int_{(n-1)s}^{ns} \left\{ \epsilon_0 + \frac{d^2}{d_i} \kappa_0 + \frac{12z_i}{t_f^3} \left[\Theta + s(n-1) \left(\frac{k_Q D_Q}{E} \gamma + k_P S \frac{\partial \Theta}{\partial x} \right) \right] \right\} dx \quad (5.22)$$

where the shear distribution factor is $k_Q = 7.32 \cdot 10^{-4}$. For simplicity, $k_P = k_Q$ is assumed.

Figure 5.5 shows the stress distributions at the top surface of the top face sheet (Figure 5.5a) and bottom surface of bottom face sheet (Figure 5.5b) as predicted with the homogenized and validation models. The present model is shown able to predict the stress distributions accurately. Deviations are observed within the unit cell at the fixed end, related to the simplified local cell shear description of the macroscopic model. As the unit cell has a stretch-related transverse shear-carrying mechanism, axial normal stresses are dominant. Bending stresses are observed mainly near the fixed end and described by the cell bending parameter. Macroscopic shear-induced bending stresses related to the Timoshenko shear description are small over the entire domain.

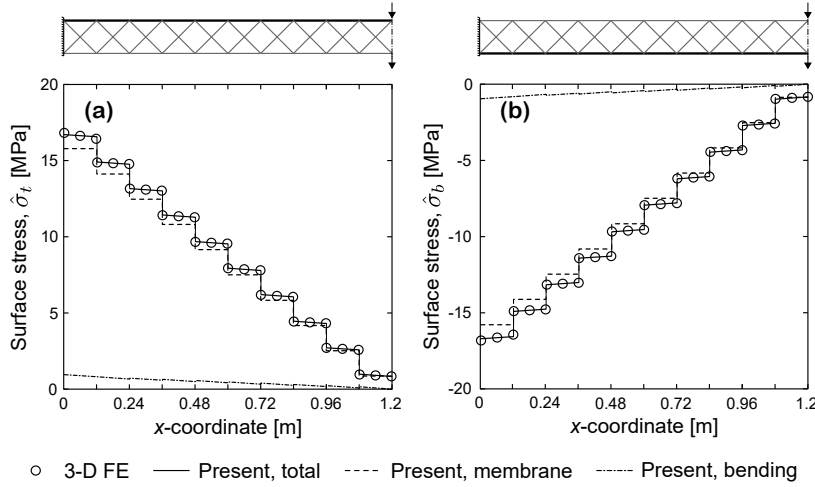


Figure 5.5. Stress distributions of a X-core sandwich cantilever beam as predicted with present and (extrapolated) 3-D FE validation model (a) top surface of the top face (b) bottom surface of the bottom face.

Fixed-fixed triangular core beam under mid-span force

A triangular core sandwich beam of length $L = 2.0$ m is fixed at both ends and subjected to a vertical point force $F = -50$ kN at mid-span. The following cell dimensions are taken: $s = 0.125$ m, $d = 0.08$ m, $t_f = 0.004$ m and $t_c = 0.002$ m. The boundary conditions are utilized for the homogenized

model, where $L = L_0/2$ due to symmetry

$$\begin{aligned} x = 0: \quad & u(0) = w(0) = \phi(0) = \theta(0) = 0 \\ x = L: \quad & u(L) = \phi(L) = \theta(L) = 0, \quad V(L) = F/2 \end{aligned} \quad (5.23)$$

The maximum deflection obtained with the validation model is $w(L_0/2) = -8.680 \cdot 10^{-5}$ m, whereas the homogenized couple-stress model predicts $w(L_0/2) = -8.779 \cdot 10^{-5}$ m ($\epsilon \approx 1.1\%$).

The bottom face sheet stress distribution within cell $n = 1.8$ is predicted based on the homogenized macroscopic solution according to Eq. 5.22, whereas for the top face sheet a phase shift of $s/2$ in the integration interval is introduced. The parameter $k_Q = 4.43 \cdot 10^{-4}$ is computed and $k_P = k_Q$ is taken as a simplification. Figure 5.6 shows the face sheet stress distributions predicted by the present and validation models.

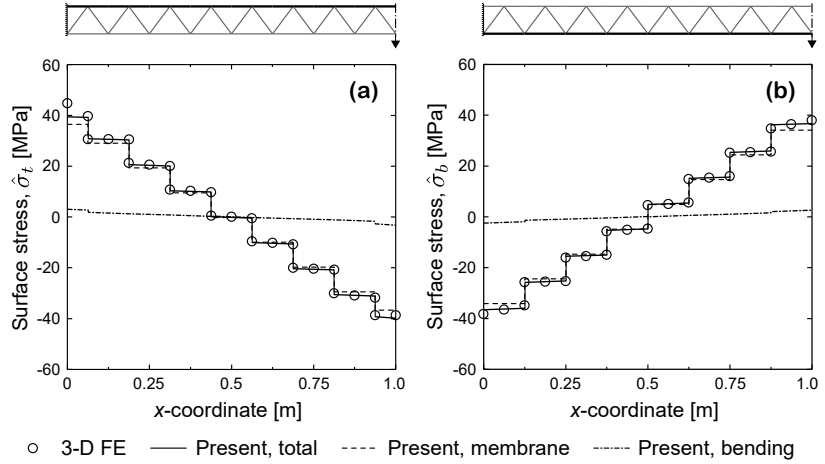


Figure 5.6. Stress distributions of a triangular core sandwich cantilever beam as predicted with present and 3-D FE validation model (extrapolated) (a) top surface of the top face sheet (b) bottom surface of the bottom face sheet.

Good agreement is generally observed. The shear-induced bending moment at the segment nearest fixed end segments somewhat deviates from the validation model when $k_P = k_Q$ is assumed. A more accurate description would require a macroscopic model with additional shear parameters, or at least an auxiliary unit cell model to estimate the shear distribution approximation. As in the X-core beam example, axial normal stresses are dominant; away from the boundaries, average local cell bending and periodic shear-induced bending components are negligible.

Pinned-roller web-core beam under mid-span force

A web-core sandwich beam composed of ten unit cells, with general dimensions $d = 0.042$ m, $t_f = 0.003$ m, $t_c = 0.004$ m, $s = 0.12$ m, to a total length $L_0 = 1.2$ m, is assessed under three-point bending. The face sheets and webs are semi-rigidly connected; four rigidity (per unit width) levels, $k_\theta = 10$ kN, $k_\theta = 50$ kN, $k_\theta = 100$ kN and $k_\theta = 10000$ kN are considered. The load F applied at mid-span is scaled to $w(L_0/2) = -0.01$ m (3-D FE model) to facilitate the response comparisons. The boundary conditions (symmetry, $L = L_0/2$) are the same as presented in Eq. 5.20.

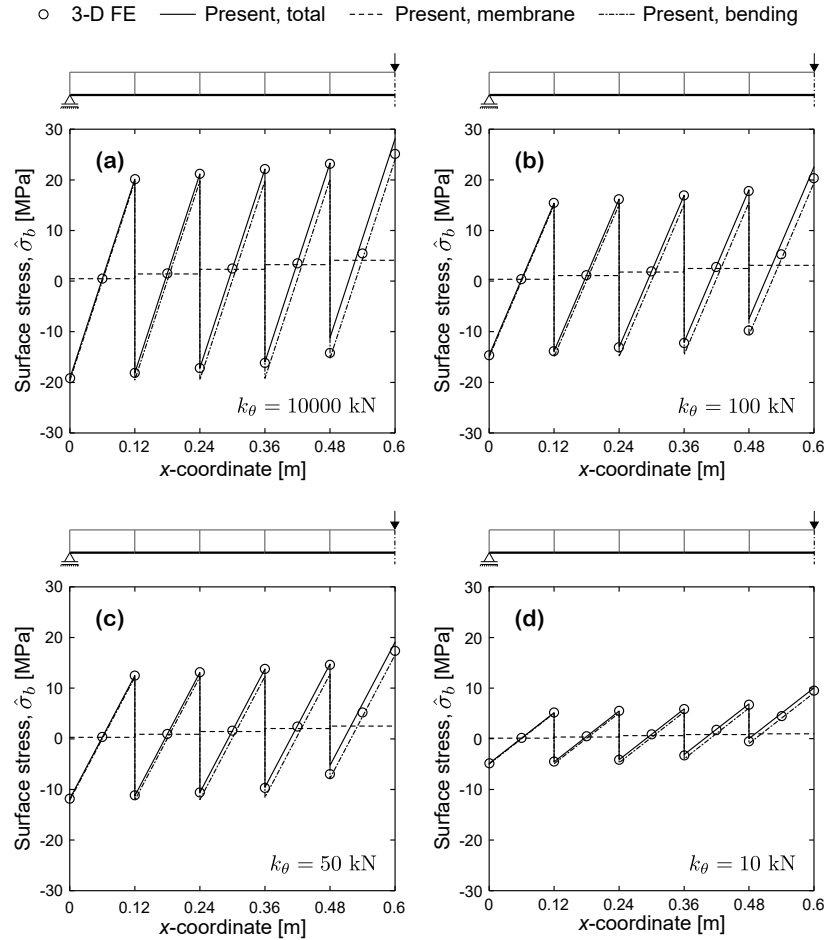


Figure 5.7. Bottom surface stress distribution at the bottom face sheet of web-core sandwich beams in three-point bending, present and 3-D FE models (extrapolated). Face sheet-web joint rotational stiffness (a) $k_\theta = 10000$ kN, (b) $k_\theta = 100$ kN, (c) $k_\theta = 50$ kN, (d) $k_\theta = 10$ kN.

Stresses are evaluated by employing Eq. 5.22 for $i = b$ and $z_i = -t_f/2$. The shear distribution factor is $k_Q = k_P = 1/2$ in all cases. Figure 5.7 show bottom surface stress distributions for the different k_θ (bottom face sheet). The vertical reaction forces obtained are also presented. Good agreement is observed between the models in all conditions. The beam becomes increasingly shear-flexible as the connection stiffness is decreased. Shear-induced bending stresses (visualized as the zig-zag pattern) are reduced as $k_\theta \rightarrow 0$; the sandwich effect is progressively lost and cell local bending becomes dominant.

Figure 5.8 shows the stress distribution over the core height obtained with present and validation models. The sandwich effect is shown to reduce as the joint rotational stiffness is lost; as the connection approaches a pinned condition, $k_\theta \rightarrow 0$, the assembly behaves as two separate beams bending with the rigidity of each face sheet, whereas the stresses at the webs tend to zero.

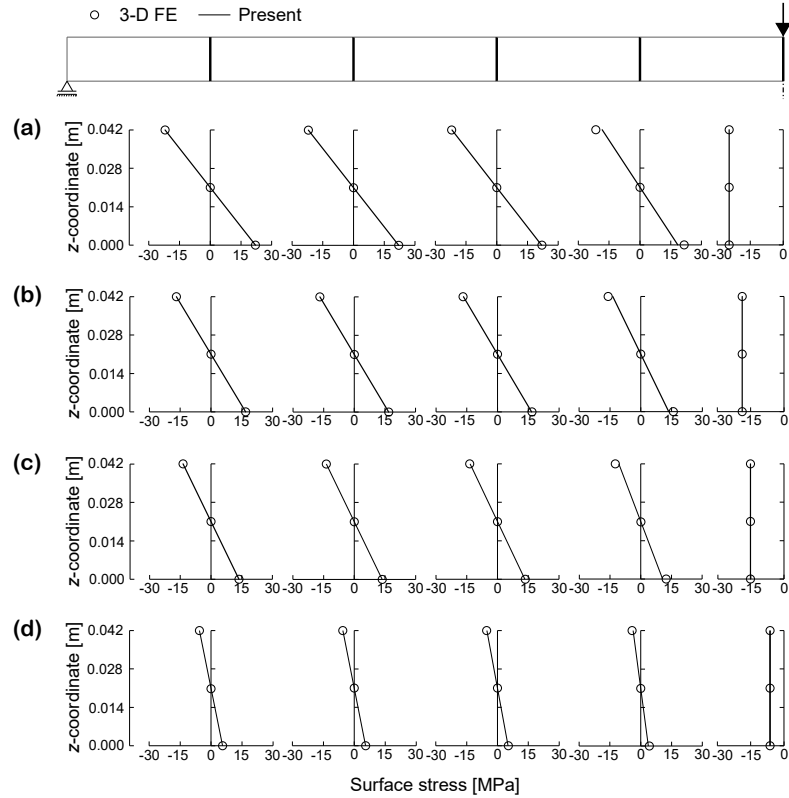


Figure 5.8. Web stress distribution of web-core sandwich beams in three-point bending, present and (extrapolated) 3-D FE models. Face sheet-web joint rotational stiffness (a) $k_\theta = 10000$ kN, (b) $k_\theta = 100$ kN, (c) $k_\theta = 50$ kN, (d) $k_\theta = 10$ kN.

5.3.3 Linear buckling analyses

The linearized model can predict the critical buckling load of sandwich beams whose failure mechanism is exclusively due to elastic global buckling, as demonstrated next through one example. In structures where local buckling is relevant, the multiscale approach is required for maintained accuracy, as discussed in the following chapter.

Axially compressed pinned-pinned and fixed-free Y-core beams

In this section, two Y-core setups are analyzed as presented in Ref. [57] by the Author. In ships, Y-core sandwich panels are typically composed of relatively few large, flexible cells and thus prone to exhibit size effects.

Consider Y-core unit cells with dimensions $a = 0.002$ m, $d_1 = 0.013$ m, $d = 0.022$ m, $s = 0.026$ m, $t_f = 0.001$ m and $t_c = 0.0003$ m (see Figure 5.2b), which are similar to the dimensions adopted in Ref. [156]. The boundary conditions considered are

Fixed-free (cantilever):

$$\begin{aligned} x = 0: \quad & V(0) = M(0) = P(0) = 0, \quad N(0) = F \\ x = L: \quad & u(L) = w(L) = \phi(L) = \theta(L) = 0 \end{aligned} \quad (5.24a)$$

Simply-supported:

$$\begin{aligned} x = 0: \quad & w(0) = M(0) = P(0) = 0, \quad N(0) = F \\ x = L: \quad & u(L) = w(L) = \phi(L) = \theta(L) = 0 \end{aligned} \quad (5.24b)$$

Figure 5.9 shows percent error comparisons between present and the classical antiplane-core Timoshenko model as function of the relative unit cell size s/L . The critical buckling loads predicted by the corresponding validation models are also shown for reference; as expected, the linear buckling capacity is larger for shorter beams.

Generally, the analyses show that the classical Timoshenko beam results progressively less accurate as the relative unit cell size is increased, underpredicting the buckling capacity. The error is larger in the simply-supported case than in the end-loaded cantilever due to the transverse concentrate load effect. The present model in its linear format is accurate for the entire unit cell size range and either boundary conditions as global buckling dominates the response.

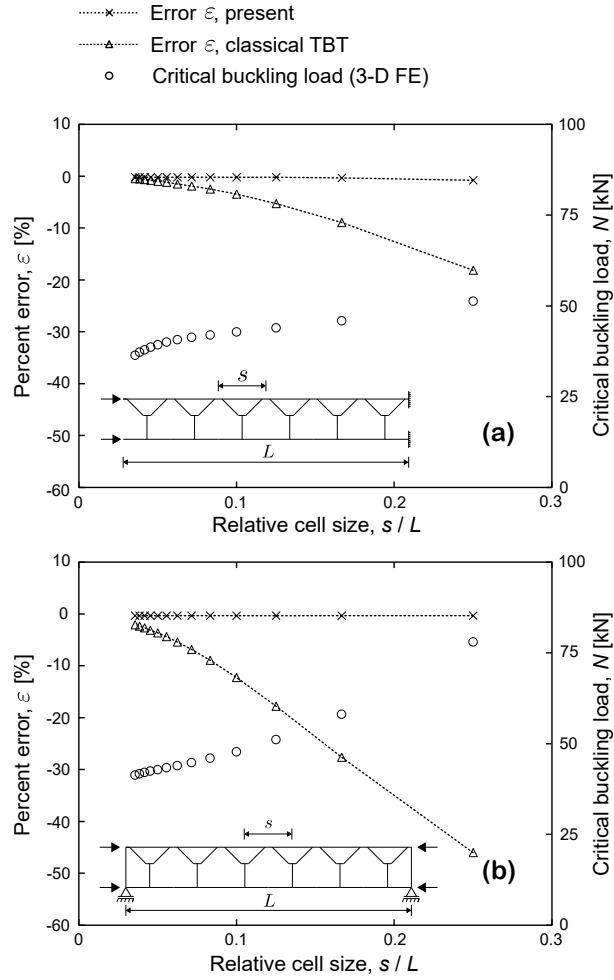


Figure 5.9. Linear buckling analysis of Y-core sandwich beams under axial compression (a) end-loaded cantilever (b) end-loaded simply-supported beam. Percent error of present and classical Timoshenko (antiplane) model, and critical buckling load (3-D FE).

6. Multiscale analyses

This chapter validates the multiscale approach proposed in Chapter 3. First, assumptions needed for the validations are recalled and discussed. The nonlinear bending response of corrugated sandwich beams is predicted in terms of displacements and stresses. Their progressive failure is discussed along the governing macroscopic parameters in the present approach. Elastic buckling capacities are estimated and post-buckling paths traced for setups with different characteristics. Results are validated against three-dimensional finite element models, and compared with analytical predictions and the classical nonlinear Timoshenko model with antiplane stiffnesses.

6.1 General assumptions

The analyses hold the same general assumptions presented in Section 3.1 and Section 5.3. As in the previous linear analyses, the beams represent wide panels along the y -axis, with elastic modulus $E = E_s/(1 - \nu_s^2)$, $E_s = 206$ GPa and $\nu_s = 0.3$; results are shown per unit width. The material is assumed to remain elastic in all cases. The validation models (3-D FE) are constructed with Abaqus S4R shell elements (see Figure 5.1), and its geometrically nonlinear response is obtained using the Riks method of the Abaqus standard solver [154].

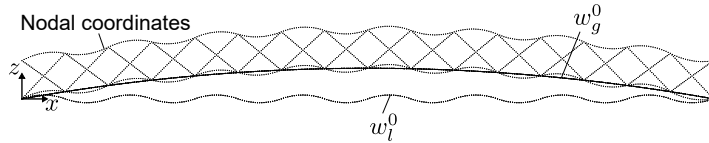


Figure 6.1. Initial geometric imperfections assigned to a 3-D model as superposition of microscopic (faces only) and macroscopic initial deflections (magnified).

In the general case, initial global and local sinusoidal imperfections are assumed to be present. Global imperfections are assigned by adjusting the nodal coordinates in three-dimensional finite-element and homogenized models. In the latter, the transformation matrix $\hat{\mathbf{T}}$ is utilized to rotate the elements (Appendix A). In the validation models, local imperfections are assigned by adjusting the face sheet nodal coordinates (Figure 6.1), whereas in the multiscale approach they are embedded in the macroscopic constitutive relations via nonlinear stiffnesses.

6.2 Nonlinear bending studies

Local face sheet buckling substantially affects the global bending response of beams composed of corrugated cells with a stretch-dominated transverse shear mechanism. The suitability of the present approach to predict their progressive failure and stress distributions under moderate quasi-static transverse loads is investigated in selected cases.

6.2.1 X-core beam with variable core relative flexibility

A X-core sandwich beam of length $L_0 = 16s = 0.8$ m and cell dimensions $s = d = 50t_f$ and $t_f/2 \leq t_c \leq 2t_f$ is studied in bending. The core rotational stiffness $k_c = 4EI_c/p$ depends on the t_f/t_c relation; three combinations are considered as demonstrated in Figure 6.3.

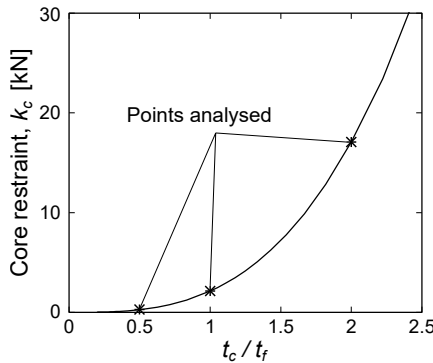


Figure 6.2. Core rotational restraints obtained for X-core unit cells with different t_f/t_c ratios.

Globally, the beam is initially straight, whereas the face sheets have a local sinusoidal imperfection of amplitude $\alpha_l = t_f/10$. The nonlinear stiffness relations obtained from the local buckling microscopic relations are shown in Figure 6.3.

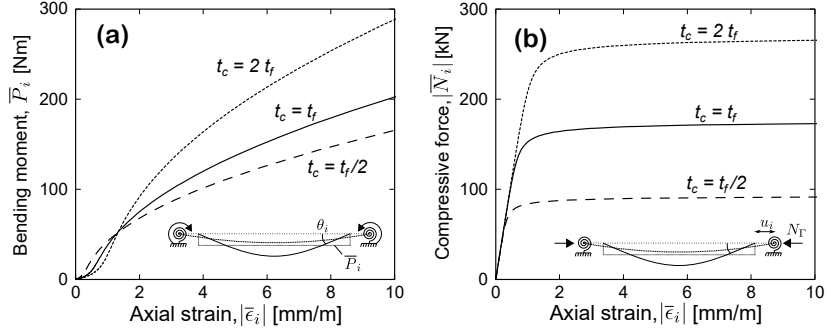


Figure 6.3. Microscopic relations that define the nonlinear face response under compression (a) bending moment to axial strain (b) axial force to axial strain.

Two boundary conditions are studied, which in the homogenized model are given by (symmetry, $L = L_0/2$)

Pinned-symmetry:

$$x = 0: \quad u(0) = w(0) = M(0) = P(0) = 0$$

$$x = L/2: \quad u(L) = \theta(L) = \phi(L) = 0, \quad V(L) = F/2 \quad (6.1a)$$

Cantilever (pinned edge):

$$x = 0: \quad u(0) = w(0) = P(0) = \phi(0) = 0,$$

$$x = L: \quad N(L) = M(L) = P(L) = 0, \quad V(L) = F \quad (6.1b)$$

In the cantilever case, the boundary sectional rotation ϕ is constrained but the slope θ is non-zero. The boundary conditions represent discrete pinned top and bottom face sheets in the equivalent discrete structure. The equilibrium equations are solved using the Newton-Raphson solver (Section 3.6.2) with convergence tolerance set to $\varepsilon_{tol} = 10^{-5}$.

Figure 6.4 and Figure 6.5 show the *Load vs. maximum deflection* relations obtained with the present approach and equivalent three-dimensional finite element models. Good agreement between the predictions is observed. The pinned-pinned beam conserves considerable post-buckling stiffness, which is activated by stretching the horizontally axially restrained faces. Conversely, sudden collapse is observed in the cantilevered beam, and limited post-buckling stiffness remains. The local buckling initiation load is substantially influenced by the relative core thickness; the rotational restraint k_c , which has great influence in the face sheet response, is a function of the core bending stiffness (thus, of t_c^3).

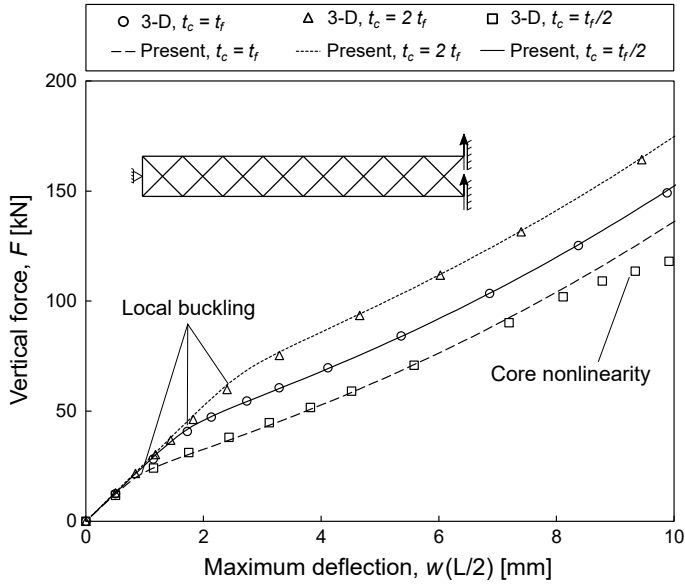


Figure 6.4. Load vs. maximum deflection relations for mid-span (symmetry line) loaded pinned-symmetry X-core sandwich beam with different t_f/t_c .

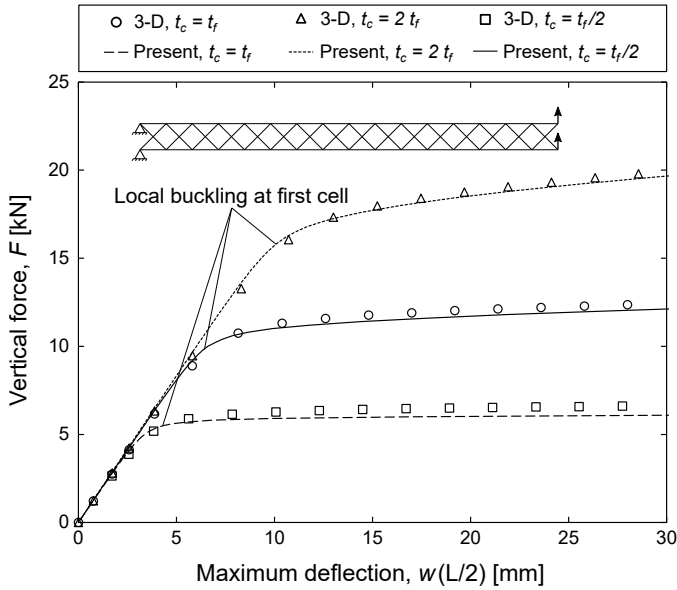


Figure 6.5. Load vs. maximum deflection relations for end-loaded cantilever (doubly pinned) X-core sandwich beam with different t_f/t_c ratios.

6.2.2 Progressive bending failure and stress analysis

The progressive nonlinear response of a triangular core sandwich beam with dimensions $L_0 = 12s = 24d = 2.4$ m and $t_f = t_c = d/50$ is considered. The global beam is initially straight, whereas the face sheets have sinusoidal imperfections of amplitude $\alpha_l = t_f/5$. Following the analogy presented in Section 4.2, the core rotational restraint is taken as $k_c = 4EI_c/p = 4269$ kN. Force-to-strain relations describing the face sheet geometrically nonlinear response are presented in Figure 6.6.

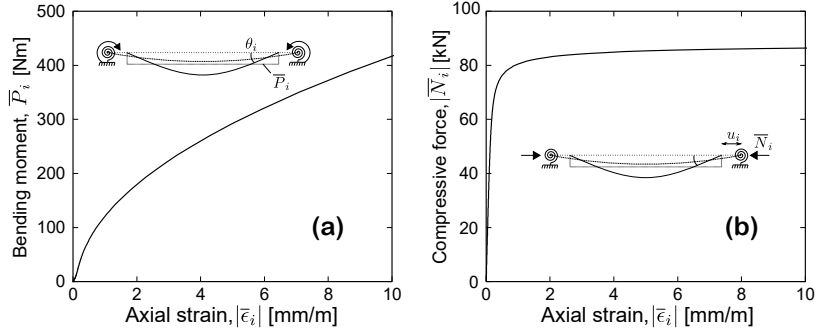


Figure 6.6. Microscopic relations that define the nonlinear face response under compression (a) bending moment to axial strain (b) axial force to axial strain.

The macroscopic beam boundary conditions, considering the mid-length symmetry at $x = L/2$, are given by

$$\begin{aligned} x = 0: \quad & u(0) = w(0) = P(0) = \phi(0) = 0 \\ x = L/2: \quad & u(L) = \theta(L) = \phi(L) = 0, \quad V(L) = -F/2 \end{aligned} \quad (6.2)$$

The boundary sectional rotation is ϕ constrained but the slope θ is non-zero to represent pinned top and bottom face sheets in the equivalent discrete structure.

Figure 6.7 shows the nonlinear *force vs. displacement* relations obtained. The predictions result accurate for the entire analysis. The percent error in maximum displacement is approximately 4-5% around Point (A), progressively reducing as the failure progresses. The maximum displacement percent error around Point (C) is less than 1%. In terms of stiffness response, three major zones are distinguishable: an approximately geometrically linear range, onset and development of local buckles at the highest-stressed regions, and progressive stretch-stiffening due to the horizontal supports. Points (A)-(C) are, respectively, representative of each zone.

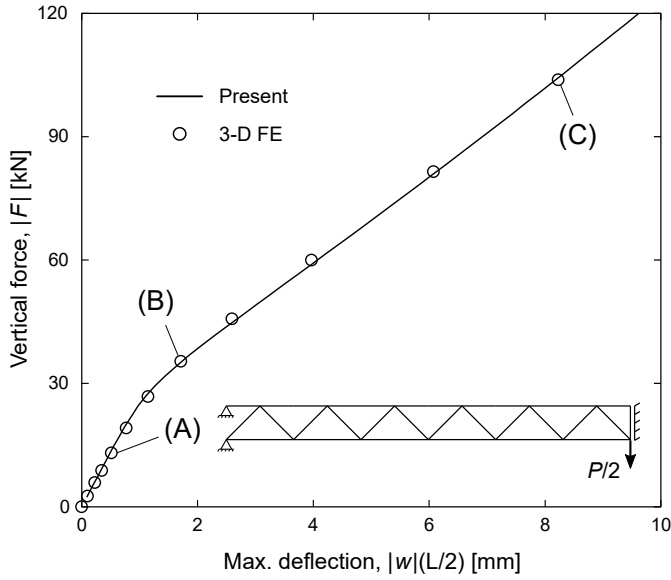


Figure 6.7. Load vs. maximum deflection relations and points under inspection, (doubly) pinned-symmetry sandwich beam under vertical force at the symmetry line.

The multiscale approach relies on discretely modifying the macroscopic stiffnesses as described in Section 3.4. Figure 6.8 shows the homogenized stiffnesses obtained over the beam length at Point (A), Point (B) and Point (C). Progressive axial and axial-bending stiffness reductions are highly localized, affecting the first segment near the (doubly) pinned-end and symmetry line. The coupling C_1 describes the progressive asymmetry in their axial response. The second internal segment at either end displays a stiffness recovery due to the observed straightening effect.

The stress distributions over top and bottom face sheets at Point (A), Point (B) and Point (C) are shown in Figure 6.9 and Figure 6.10, respectively. The present homogenized model is shown to predict stress levels satisfactorily when geometric nonlinearities are moderate. In the initial, approximately linear zone, stress predictions are accurate. Past the onset of local buckling, the predictions are somewhat less precise, yet a good indicative level can be achieved. Error can be mainly attributed to:

- Face sheet-core nonlinear interactions, which are not captured by the homogenized model.
- Interactions between neighboring cells, which can be described in only a very limited manner.

At Point (A) (Figure 6.9a and Figure 6.10a), secondary bending-induced stresses are small yet widespread due to the initial imperfection effect. At Point (B) (Figure 6.9b and Figure 6.10b), local buckles develop near the beam ends and the local buckling-related secondary bending stress becomes dominant over the other components. At Point (C) (Figure 6.9c and Figure 6.10c), the local buckles at the boundary segments further develop, while the nonlinear membrane stiffening effect straightens the beam elsewhere.

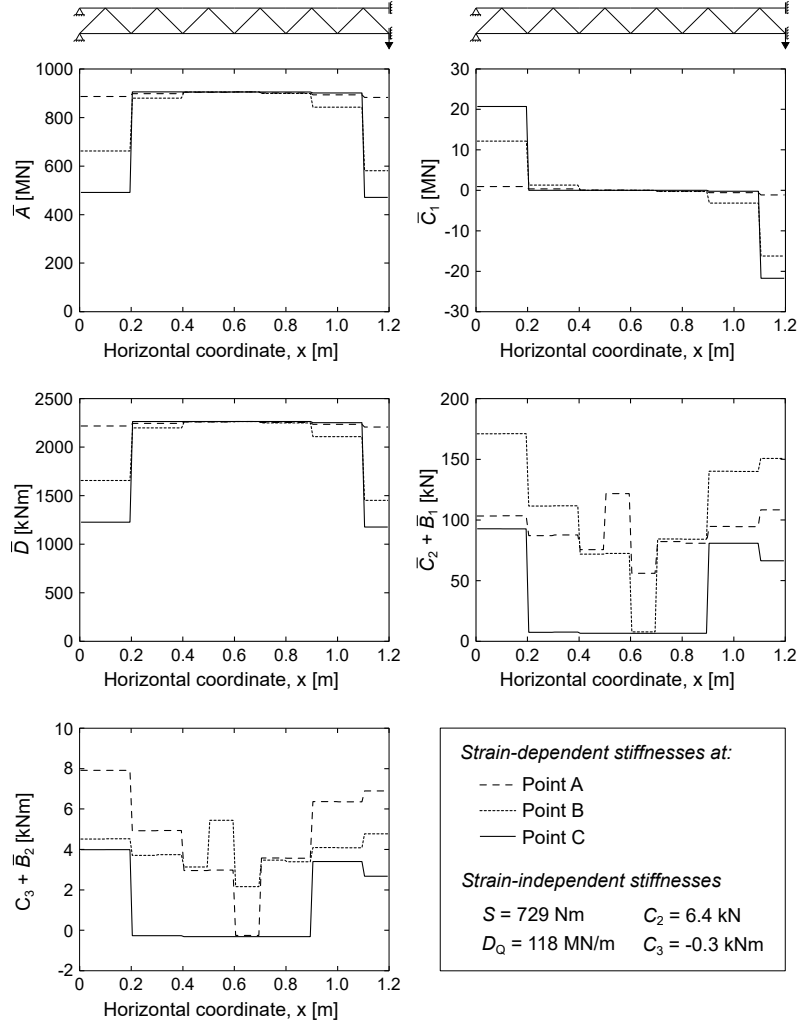


Figure 6.8. Strain-dependent stiffnesses at Points (A), (B) and (C), and strain-independent stiffnesses.

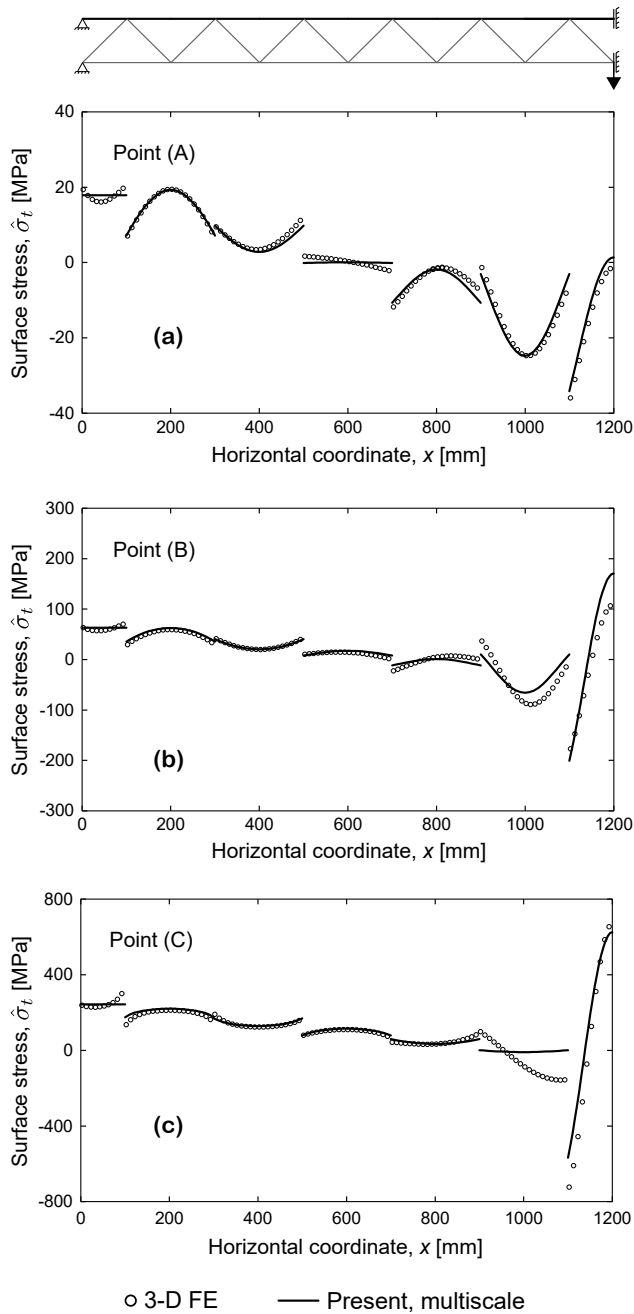


Figure 6.9. Top surface stress distribution at the top face sheet, (doubly) pinned-symmetry sandwich beam under vertical force at the symmetry line (a) Point (A) (b) Point (B) (c) Point (C).

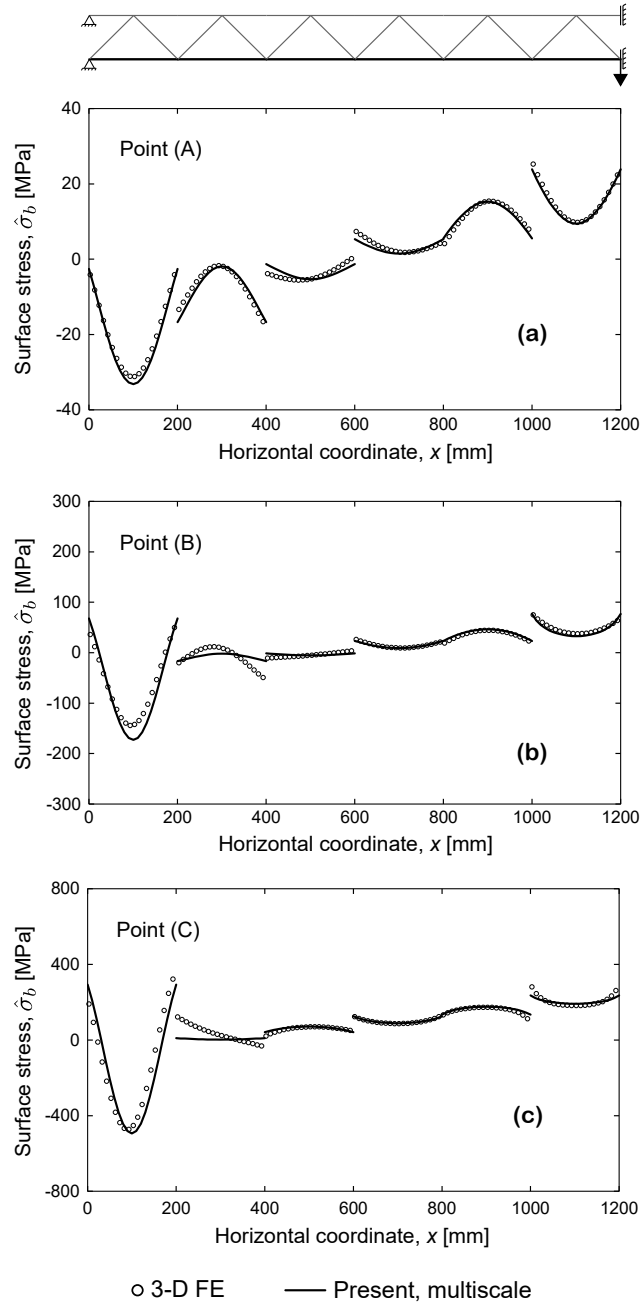


Figure 6.10. Bottom surface stress distribution at the bottom face sheet, (doubly) pinned-symmetry sandwich beam under vertical force at the symmetry line (a) Point (A) (b) Point (B) (c) Point (C).

6.3 Nonlinear buckling studies

Local nonlinearities have great impact in progressive buckling response of corrugated sandwich beams with stretch-dominated cores. Meanwhile, as demonstrated in Section 5.3.3, unit cell stiffness effects may be significant in shear-flexible beams. The suitability of the present approach to predict the buckling response of beams with different structural ratios is investigated next. Comparisons with 3-D finite element validation models, classical Timoshenko antiplane model, and analytical equations are provided.

6.3.1 Post-buckling analysis of a X-core and size effects

X-core sandwich beam structures with unit cell dimensions $s = d = 0.1$ m to a total length $L = ns$ have their post-buckling response analyzed. Face sheets and core struts have equal thickness $t_f = t_c = t$. Global and local sinusoidal imperfections of amplitude $w_g^0 = L/100$ and $w_l^0 = 0.001s$, respectively, are present.

Unit cell density is defined for the X-core setup with $t_f = t_c$ as

$$\rho = \frac{2(1 + \sqrt{2})td}{(d + t)s} \quad (6.3)$$

Three densities, named cases A-C, are taken for inspection. The thicknesses and core rotational restraint, computed according to Section 4.2 ($\kappa_c = 4EI_c/p$), are given by

$$A: \quad t = 0.01s \quad \rightarrow \quad \rho_A = 0.05, \quad \kappa_c = 1067 \text{ kN} \quad (6.4a)$$

$$B: \quad t = 0.02s \quad \rightarrow \quad \rho_B = 0.09, \quad \kappa_c = 8537 \text{ kN} \quad (6.4b)$$

$$C: \quad t = 0.04s \quad \rightarrow \quad \rho_C = 0.19, \quad \kappa_c = 68297 \text{ kN} \quad (6.4c)$$

The microscopic *force vs. strain* response for cases A-C is presented in Figure 6.11. The boundary conditions of the homogenized model can be written as

$$\begin{aligned} x = 0: \quad w(0) = \phi(0) = P(0) = 0, \quad N(0) = F \\ x = L: \quad u(L) = w(L) = \theta(L) = \phi(L) = 0 \end{aligned} \quad (6.5)$$

The boundary sectional rotation is ϕ constrained but the slope θ is non-zero to represent pinned top and bottom face sheets in the equivalent discrete structure.

The finite element shown in Section 3.6 is utilized in conjunction with the adapted cylindrical arc-length method (Algorithm 3) to trace the nonlinear equilibrium paths. The Feng criterion (see Ref. [37] for details) is utilized, as observed to be a good continuation predictor. The convergence tolerances are set to $\varepsilon_{tol} \leq 10^{-4}$ in all analyses.

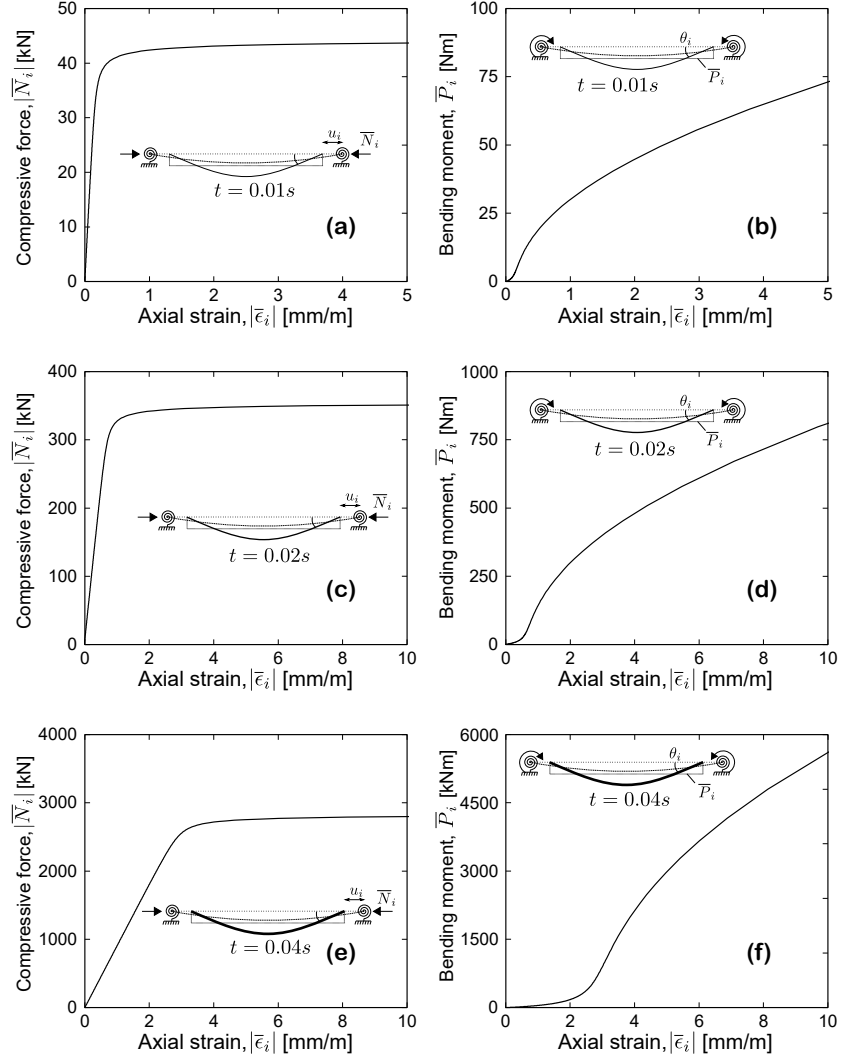


Figure 6.11. Microscopic internal forces that define the nonlinear face sheet response under compression (a)/(b) $t = 0.01s$ (c)/(d) $t = 0.02s$ (e)/(f) $t = 0.04s$.

Size-effect analysis

The buckling loads obtained with the homogenized model for n -cell X-core beam structures are compared with buckling equations obtained from the literature [34, 4, 179], where analytical antiplane core stiffnesses (Eq. 3.21) apply

$$N_g = \frac{\frac{2k_g^4\pi^4 D_f D_0}{L^4} + \frac{k_g^2\pi^2 D_g D_Q}{L^2}}{\frac{k_g^2\pi^2 D_0}{L^2} + D_Q} \quad (\text{global buckling}) \quad (6.6a)$$

$$N_w = 2\left(\frac{k_l\pi^2 D_f}{s^2}\right) \quad (\text{wrinkling}) \quad (6.6b)$$

The factor k_g in Eq. 6.6a is effective global column length, taken as $k_g = 4.0$ (fixed-fixed). In Eq. 6.6b, the column length of the faces k_l may be obtained based on a modified Newmark approximation [121, 12]

$$k_l = \frac{(0.4 + k_{sr})^2}{(0.2 + k_{sr})^2} = 2.34 \quad (6.7)$$

where the semi-rigid coefficient k_{sr} is obtained for the X-core as

$$k_{sr} = \frac{EI_f}{s} \left(\frac{4EI_c}{p} \right)^{-1} = 0.18 \quad (6.8)$$

where $EI_f/EI_c = 1$. Eq. 6.6a includes the global contributions of Euler-type and shear buckling [42].

Figure 6.12 shows buckling load comparisons as function of the relative unit cell size for different cell densities. The buckling loads of the homogenized and three-dimensional validation models are estimated based on the maximum force obtained from the nonlinear force-displacement curves. The relative size ratio s/L and cell density ρ are governing parameters describing the influence of a single unit cell in the global response.

The homogenized beam successfully predicts buckling loads regardless of relative size or unit cell density. The median error among the n -cases studied is 0.9% ($\rho = 0.05$), 0.7% ($\rho = 0.09$) and 0.7% ($\rho = 0.19$). The envelope of analytical equations is only moderately accurate if the response is clearly either global or local. That is, the analytical equations become more accurate as the cell density increases, or for points in the ends of the s/L spectrum. Generally, scale interactions govern the response; the scale interaction zone is shown to be wider in beams composed of lower-density unit cells. The present homogenized model succeeds as it incorporates microscopic effects in the average macroscopic response through modified stiffness parameters.

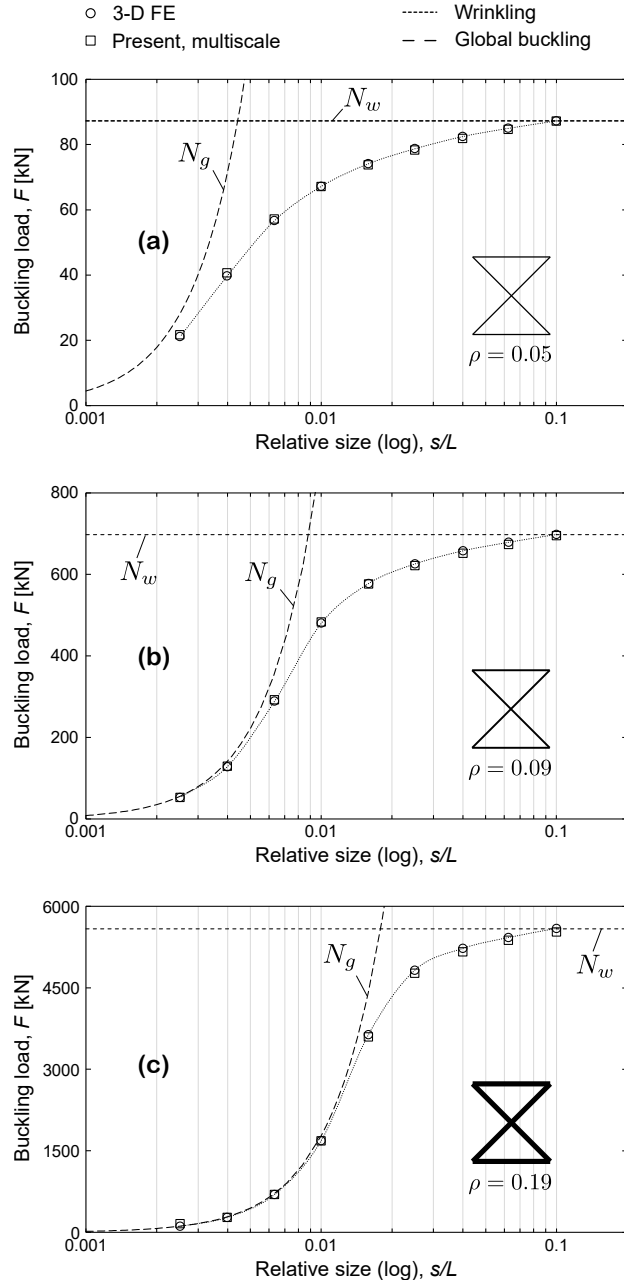


Figure 6.12. Buckling loads predicted for X-core sandwich beams as function of relative size s/L and cell density ρ with (present) homogenized beam, 3-D FE validation model and closed-form global buckling and wrinkling equations: (a) $\rho = 0.05$, (b) $\rho = 0.09$ and (c) $\rho = 0.19$.

Response assessment

Detailed response assessment is conducted as follows for cases extracted from Figure 6.12. Three contrasting configurations are selected: $s/L = 0.1$, $s/L = 0.01$ and $s/L = 0.00251$. Figure 6.13, Figure 6.14 and Figure 6.15 show *load vs. end-shortening* and *load vs. maximum deflection* relations obtained for the selected cases with $\rho = 0.05$, $\rho = 0.09$ and $\rho = 0.19$, respectively.

Overall, the homogenized beam with nonlinear stiffnesses predicts the progressive buckling responses with good accuracy against the validation models. Thanks to the modified arc-length implementation, descending post-buckling paths are also successfully described. Such description would not succeed with a standard Newton-Raphson implementation.

For all densities considered, $s/L = 0.1$ depicts a local response, where widespread wrinkling over the beam length is observed. The *load vs. end-shortening* relations correlate with the nonlinear stiffness of both face sheets combined, as may be verified by contrasting with Figure 6.11. Upon the onset of buckling, the structure becomes a mechanism and deflections increase with negligible incremental force.

For $s/L = 0.00251$, the response is majorly global for all densities assessed. Local face sheet buckling at the most stressed unit cells reduces the global capacity, effect which is more pronounced as the cell density is reduced. Slight stiffness reserve is present after the buckling point in higher-density cells.

In all $s/L = 0.01$ cases, scale interactions define the response. As implied from Figure 6.12, the interactions lead to somewhat different response for each density studied. The local buckling influence is inversely related to the density. Figure 6.13b and Figure 6.14b show approximately linear paths with a clear peak and descending branch. In the homogenized model, small stiffness changes due to local buckling initiation (axial stiffness reduction and increase in local bending parameters) are sufficient to trigger sudden global instability. In Figure 6.15b the response is mostly global. The homogenized beam stiffness reductions lead to gradual deterioration in the global capacity as the strain increases.

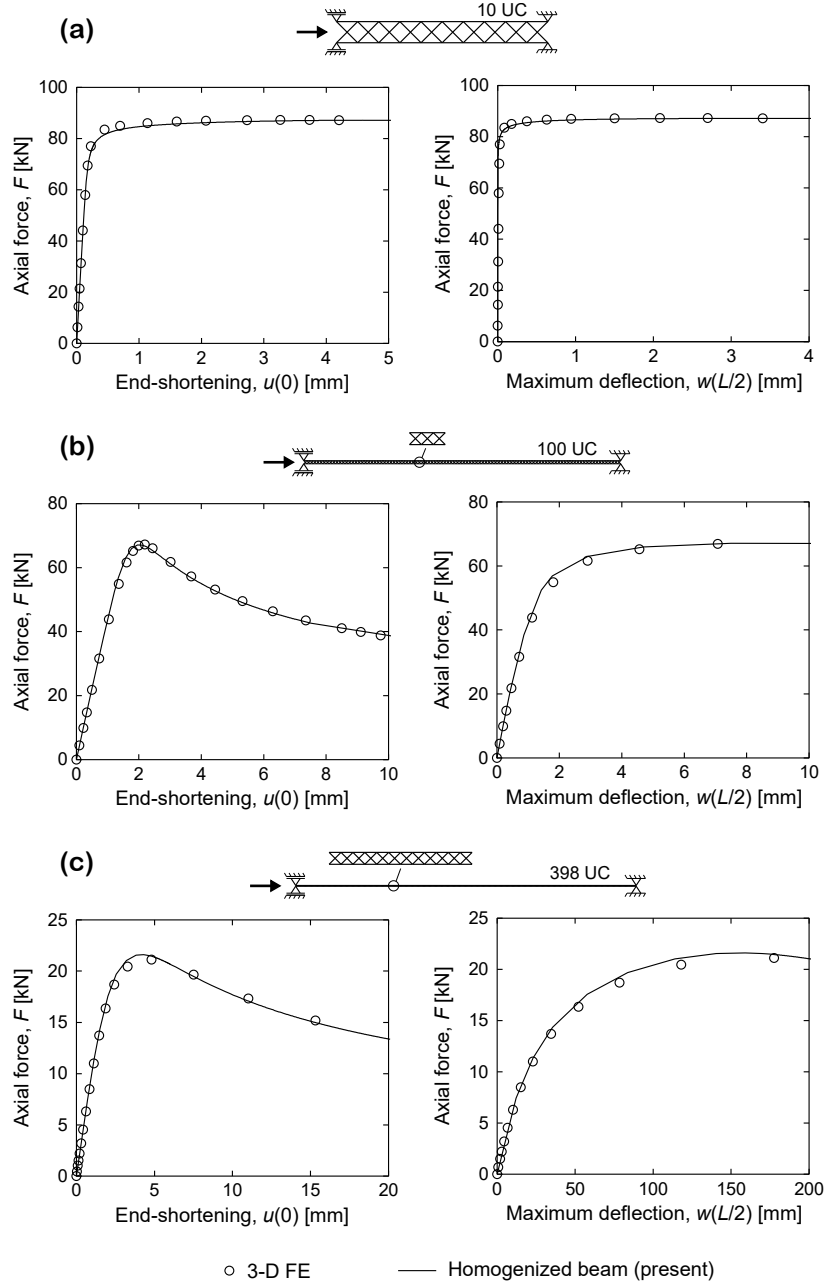


Figure 6.13. Load vs. end-shortening and Load vs. maximum deflection relations for fixed-fixed X-core beams with cell density $\rho = 0.05$ under axial compression; (a) $s/L = 0.1$, (b) $s/L = 0.01$ and (c) $s/L = 0.00251$.

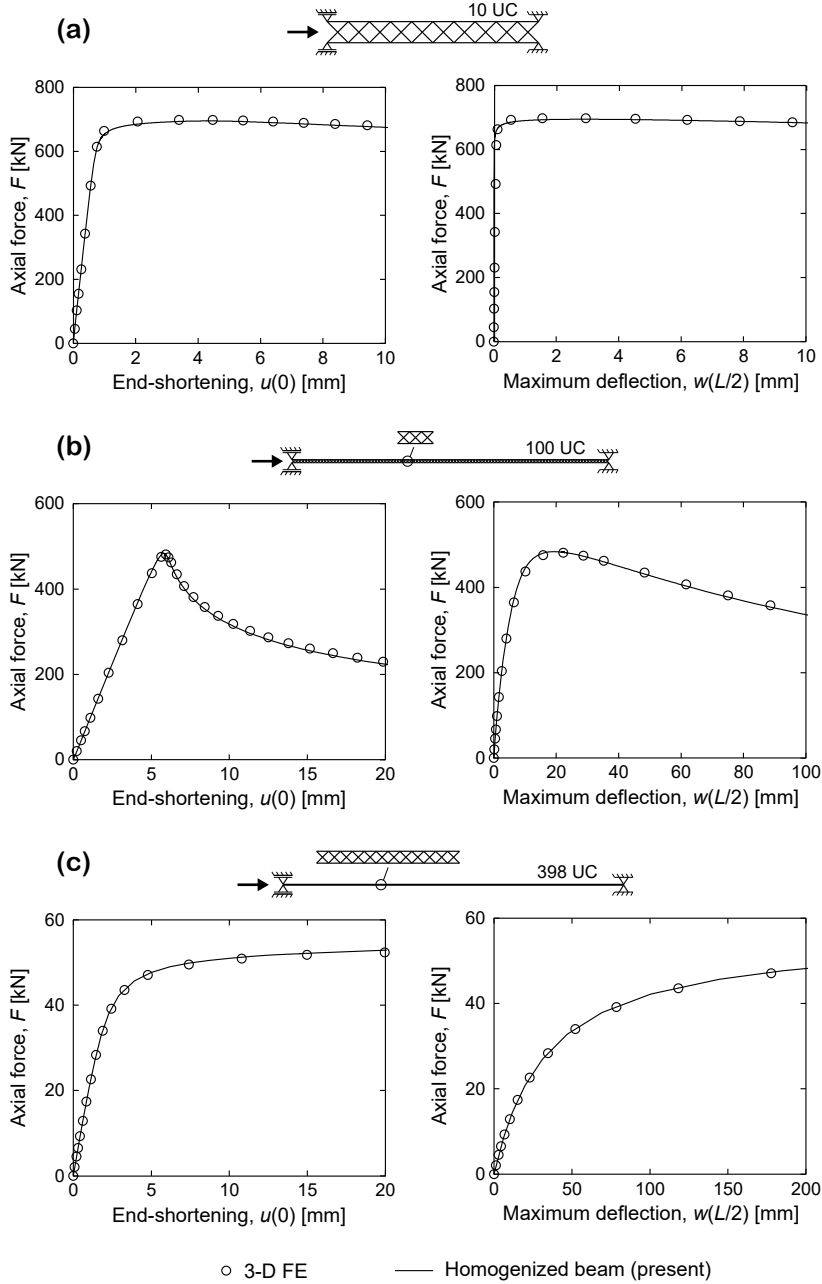


Figure 6.14. Load vs. end-shortening and Load vs. maximum deflection relations for fixed-fixed X-core beams with cell density $\rho = 0.09$ under axial compression; (a) $s/L = 0.1$, (b) $s/L = 0.01$ and (c) $s/L = 0.00251$.

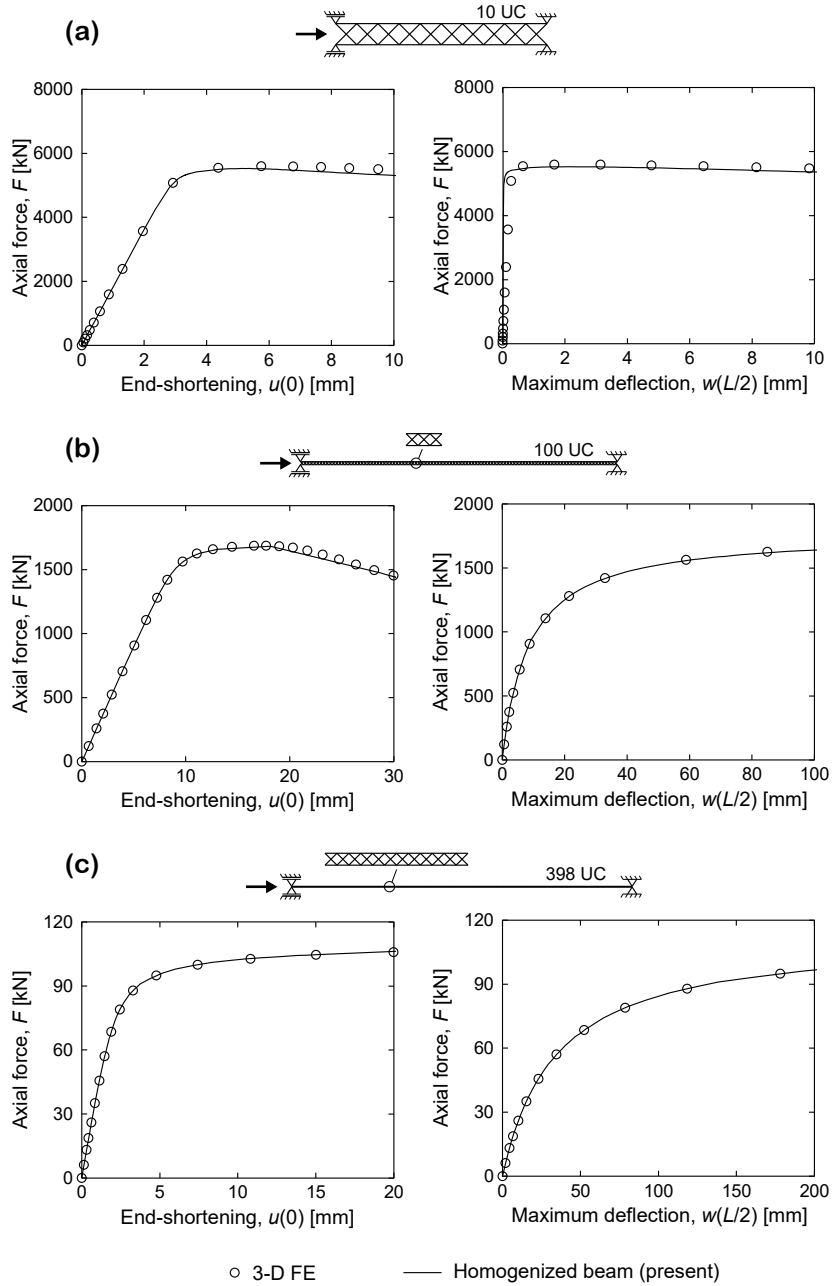


Figure 6.15. Load vs. end-shortening and Load vs. maximum deflection relations for fixed-fixed X-core beams with cell density $\rho = 0.19$ under axial compression; (a) $s/L = 0.1$, (b) $s/L = 0.01$ and (c) $s/L = 0.00251$.

Influence of \bar{B}_i parameters

A comparison of predicted responses using the general constitutive model or a simplified symmetric constitutive model ($\bar{B}_1 = \bar{B}_2 = 0$) is presented next. Unit cell density $\rho = 0.05$ and two relative cell ratios, $s/L = 0.1$ and $s/L = 0.025$ are selected; in either case, the local nonlinear response is relevant.

Figure 6.16 shows that the global buckling load predictions obtained are similar. The simplified model yields an overly soft post-buckling path in Figure 6.16a, as the strain energy due to secondary bending is significant after the global stability is lost. In Figure 6.16b, both constitutive models yield similar results due to the lower influence of local effects in the global response.

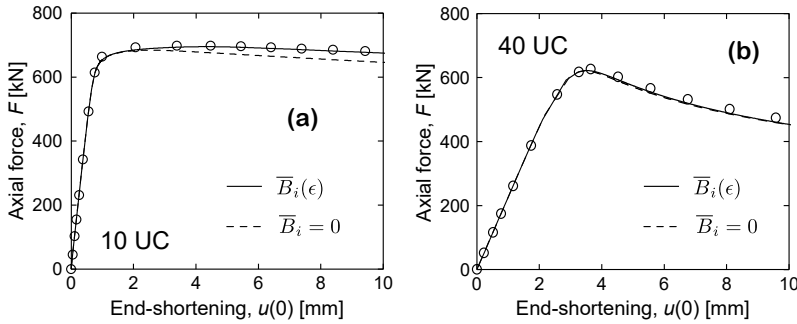


Figure 6.16. Comparisons between complete and simplified constitutive model. Density $\rho = 0.09$ and (a) $s/L = 0.1$, (b) $s/L = 0.025$.

6.4 Comparison between classical and present models

Classical Cauchy and couple stress-based models with or without macro-micro nonlinear scale interactions are compared in terms of buckling prediction accuracy, having 3-D finite-element results as reference.

Web-core and X-core sandwich beams are selected as representative of size-dependent and local buckling sensitive setups. For the comparisons, beams with unit cell density $\rho = 0.15$ (15%) and different relative sizes s/L are studied. The densities are attained with different thickness ratios t_f/t_c , calculated as

$$\text{Web-core: } \rho = \frac{2st_f + (d - t_f)t_c}{s(d + t_f)} \quad (6.9a)$$

$$\text{X-core: } \rho = \frac{2st_f + 2\sqrt{2}(d - t_f)t_c}{s(d + t_f)} \quad (6.9b)$$

A total of nine combinations of $s/L = 0.1, 0.0159, 0.0025$ and $t_f/t_c = 0.5, 1, 2$, is considered as summarized in Table 6.1. Figure 6.17 demonstrates the size-effect and local buckling sensitivities obtained in each case.

	Web-core			X-core		
	t_f [m]	t_c [m]	L [m]	t_f [m]	t_c [m]	L [m]
Ia	0.00398	0.00796	1.0	0.00203	0.00406	1.0
Ib	0.00398	0.00796	6.3	0.00203	0.00406	6.3
Ic	0.00398	0.00796	39.8	0.00203	0.00406	39.8
IIa	0.00536	0.00536	1.0	0.00327	0.00327	1.0
IIb	0.00536	0.00536	6.3	0.00327	0.00327	6.3
IIc	0.00536	0.00536	39.8	0.00327	0.00327	39.8
IIIa	0.00648	0.00324	1.0	0.00648	0.00324	1.0
IIIb	0.00648	0.00324	6.3	0.00648	0.00324	6.3
IIIc	0.00648	0.00324	39.8	0.00648	0.00324	39.8

Table 6.1. Cases proposed for a sensitivity analysis on the model suitability.

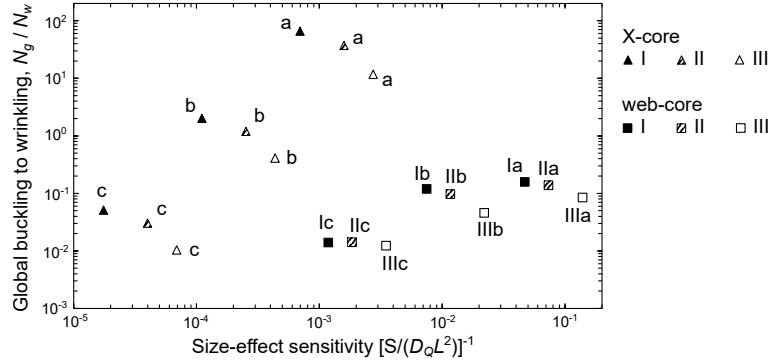


Figure 6.17. Cases defined in Table 6.1 in terms of their local buckling sensitivity (i.e. wrinkling to macro-buckling ratio) and size-effect sensitivity ratio.

The web-core sandwich beam has semi-rigid joints, with rotational stiffness $k_\theta = 100$ kN (see Ref. [149] for experimental k_θ values). The X-core is assumed rigid, as the connection does not significantly influence the stiffness behavior. The beams have global and local sinusoidal imperfections, with respective amplitudes $\alpha_g = L/100$ and $\alpha_l = 0.0002$ m. Figure 6.18 shows the microscopic relations of a periodic segment, while Figure 6.19 shows the relations for a boundary segment with $\theta_i(x_a) = 0$. Unlike the previous examples, boundary microscopic relations are needed for accurate predictions due to the discrete face sheet slope boundary conditions at the fixed end. The relations are based on the core rotational restraints $k_c = Et_c^3/3p$ and $k_c = Et_c^3/8d$ for X-core and web-core, respectively.

The macroscopic beam boundary conditions, considering the mid-length symmetry at $x = L/2$, are given by

$$\begin{aligned} x = 0: \quad & u(0) = w(0) = \theta(0) = \phi(0) = 0 \\ x = L/2: \quad & u(L) = \theta(L) = \phi(L) = 0, \quad V(L) = -P/2 \end{aligned} \quad (6.10)$$

In the equivalent discrete structure, the face sheet slopes are constrained. The modified cylindrical arc-length method (Algorithm 3) with Feng continuation is utilized to trace the nonlinear equilibrium paths. Convergence tolerances $\varepsilon_{tol} \leq 10^{-4}$ are used.

The critical buckling loads are computed using the following models

- Classical Timoshenko model, macroscale only (TBT)
- Classical Timoshenko model, macro-micro approach (TBT-M)
- Couple stress-based model, macroscale only (CSST)
- Couple stress-based model, macro-micro approach (CSST-M)

For the classical Timoshenko model, an antiplane core is assumed to define the stiffnesses.

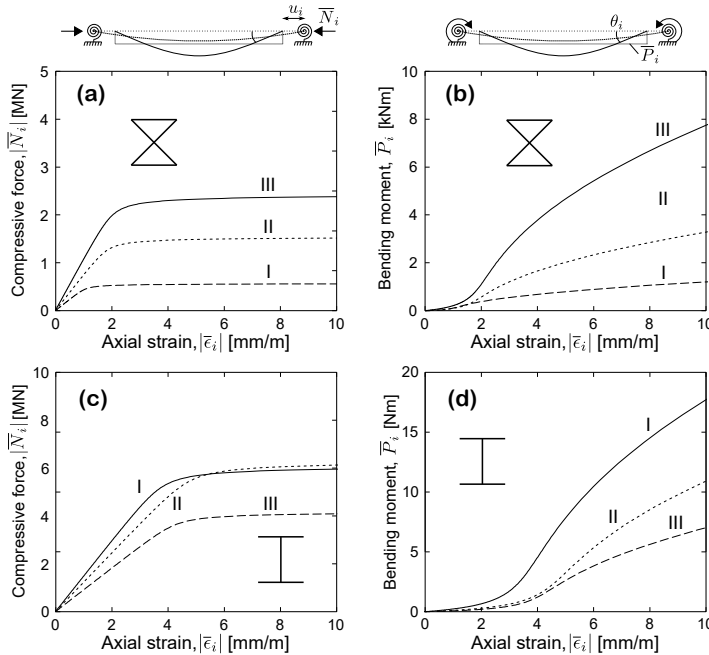


Figure 6.18. Microscopic relations that define the nonlinear face sheet response under compression (Cases I-III, X- and web-core).

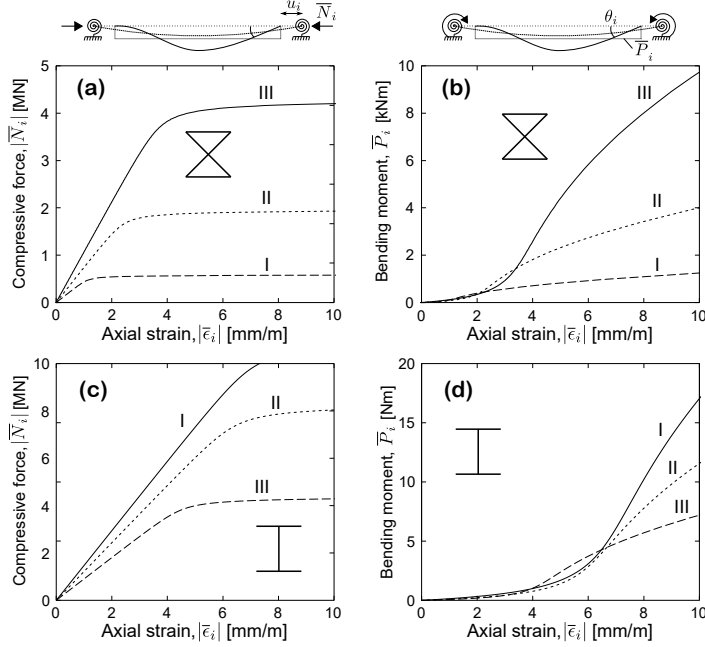


Figure 6.19. Microscopic relations that define the nonlinear face sheet response under compression (Cases I-III, X- and web-core).

Figure 6.20 shows the buckling loads obtained with the present multiscale approach and classical antiplane Timoshenko model. Figure 6.21 and Figure 6.22 show the percent errors obtained for each of the 18 cases, computed in relation to the equivalent 3-D FE models. Very good agreement between the predictions of the present approach and validation models is observed. The median absolute errors are 0.2% and 0.8% for web-core and X-core, respectively. The maximum error is 4% (Case IIIa). Slightly less accurate predictions are observed in beams that fail due to wrinkling, as are more sensitive to the correctness of the microscopic model assumptions such as the k_c estimate. Minor differences are seen in thin-faced cases Ia and Ib due to the simplified shear description of the present model.

Figure 6.21 shows that the Cauchy models are less accurate when short, thick-faced web-core beams are concerned due to the underlying size effects. The errors are proportional to the sensitivity parameters shown in Figure 6.17. In the short beams, the face own-axis bending stiffness accounts for a considerable portion of the buckling resistance, and thus the classical Timoshenko model is inaccurate. For the web-core dimensions here selected, one- and multiscale model output approximately the same results; in all cases, local and global buckling are clearly separated, and global buckling occurs with very minor local deformation of the faces.

The X-core beams with relative sizes $s/L = 0.1$ and $s/L = 0.0159$ (cases *a* and *b*, respectively) are prone to local buckling, as evident from their high wrinkling to macro-buckling ratios in Figure 6.17. In Figure 6.22 and Figure 6.20d-f, the effect of local face sheet buckling in the critical load predictions is evident. The error obtained with microscale-independent models is significant in most cases; it becomes larger as the face sheet thickness is reduced and as the beams become shorter. For the shortest beams ($s/L = 0.0159$), wrinkling failure is observed for all face-core thickness ratios t_f/t_c . Given the low size effect sensitivity ratios, Cauchy and couple stress-based models provide similar predictions overall.

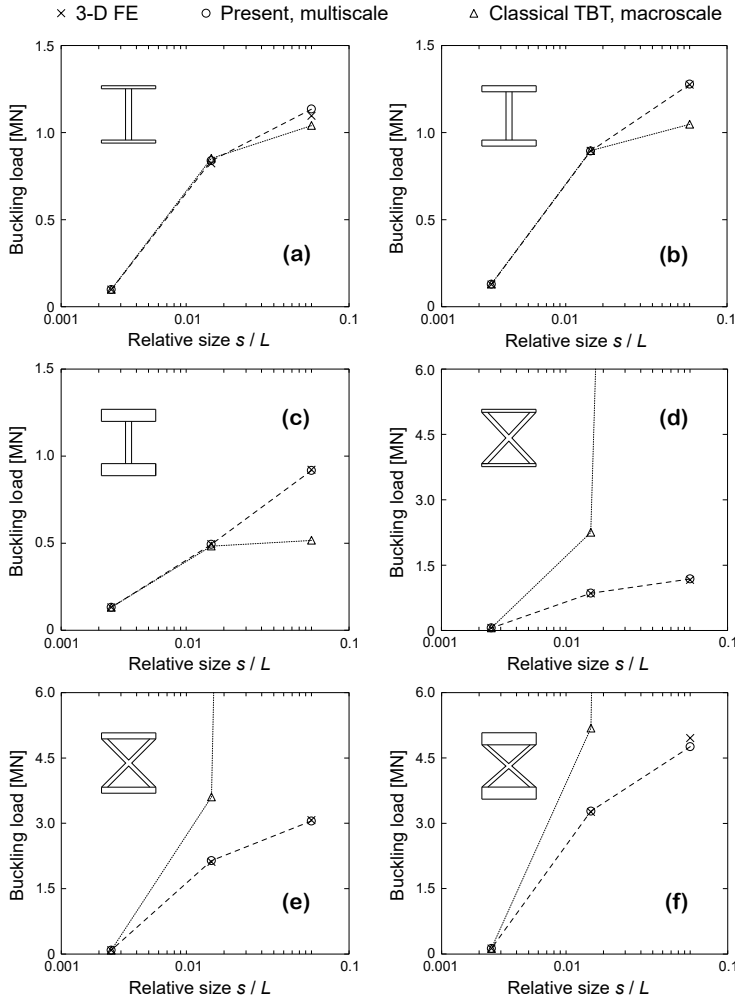


Figure 6.20. Critical buckling loads predicted with CSST-M (present), TBT and 3-D FE validation models for web-core and X-core sandwich beams with different t_f/t_c ratios.

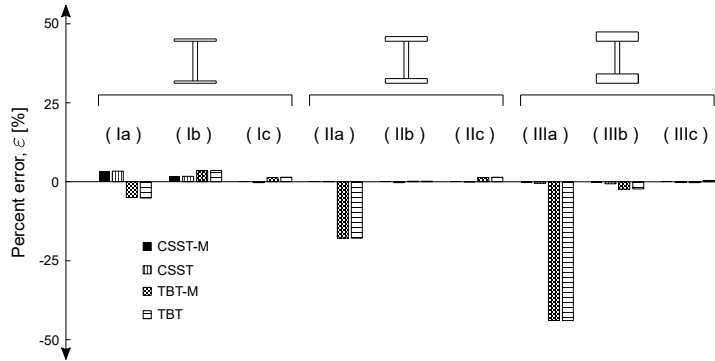


Figure 6.21. Percent errors obtained for nine web-core configurations (Table 6.1) as obtained with couple stress- and classical Timoshenko-based models with or without microscale stiffness effects.

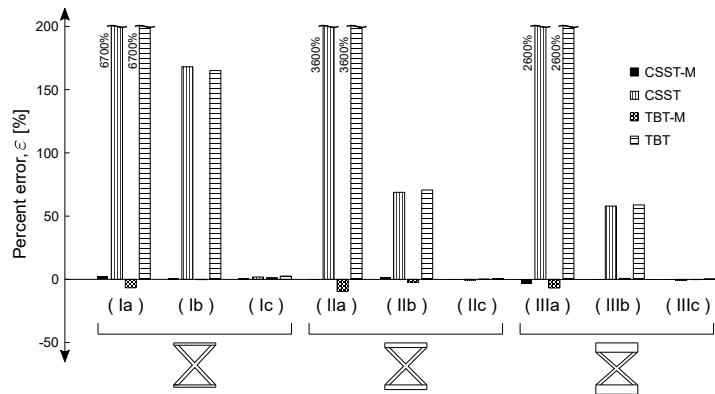


Figure 6.22. Percent errors obtained for nine X-core configurations (Table 6.1) as obtained with couple stress- and classical Timoshenko-based models with or without microscale stiffness effects.

7. Size effect sensitivity analyses

Stiffness size-independence is a basic assumption upon which the classical Cauchy continuum was constructed. In the classical continuum, structures have the same relative stiffness irrespective of their size, what has been verified as a reasonable assumption for most engineering materials. Certain low-density materials such as foams [5] or lattice grids [13], however, significantly violate this simplification and require more involved theories for consistent analysis of differently sized structures. Like other lattice-type materials, corrugated sandwich beams with shear-flexible cores exhibit size effects [59] triggered by shear force discontinuities.

While the Timoshenko model describes the shear deformation through a constant shear angle, the size-effect sensitivity can be related to its derivatives. In the present model, the cells are assumed to bend to a constant average curvature, and size effects are modeled through the first shear angle derivative. In the analyses that follow, the size-dependent response of linear elastic corrugated sandwich beams is investigated in relation to governing parameters.

7.1 Effect of cell geometry and density

In the present model, the parameter ζ may be used to quantify the size effect magnitude as function of the cell characteristics

$$\zeta_a \leq \zeta \leq \zeta_b \quad (C_3 \leq 0), \quad \zeta_a = \sqrt{\frac{S + C_3}{D_Q L^2}}, \quad \zeta_b = \sqrt{\frac{S}{D_Q L^2}} \quad (7.1)$$

where the changes in numerator delimit bounds. If the shear discontinuity has a localized effect on the global response, $\phi \approx \theta$, the size effect sensitivity tends to ζ_a and vice-versa. Typically, for practical cores, $\zeta_a \approx \zeta_b$. Equation 7.1 implies that size effects in corrugated sandwich beams depend on the core setup. The notion of stretch-dominated and bending-dominated shear-carrying mechanisms is important to classify the core behavior.

7.1.1 Governing ratios: a simple cell

Take as initial example a web-core beam with rigid joints. Assuming that $t_f^2 \ll d^2$, $\zeta = \zeta_a = \zeta_b$ can be simplified as

$$\zeta = \sqrt{\frac{1}{12} \left(\frac{s}{L}\right)^2 \left[2 \left(\frac{d}{s}\right) \left(\frac{t_f}{t_c}\right)^3 + 1\right]} \quad (7.2)$$

in which the governing ratios s/L , d/s and t_f/t_c are identified. Their significance in structural response predictions is studied in a simple example. Consider the linear elastic analysis of web-core sandwich beams with $t_c = 0.004$ m and $s = 0.012$ m in three-point bending. The governing ratios shown in Eq. 7.2 are varied one at a time, while the other two are maintained constant.

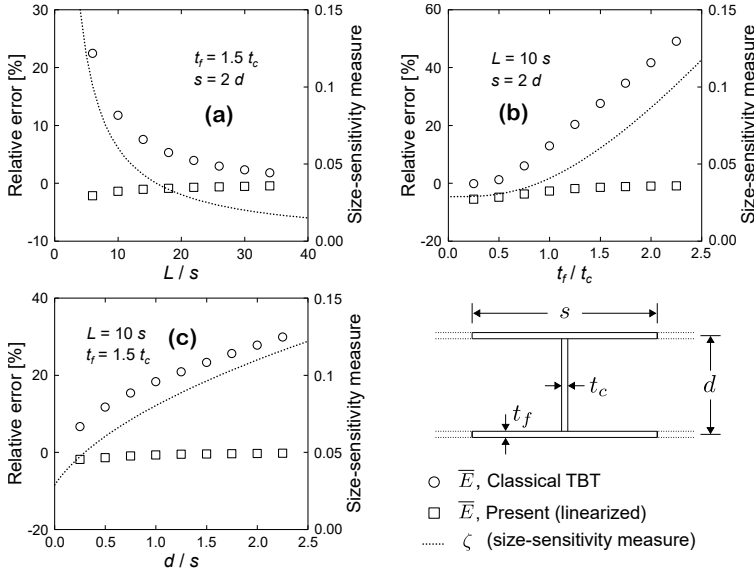


Figure 7.1. Percent error obtained with present and classical Timoshenko models as function of web-core cell structural ratios.

Figure 7.1 shows the errors obtained with the present model and size-independent classical Timoshenko beam as function of the governing ratios of Eq. 7.2. The present model is accurate for all parameter combinations, and eventual errors are not clear functions of the size-effect ratios. Meanwhile, the classical Timoshenko beam results only converge to the three-dimensional finite element solutions when $\zeta \rightarrow 0$. Error magnitudes obtained with the classical Timoshenko beam correlate with the powers of the governing parameters as in Eq. 7.2.

7.1.2 Effect of core setup and governing ratios

Corrugated beams with four core setups and nine structural ratio combinations each are analyzed. Unity-length beams ($L = 1.0$ m) with $d = L/10$ have their governing ratios t_f/d and s/d varied. Figure 7.2 shows the corresponding size-sensitivity parameter $\zeta_b = \sqrt{S/(D_Q L^2)}$ in each case.

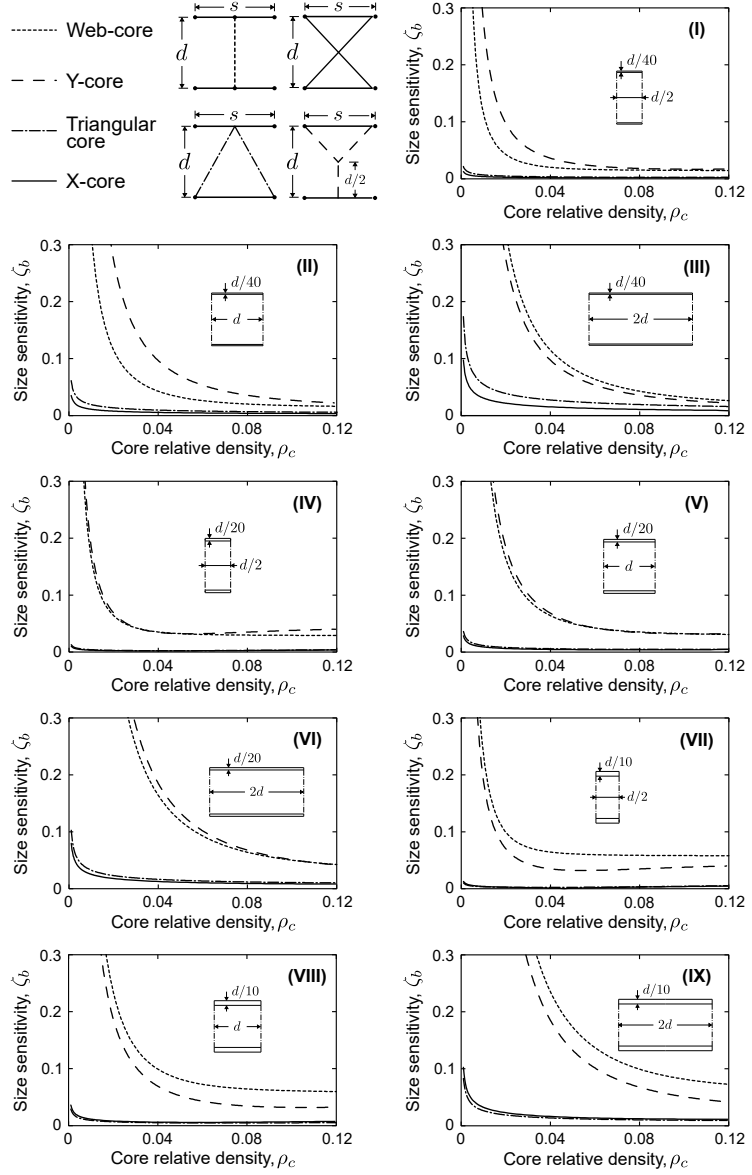


Figure 7.2. Size-effect sensitivity measure ζ as function of the core relative density for different corrugated cell arrangements and dimensions.

Figure 7.2 shows that, in the bending-dominated web-core and Y-core, the size-effect sensitivity highly depends on the core relative density. Conversely, stretch-dominated X-core and triangular cores are almost size-independent. The bending dominated cores have D_Q as a cubic function of the core thickness, whereas in stretch-dominated cores the dependency is linear. In all cases, $S \rightarrow D_f = EI_f$ as $t_c \rightarrow 0$. The figures also indicate that the ratio s/d influences the shear sensitivity as D_Q is function of the core strut angle and bending spans.

The core relative density effect on the size-dependency is further demonstrated by analyzing beams with cell dimensions of case **V** (Figure 7.2) under a centered point load and fixed ends (see Eq. 5.23). Figure 7.3 shows percent errors as function of ρ_c , as well as the prescribed force F needed to produce a maximum deflection of $w(L) = 0.01$ m. Overall, the present model can predict deflections for all cores satisfactorily. Conversely, the classical Timoshenko beam is only accurate when $\zeta \rightarrow 0$. For cases where $\zeta \rightarrow 0$, the homogenized models do not necessarily predict the same deflections due to the different assumptions on the core normal stress distribution.

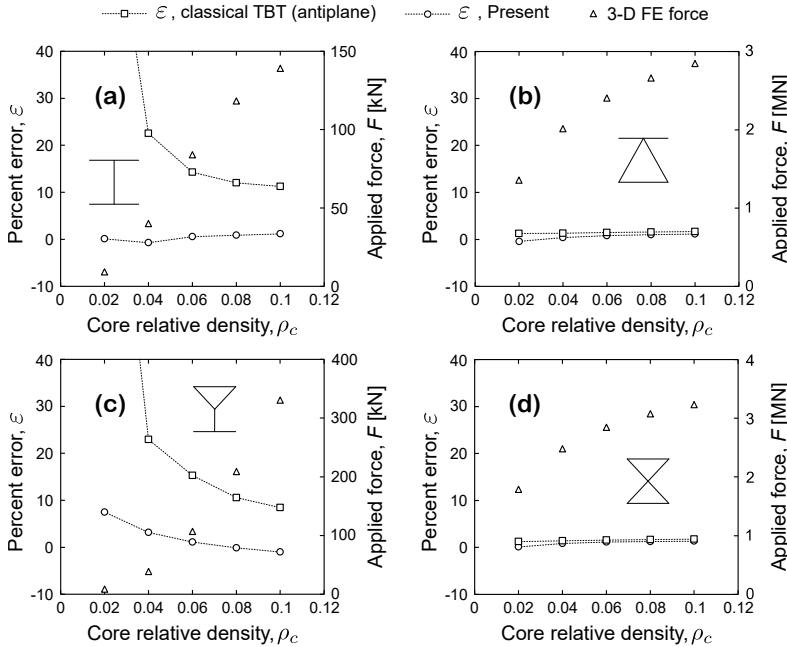


Figure 7.3. Percent error obtained with the present and classical Timoshenko antiplane models for the maximum deflections of fixed-fixed corrugated sandwich beams (varying core relative density) under a centered point force.

7.1.3 Effect of stacking sequence

To investigate the effect of stacking sequence in the size-effect sensitivity of multilayered cores, diamond and honeycomb core structures with different corrugation orders n (see Figure 4.6) are studied in bending. A setup with fixed-fixed boundary conditions and centered vertical force (see Eq. 5.23) is selected. The beam length is $L = 1.0$ m, whereas $s = L/10$ and $t_f = s/20$. The setups are regular; for diamond core beams $s = d$, while for the hexagonal core beams $s = \sqrt{3}p$. Low core relative density is taken in all cases, $\rho_c = 0.06$, and the thickness of core struts scaled accordingly.

Figure 7.4 shows the percent error obtained with present and classical Timoshenko beam models as function of n . The force necessary to produce unity (1 mm) displacement at mid-span is also depicted. Higher honeycomb corrugation order relate to somewhat higher error of the classical model as ζ increases slightly. Diamond core cells are not size-sensitive, regardless of n . The present model predictions are shown to be accurate for both setups regardless of the corrugation order.

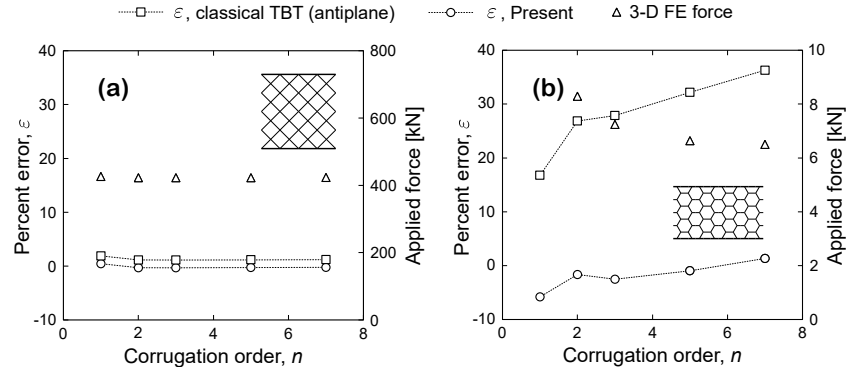


Figure 7.4. Percent error obtained with the present and classical Timoshenko antiplane models for the maximum deflections of fixed-fixed corrugated sandwich beams (varying stacking sequence) under a centered point force.

7.2 Effect of face-core connection stiffness

Bending dominated corrugated cores rely on the moment transfer capacity at face sheet-core connections to carry shear loads. Yet, manufacturing processes such as laser-welding may result in joints that are not nearly rigid. The transverse shear stiffness of the assembly is progressively reduced as the effectiveness of the connection reduces and, consequently, size effects are observed as the joint approaches a pinned behavior.

In this section, the effect of the joint rotational stiffness on the size-dependency is investigated through a simple example. Consider a web-core sandwich beam with overall length $L = 2.0$ m, composed of 10 cells with dimensions $s = 2d = 0.2$ m and $t_f = t_c = 0.005$ m. The beam has semi-rigid face sheet-core joints, modeled as rotational springs with stiffness per unit width $30 \leq k_\theta \leq 3 \cdot 10^8$. The scale parameter of Eq. 7.2 ($\zeta = \zeta_a = \zeta_b$) can be written (approximately) as

$$\zeta = \sqrt{\frac{s(k_1 t_f^3 t_c^3 d^2 + 2d^3 t_f^3 + d^2 s t_c^3 + s t_f^2 t_c^3)}{12d^2 t_c^3 L^2}} \quad (7.3)$$

The following boundary conditions are considered

$$\begin{aligned} x = 0: \quad & w(0) = \theta(0) = \phi(0) = 0, \quad N(0) = F \\ x = L: \quad & u(0) = w(L) = \theta(L) = \phi(L) = 0 \end{aligned} \quad (7.4)$$

Figure 7.5 shows the critical buckling loads predicted with the present model as function of k_θ , which are validated against equivalent 3-D FE models and compared with the classical Timoshenko model. The critical buckling load yield by the classical model is given by

$$F_{cr} = \frac{4\pi^2(D+S)L^2}{1 + 4\pi^2(D+S)/(D_Q L^2)} \quad (7.5)$$

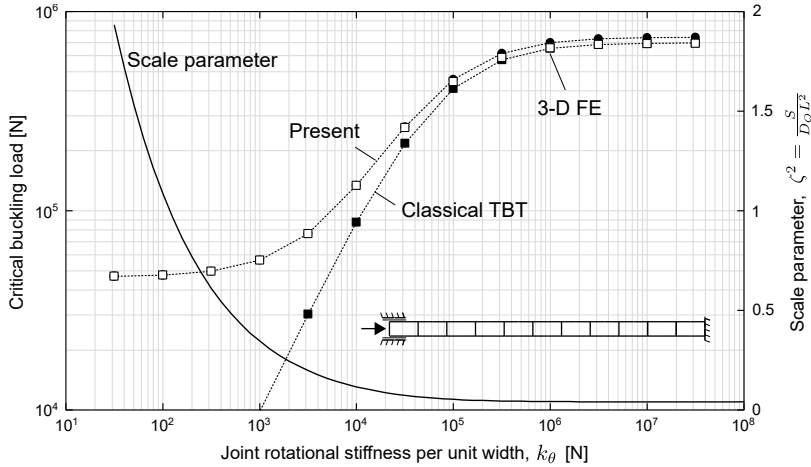


Figure 7.5. Critical buckling load predictions for a fixed web-core sandwich beam under a centered axial force as function of the joint rotational stiffness. Predictions based on the present, classical Timoshenko and 3-D FE models. The scale parameter ζ is also indicated.

Overall, Figure 7.5 shows that the classical Timoshenko model becomes progressively less accurate as the scale parameter increases. The present sandwich model successfully predicts the critical buckling load for the entire range of k_θ . The scale parameter tends to infinity as the joints approached pinned-like conditions. The web-core sandwich assembly then reduces to two unconnected beams, and the core becomes inactive. As the joints approach a rigid condition, the scale parameter converges to a constant, small yet non-zero value.

7.3 Effect of boundary conditions

Elastic size effects in sandwich beams are related to discontinuities that induce lengthwise shear angle variations. In this section, different sets of loading and boundary conditions are studied as to quantify their influence onto the size-dependent response of corrugated sandwich beams with different unit cell properties. Figure 7.6 shows four boundary conditions in which shear discontinuities are present. The discontinuities are related to point forces and slope boundary conditions that promote changes in the shear distribution diagram.

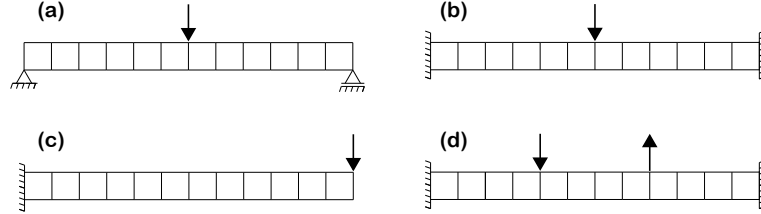


Figure 7.6. Boundary conditions for the sensitivity analysis (a) simply-supported beam under centered point force (b) fixed-fixed beam under centered point force (c) end-loaded cantilever (d) fixed-fixed zig-zag beam.

Setup	Core	t_f [m]	t_c [m]	ζ_b
A	Web-core	0.006	0.004	0.0670
B	Web-core	0.004	0.0035	0.0480
C	Triangular core	0.00125	0.0025	0.0016
D	Triangular core	0.01	0.002	0.0129
E	Y-core	0.009	0.003	0.0780
F	Y-core	0.004	0.004	0.0271

Table 7.1. Configurations proposed for the investigation on the influence of boundary conditions in the size-dependent response of corrugated sandwich beams.

Six sandwich cell setups are proposed for the investigations as shown in Table 7.1. The general cell dimensions are $s = d = 0.1$ m, whereas core type and thickness, as well as face thickness are varied to obtain data points in $0 \leq \zeta_b \leq 0.08$. (see Eq. 7.1). Figure 7.7 shows the errors obtained with present and classical antiplane Timoshenko model for the setups of Table 7.1 and boundary conditions of Figure 7.6. Error is defined as the relative difference between deflections under the point force predicted with the homogenized and equivalent 3-D FE validation models. In the zig-zag beam, the forces result equal in magnitude given the geometric symmetry.

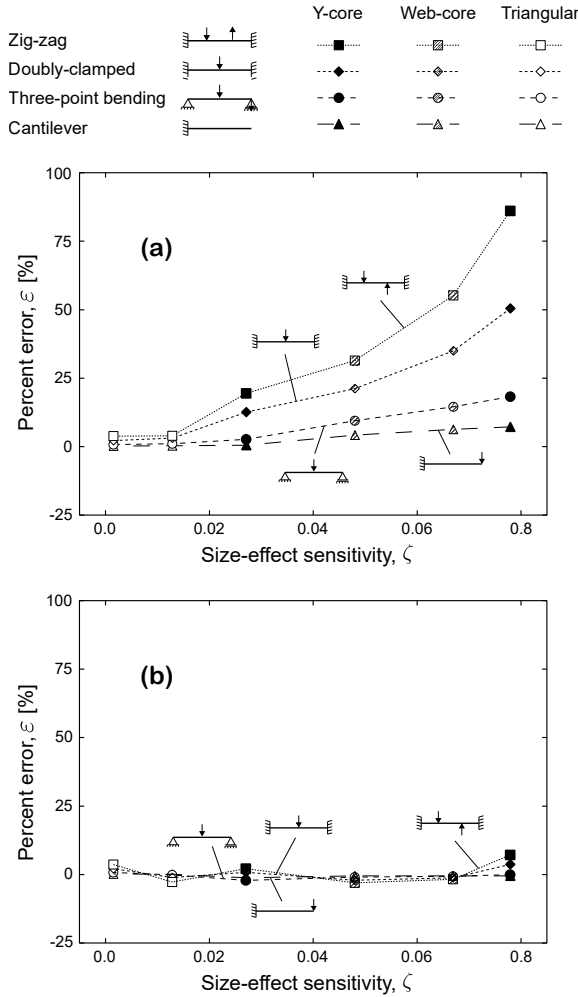


Figure 7.7. Percent error (deflection under the point force) obtained with (a) classical Timoshenko (antiplane) and (b) present model for different beam setups as function of the upper-bound size-effect sensitivity parameter.

Figure 7.7a shows that the classical Timoshenko beam error scales with the size-effect parameter ζ . The error is larger in the zig-zag setup as multiple shear discontinuities are present, whereas it is the lowest for the cantilever beam. The three-point bending case is equivalent to a cantilever beam with length $L/2$, thus their errors are scaled by a factor of two, approximately. Figure 7.7b shows that the present model is considerably more accurate in all size-sensitive cases and no correlation between size-effect sensitivity parameter and error is evident.

8. Discussion

The present work defined a modeling approach for corrugated sandwich beams that contains nonlinear information from consecutive scales. The scales and their interrelationships were defined, along with application to selected sandwich setups of practical relevance. Contrary to conventional approaches, the macroscopic formulation provides basis to capture size effects in simple fashion. Moreover, the approach is able to predict microscopic nonlinearities such as local buckling by simple progressive modification of the macroscopic constitutive matrix. In the following subsections, the modeling assumptions, and relevance to response prediction and practical application are discussed. Directions for future work are then provided.

8.1 On the assumptions and approach

In contrast to other non-classical models, the modified couple stress Timoshenko beam [143, 7, 111] provides a minimum amount of independent parameters to describe the response of shear-flexible sandwich beams. Micropolar-based models [84, 120, 86] are conceptually similar, yet convey a more involved shear description. Other non-classical models could be employed to describe the underlying physics. An advantage of the modified couple stress model is the resemblance with the classical Timoshenko beam theory.

Unlike Cauchy-based models, the couple stress-based macroscale has a length-scale parameter, thus being capable of capturing size effects. Stress resultants defined as in Ref. [57] include a parameter to describe stiffening near structural discontinuities due to the cell own-axis inertia [59]. The cell bending stiffness is an average description; greater accuracy, particularly in stress predictions, would require the introduction

of higher-order displacement derivatives and related stiffnesses. In the absence of coupling between cell bending and the other axial stress-related stress resultants, the present model converges to the so-called thick-face sandwich theory [4, 139, 179] (in the linear bending case). Couplings are, however, necessary in fulfilling the Hill-Mandel condition (see e.g. Ref. [1]) and predicting accurate stress distributions in the analysis of most corrugated cores. Couplings are also utilized to include the strain energy due to secondary bending into the macroscopic equilibrium equations.

Corrugated sandwich beams are transversely flexible and a homogenized description requires a shear deformation measure. The Timoshenko-type model as chosen condenses shear strains, which are generally different in horizontal and vertical directions, into an average section slope. Higher-order shear deformation theories [141] or models with additional measures [84] can improve the shear description, yet an average section angle is sufficiently accurate in virtually all practical cases. The shear stiffness results from micromechanical analysis in similar manner as in Refs. [109, 54, 151]. As the strain energy is conserved in the averaging process, no additional shear correction factor is required (i.e. $K_s = 1.0$ in Eq. 3.9b). The transverse shear relations are linear; geometric nonlinearities are assumed not to substantially influence the unit cell shear behavior.

Stiffness determination is based on the micromechanical analysis of a repeating unit cell, wherein *mesoscopic* deformations are assumed small. Cell-average stiffness relations follow the lines of Sun and Vaidya [160] with a stress resultant level treatment as in Ref. [59]. Stiffness derivations were conducted using linear plane frame analysis with Euler-Bernoulli elements. Displacement boundary conditions and extraction of boundary tractions ensure strain energy conservation among scales [66, 70]. The plane-stress macroscopic assumption is maintained; in the derivation of normal stress-related resultants, the vertical boundary tractions are zero, while displacements (and related strain) are generally non-zero. Stiffness derivations are analogous to previous works [105, 21, 109, 53, 54], while considering the enhanced macroscale and incorporating scale transitions. Corrugated cells with core strut continuity have decoupled normal and couple stress-related phase responses: the stiffnesses have independent face sheet and core components. Meanwhile, unit cells with discontinuous core have more intricate stiffness relationships, and the core stretch-related stiffnesses are also function of the face sheet properties. As the core is unable to transfer normal stresses directly, however, the expressions tend to an antiplane state.

Macroscopic stiffness updates due to cell nonlinearities are confined to nonlinear stiffness coefficients in similar spirit as proposed by Byklum and colleagues [24, 25] and Ref. [56]. These references, however, modified stiffnesses element-wise and lack scale-dependent parameters. As meant for relatively thick panels, the model in Refs. [24, 25] did not include the effect of shear deformation. Nonlinear stiffnesses were also utilized in Rabczuk et al. [140]; there, the core of each unit cell is homogenized into a shell element with effective strain-dependent properties. The approach in [140] was shown able to satisfactorily describe substantially nonlinear core behavior. Unlike in a computationally-intensive FE2 method [47], in this work the analysis of the coupled scales is uncoupled and the microscopic equilibrium solved analytically based on slope-deflection equations [166, 8, 12].

As result of the pseudo-terms proposed, the macroscopic constitutive matrix becomes unsymmetrical in presence of local nonlinearities. A more conventional symmetric matrix implementation with $\bar{B}_1 = \bar{B}_2 = 0$ may be employed as a further simplification. Setting $\bar{B}_i = 0$ implies energy dissipation in presence of local buckling-related secondary bending, yielding a slightly overly soft global response.

The macroscopic equilibrium equations are solved using the displacement-based finite element method. The nonlinear element is based on derivations in Ref. [7] with further manipulations as described in Ref. [57]. The approximate tangent stiffness matrix of the Newton method neglects stiffness derivatives. Initial macroscopic imperfections are introduced via transformation matrices. Implicit solvers, namely the modified Newton-Raphson and cylindrical arc-length method [35] with the Feng continuation criterion [46, 37] were utilized in the analyses. The arc-length method was favored in the post-buckling analyses due to the occurrence of limit points; it is capable of adjusting the external force when the tangent of the equilibrium approaches a singularity point (see, for instance, Refs. [35, 36] for details). With the present modifications, the progressive update of stiffness parameters slows down the convergence rate, as the equations to be solved dynamically change and have a predictor-corrector sense. In constructing the stiffness matrices, reduced integration was utilized to avoid membrane and shear locking phenomena [144, 31].

The dissertation is limited to the study of face sheet geometric nonlinearities, which are of greater concern under typical service loads [16]. Incorporation of core strut buckling as observed in accidental limit states such as blast loading [181] and collisions [41] is left for future work. The

introduction of material nonlinearities is not presented in this document, but may be accomplished in analogous manner (yet, including thickness-integration during the analysis).

8.2 On the structural response

Examples were selected as to validate and assess the performance of the multiscale approach. In its linear form, the resulting two-scale (macro-meso) homogenized model outperforms conventional single-layer counterparts and provides accurate deflection and stress distribution estimates. Incorporation of nonlinear scale transitions was shown to enable the prediction of progressive, interactive local-global buckling. Other local nonlinearities may be incorporated in an analogous manner.

As shown in Section 5.2, the two-scale linear model matches the thick-face sandwich theory (see Refs. [4, 139, 179]) for an antiplane core. While an antiplane assumption is generally accurate for deflection analyses, incorporation of coupling terms is central in determining stresses. Examples have shown that the present model excels in predicting stress distributions. Local deviations due to higher-order cell bending, however, remain near structural discontinuities. Their prediction would require a more involved model with higher-order displacement gradients and corresponding stiffnesses, what is hardly justifiable in practice.

In a geometrically nonlinear setting, the multiscale approach was utilized to predict interacting elastic local-global buckling and post-buckling paths. Imperfections were assumed for numerical soundness; in fact, global and local imperfections may be substantial in corrugated sandwich structures [30] and affect their load-carrying capacity as discussed in Biagi and Bart-Smith [15], Jelovica [74] and Jelovica and Romanoff [75]. Laser-welding as a common manufacturing process can induce substantial distortions to thin-walled sections [30]. In the nonlinear studies, size-dependent behavior was observed in scale-sensitive beams.

Shear-stiff beams with thin face sheets were shown prone to local buckling, whereas global buckling is dominant for longer, shear-flexible setups. A wide transition range exists, where interactive local-global buckling occurs. In bending, face sheet buckles initiate at the highest bending stress region, whereas under uniaxial compression this depends on cell characteristics, structural length, imperfection shape and size. Local buckling may occur well into the elastic regime and prompt failure of the entire member in the absence of in-plane restraint (as in a simply-supported

beam). Membrane stiffening reduces the severity of local buckling in the overall integrity when in-plane displacement is restricted; local buckling then progressively propagates.

Buckling equations from sandwich constructions books [4, 179, 173] are often used to predict the critical buckling loads of corrugated sandwich beams as described in Valdevit et al. [171]. Ref. [16] presented failure maps based on these equations and showed that the elastic failure typically occurs at lower loads than the predicted values. In fact, the present study demonstrated that the envelope of analytical predictions fail to estimate the critical buckling load when local-global buckling interaction is present. In light of this, the present approach offers an inexpensive alternative to incorporate scale interactions in stiffness response assessments. Figure 8.1 shows a rational model selection diagram, which is based on the global buckling to wrinkling ratio P_G/P_w and the size-effect sensitivity ratio bound $[S/(D_Q L^2)]^{\frac{1}{2}}$.

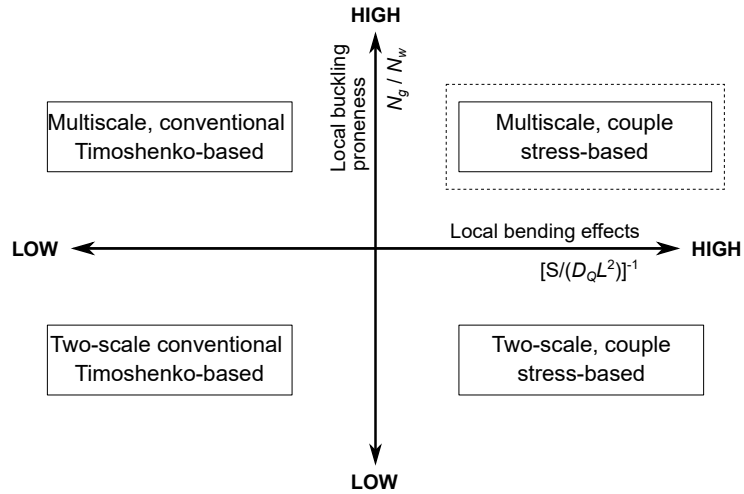


Figure 8.1. Four-field for model selection in the nonlinear buckling analysis of corrugated sandwich beams.

Size-sensitivity studies showed that short beams with low-density, bending-dominated cores and relatively thick face sheets are prone to display size effects. As in Ref. [59] and other studies on lattice-type structures [108, 5, 125], a scale-dependent parameter was shown necessary for their prediction. For equal boundary conditions, size effects lie within geometric bounds, related to the shear flexibility of the cell and size of the structure. Cores that transfer transverse shear loads through strut stretching have low size-effect sensitivity and vice-versa. Thus, a size-dependent model is

mostly relevant when bending-dominated sandwich cells are to be analyzed for stiffness.

8.3 Practical relevance and implications

The homogenized model aims to simplify the analysis of corrugated sandwich panels subjected to quasi-static loads. The approach is relevant for the preliminary analysis of complex lightweight structures, where design changes can be handled in the stiffness level and multiple analyses conducted in a reasonable time frame. Progressive global failure can be tracked accounting for member-level effects, such as local buckling. A material failure condition may be incorporated via a stress envelope analysis based on the upscaling rules that were shown.

Practical utilization would benefit from implementations of the concepts into a plate model (thus, removing the plane-strain assumption). The general ideas presented remain valid, and thus such extension is relatively straightforward. Similar approach has been defined by the Author for a classical first-order plate model [56].

8.4 Future work

The dissertation demonstrated the capabilities of single-layer modeling in predicting the response of corrugated sandwich beams with nonlinearities at consecutive structural scales. The work has revealed several areas for future research.

A plate model implementation of the concepts defined would extend the practical significance. Such model would require studying three-dimensional unit cells in the same spirit as in Ref. [56]. To predict more severe nonlinearities, extension to a large-strain setting as in Ref. [140] could broaden the range of applicability.

Future work could focus on implementing other local nonlinearities into the macroscopic constitutive matrix. Similar reasoning along with a strain-dependent thickness-integration scheme can be employed to handle moderate material nonlinearity. Core buckling may be described in a simplified manner by progressively adapting the transverse shear stiffness. The approach can be extended to include the effect of local loads within the face segments. The introduction of additional displacement derivatives can locally improve the stress prediction accuracy and allow the interaction between neighboring unit cells to be accounted for.

9. Conclusions

This dissertation presented a multiscale modeling approach for corrugated sandwich beams. The approach defines three interacting scales and their interrelationships. The *macroscale* represents the global structure through a homogenized size-dependent sandwich model. The *mesoscale* is a unit cell of the global structure, from which macroscopic constitutive information is derived. The *microscale* describes sub-cell behavior; in this study, the geometrically nonlinear response of the sandwich face sheets subjected to an uniform stretch. An iterative scheme computes, for every load increment and until energetic equilibrium, the macroscopic strains, updates the microscopic state and determines macroscopic stiffnesses based on the mesoscopic averaging rules. Small strains and moderate rotations are assumed at structural and sub-structural scales; the undeformed structure is the reference configuration. The approach can capture elastic size effects due to interacting scales and predict the influence of local nonlinearities in the global structural behavior. A recovery scheme based on linear superposition can be utilized to predict discrete stress distributions for moderately nonlinear response.

The *macroscopic* homogenized model is founded on the modified couple stress theory with Timoshenko beam assumptions. Constitutive relations describe four cell deformation modes that combined can describe the stiffness behavior of sandwich beams with different corrugated cores. Normal cell stresses are decomposed into three resultants: constant normal forces, global bending-inducing normal forces and constant cell bending moments. Three related strain components are defined: constant stretch, section differential stretch (zero-average) due to bending and constant cell curvature. The normal cell stress-related resultants and strains are coupled through eight independent constitutive parameters in the general case. Unit cell shear stresses are described by a linear equation as in the classical Timoshenko beam theory. A local shear component arises from the couple-stress

equations as a cell-moment derivative.

In the *mesoscopic* scale, a micromechanics-based approach determines the macroscopic stiffness averaging rules. Boundary displacements enforced to an unit cell model replicate the average macroscopic strains. The resulting boundary tractions are used to compute equivalent macroscopic stress resultants. The ratios between equivalent resultants and strains provide the parameters of the macroscopic constitutive matrix. A linear elastic mesoscopic model outputs constant stiffnesses that depend on cell geometry and material properties, while a nonlinear model is also function of the microscopic strain state and additional parameters influencing the microscopic behavior. Stiffness relations were derived for selected corrugated cells using conventional frame analysis, resulting in closed-form expressions that are function of the microscopic state. For a linear microscale, the expressions are functions of material and geometric unit cell properties only.

Nonlinear local second-order effects are embedded in the constitutive relations through a *microscopic* boundary value problem and a scale transition scheme. In the present work, the microscale describes the second-order nonlinear response of compressed face sheets (local buckling). The *microscopic* model is a conventional Euler-Bernoulli beam with von Kármán kinematics, solved analytically with help of slope-deflection equations. The macroscopic stretch-related strains are averaged and enforced as microscopic boundary condition. The resulting reaction forces are utilized to compute average macroscopic stiffnesses based on *mesoscopic* geometric relations. In the macroscopic level, the stiffness degradation describes a local load-carrying mechanism shift from face sheet stretching to bending - a less effective mode.

A finite element model was defined in line with previous works on the couple stress-based Timoshenko beam theory. Lagrangian linear and Hermitian cubic functions interpolate the kinematical variables. Following previous works, elemental secant and tangent stiffness matrices were provided. A nonlinear solution scheme was defined based on the modified Newton-Raphson method. To compute the post-buckling examples, an extension was conducted to obtain an arc-length-type scheme that can overcome limit points.

The approach was validated against equivalent three-dimensional finite element models and compared to other homogenized beam idealizations. Justification for a nonlinear scale-dependent sandwich model was provided in a series of examples, in many of which conventional approaches are

insufficient to provide a complete response description.

A *macroscopically* and *microscopically* deformation-independent model was determined and employed for displacement and stress analyses. Broad validity was demonstrated. Unlike the Cauchy-based antiplane Timoshenko model, the present model was shown to maintain good accuracy when scale interactions are significant. Critical buckling loads were successfully predicted with the linear model for a structure with dominant global response. The examples also demonstrated the capability of the stress localization scheme, which allows satisfactory predictions also when moderate scale interactions are present. In shear-stiff structures, face sheet stresses result mainly from direct integration of the macroscopic quantities, implying an approximately piecewise constant distribution. In shear-flexible structures, the response becomes piecewise linear due to recovery of zero-average shear terms.

The multiscale approach was then employed to trace (elastic) failure paths of beams undergoing geometric nonlinearities at different scales. Parametric studies demonstrated soundness irrespective of the setup. Stretch-stiffening in horizontally restrained beams was shown to be satisfactorily captured through the macroscopic von Kármán term. Progressive stiffness adaptations were shown successful in describing not only the first buckling point, but also the load-displacement relations past the initial failure as local buckling spreads to multiple cells. Linear superposition was shown to output satisfactory stress descriptions of moderately nonlinear beams. Nonlinear buckling of axially loaded beams was then studied and shown to be a major application potential of the present approach. In most cases, failures occur due to mode combinations, which cannot be predicted neither by well-known buckling equations nor by scale-independent homogenized models. The present approach was shown to excel with this respect, not only providing accurate buckling load estimates but also yielding accurate progressive failure paths at low modeling and computational costs.

In sensitivity studies, the parameters governing elastic size effects in linear elastic sandwich structures were identified. Besides the beam length, the effects of cell geometry, vertical stacking sequence (in multi-layered lattice-type cores), core relative density, member connection stiffness and macroscopic boundary conditions were assessed. It was shown that the size effect sensitivity can be quantified in a similar spirit as the shear deformation is quantified in sandwich construction textbooks.

Overall, the dissertation demonstrated the capability of homogenization

in predicting complex stiffness behavior of corrugated sandwich beams. The developed approach excels in conditions where well-known analytical buckling equations and conventional beam theories fall out of their validity range. It was shown that a nonlinear model for lattice-type materials such as corrugated core sandwich beams must contain scale parameters and nonlinear sub-scale information, which can be condensed into effective stiffnesses.

References

- [1] J. Aboudi, S. Arnold, and B. Bednarczyk. *Micromechanics of Composite Materials*. Butterworth-Heinemann, 2012.
- [2] Z. Aboura, N. Talbi, S. Allaoui, and M. L. Benzeggagh. Elastic behavior of corrugated cardboard: Experiments and modeling. *Composite Structures*, 63(1):53–62, 2004.
- [3] International Energy Agency. *World Energy Outlook 2018*. 2018.
- [4] H. G. Allen. *Analysis and Design of Structural Sandwich Panels*. Pergamon Press, 1969.
- [5] W. B. Anderson and R. S. Lakes. Size effects due to cosserat elasticity and surface damage in closed-cell polymethacrylimide foam. *Journal of Materials Science*, 29(24):6413–6419, 1994.
- [6] J. Andrić and V. Žanić. The global structural response model for multi-deck ships in concept design phase. *Ocean Engineering*, 37(8-9):688–704, 2010.
- [7] A. Arbind and J.N. Reddy. Nonlinear analysis of functionally graded microstructure-dependent beams. *Composite Structures*, 98:272–281, 2013.
- [8] J. D. Aristizabal-Ochoa. Second-order slope–deflection equations for imperfect beam–column structures with semi-rigid connections. *Engineering Structures*, 32(8):2440–2454, 2010.
- [9] M. Asghari, M. H. Kahrobaian, and M. T. Ahmadian. A nonlinear Timoshenko beam formulation based on the modified couple stress theory. *International Journal of Engineering Science*, 48(12):1749–1761, 2010.
- [10] M. Asghari, M. Rahaeifard, M. H. Kahrobaian, and M. T. Ahmadian. The modified couple stress functionally graded Timoshenko beam formulation. *Materials & Design*, 32(3):1435–1443, 2011.
- [11] M. F. Ashby. *Materials Selection in Mechanical Design*. Butterworth-Heinemann, 2016.
- [12] Z. P. Bazant and L. Cedolin. *Stability of structures*. World Scientific, 2010.
- [13] Z. P. Bazant and M. Christensen. Analogy between micropolar continuum and grid frameworks under initial stress. *International Journal of Solids and Structures*, 8:327–346, 1972.

- [14] E. Beneus and I. Koc. Innovative road bridges with steel sandwich decks: Optimization of the structural performance of a laser welded steel sandwich deck. Master's thesis, Chalmers University of Technology, Sweden, 2014.
- [15] R. Biagi and H. Bart-Smith. Imperfection sensitivity of pyramidal core sandwich structures. *International Journal of Solids and Structures*, 44(14-15):4690–4706, 2007.
- [16] R. Biagi and H. Bart-Smith. In-plane column response of metallic corrugated core sandwich panels. *International Journal of Solids and Structures*, 49(26):3901–3914, 2012.
- [17] H. Bin, Y. Bo, X. Yu, C. Chang-Qing, Z. Qian-Cheng, and L. Tian Jian. Foam filling radically enhances transverse shear response of corrugated sandwich plates. *Materials & Design*, 77:132–141, 2015.
- [18] R. K. Boorle and P. K. Mallick. Global bending response of composite sandwich plates with corrugated core: Part I: Effect of geometric parameters. *Composite Structures*, 141:375–388, 2016.
- [19] M. Brambilla and A. Martino. Research for TRAN Committee - Maritime Transport System: Focus on Ferries. Technical report, 2016.
- [20] British Petroleum. Bp energy outlook 2019 edition. Technical report, 2019.
- [21] N. Buannic, P. Cartraud, and T. Quesnel. Homogenization of corrugated core sandwich panels. *Composite Structures*, 59(3):299–312, 2003.
- [22] W. S. Burton and A.K. Noor. Assessment of computational models for sandwich panels and shells. *Computer Methods in Applied Mechanics and Engineering*, 124(1-2):125–151, 1995.
- [23] E. Byklum. *Ultimate strength analysis of stiffened steel and aluminium panels using semi-analytical methods*. PhD thesis, Norwegian University of Science and Technology, 2002.
- [24] E. Byklum and J. Amdahl. A simplified method for elastic large deflection analysis of plates and stiffened panels due to local buckling. *Thin-Walled Structures*, 40(11):925–953, 2002.
- [25] E. Byklum, E. Steen, and J. Amdahl. A semi-analytical model for global buckling and postbuckling analysis of stiffened panels. *Thin-Walled Structures*, 42(5):701–717, 2004.
- [26] E. Carrera and S. Brischetto. A survey with numerical assessment of classical and refined theories for the analysis of sandwich plates. *Applied Mechanics Reviews*, 62(1), 2008.
- [27] L. Chapman. Transport and climate change: a review. *Journal of Transport Geography*, 2007.
- [28] W.F. Chen and E.M Lui. *Handbook of structural engineering*. CRC Press, 2005.
- [29] B. G. Compton and J. A. Lewis. 3D-printing of lightweight cellular composites. *Advanced Materials*, 26(34):5930–5935, 2014.
- [30] SANDWICH consortium. Synthesis report test results tno.all.deliverable4.4- v1 03-03-03. Technical report, 2003.

- [31] R. D. Cook, D. S. Malkus, and M. E. Plesha. *Concepts and applications of finite element analysis*. John Wiley & Sons, 1989.
- [32] E. Cosserat and F. Cosserat. *Théorie des corps déformables (engl. translation by D. Delphenich 2007)*. 1909.
- [33] F. Côté, R. Biagi, H. Bart-Smith, and V. S. Deshpande. Structural response of pyramidal core sandwich columns. *International Journal of Solids and Structures*, 44(10), 2007.
- [34] F. Côté, V. S. Deshpande, N. A. Fleck, and A. G. Evans. The compressive and shear responses of corrugated and diamond lattice materials. *International Journal of Solids and Structures*, 43(20):6220–6242, 2006.
- [35] M. A. Crisfield. A fast incremental/iterative solution procedure that handles "snap-through". *Computers and Structures*, 13(1-3):55–62, 1981.
- [36] R. de Borst, M. A. Crisfield, J. J. C. Remmers, and C. V. Verhoosel. *Non-Linear Finite Element Analysis of Solids and Structures: Second Edition*. 2012.
- [37] E. A. De Souza Neto and Y. T. Feng. On the determination of the path direction for arc-length methods in the presence of bifurcations and 'snap-backs'. *Computer Methods in Applied Mechanics and Engineering*, 179(1-2):81–89, 1999.
- [38] A. M. Dehrouyeh-Semnani and A. Bahrami. On size-dependent timoshenko beam element based on modified couple stress theory. *International Journal of Engineering Science*, 107:134–148, 2016.
- [39] V. S. Deshpande and N. A. Fleck. Collapse of truss core sandwich beams in 3-point bending. *International Journal of Solids and Structures*, 38(36-37), 2001.
- [40] DNV-GL. Next generation energy management. Technical report, 2014.
- [41] S. Ehlers, K. Tabri, J. Romanoff, and P. Varsta. Numerical and experimental investigation on the collision resistance of the X-core structure. *Ships and Offshore Structures*, 7(1):21–29, 2012.
- [42] F. Engesser. Ueber die knickfestigkeit gerader stäbe. *Zeitschrift für Architektur und Ingenieurwesen*, 35(4), 1889.
- [43] A. Cemal. Eringen. Linear Theory of Micropolar Elasticity. *Journal of Mathematics and Mechanics*, 15(6):909–923, 1966.
- [44] Eurocode. *EN 1990:2002 - Basis of structural design*. 2002.
- [45] FCCA. 2018 cruise industry overview. Technical report, 2018.
- [46] Y. T. Feng, D. Perić, and D. R.J. Owen. Determination of travel directions in path-following methods. *Mathematical and Computer Modelling*, 1995.
- [47] F. Feyel. A multilevel finite element method (FE2) to describe the response of highly non-linear structures using generalized continua. *Computer Methods in Applied Mechanics and Engineering*, 192(28-30):3233–3244, 2003.

- [48] F. Feyel. Multiscale FE2 elastoviscoplastic analysis of composite structures. *Computational Materials Science*, 16(1-4):344–354, 2003.
- [49] F. Feyel and J. L. Chaboche. FE2 multiscale approach for modelling the elastoviscoplastic behaviour of long fibre SiC/Ti composite materials. *Computer Methods in Applied Mechanics and Engineering*, 183(3-4):309–330, 2000.
- [50] N. A. Fleck, V. S. Deshpande, and M. F. Ashby. Micro-architected materials: past, present and future. *Proceedings of the Royal Society A*, 466:2495–2516, 2010.
- [51] D. Frank, J. Romanoff, and H. Remes. Fatigue strength assessment of laser stake-welded web-core steel sandwich panels. *Fatigue and Fracture of Engineering Materials and Structures*, 36(8):724–737, 2013.
- [52] Y. Frostig and M. Baruch. Bending of sandwich beams with transversely flexible core. *AIAA Journal*, 28(3):523–531, 1990.
- [53] T. C. Fung, K. H. Tan, and T. S. Lok. Elastic Constants for Z-Core Sandwich Panels. *Journal of Structural Engineering*, 120(10):3046–3055, 1994.
- [54] T. C. Fung, K. H. Tan, and T. S. Lok. Shear stiffness DQy for C-Core sandwich panels. *Journal of Structural Engineering*, 122(8):958–966, 1996.
- [55] M. G. D. Geers, V. G. Kouznetsova, and W. A. M. Brekelmans. Multi-scale computational homogenization: Trends and challenges. *Journal of Computational and Applied Mathematics*, 234(7):2175–2182, 2010.
- [56] B. R. Goncalves, J. Jelovica, and J. Romanoff. A homogenization method for geometric nonlinear analysis of sandwich structures with initial imperfections. *International Journal of Solids and Structures*, 87:194–205, 2016.
- [57] B. R. Goncalves, A. T. Karttunen, and J. Romanoff. A nonlinear couple stress model for periodic sandwich beams. *Composite Structures*, 212(20):586–597, 2019.
- [58] B. R. Goncalves, A. T. Karttunen, J. Romanoff, and J. N. Reddy. Buckling and free vibration of shear-flexible sandwich beams using a couple-stress-based finite element. *Composite Structures*, 165:233–241, 2017.
- [59] B. R. Goncalves and J. Romanoff. Size-dependent modelling of elastic sandwich beams with prismatic cores. *International Journal of Solids and Structures*, 136-137:28–37, 2018.
- [60] S. Gu, T. J. Lu, and A. G. Evans. On the design of two-dimensional cellular metals for combined heat dissipation and structural load capacity. *International Journal of Heat and Mass Transfer*, 44(11):2163–2175, 2001.
- [61] Z. Guangrong (editor). Ship energy efficiency technologies - now and the future. Technical report, 2017.
- [62] A. R. Hadjesfandiari and G. F. Dargush. Couple stress theory for solids. *International Journal of Solids and Structures*, 48(18):2496–2510, 2011.
- [63] A. R. Hadjesfandiari and G. F. Dargush. Evolution of generalized couple-stress continuum theories : a critical analysis. *arXiv preprint arXiv*, 2014.

- [64] L. He, Y.-S. Cheng, and J. Liu. Precise bending stress analysis of corrugated-core, honeycomb-core and X-core sandwich panels. *Composite Structures*, 94(5):1656–1668, 2012.
- [65] A. S. Herrmann, P. C. Zahlen, and I. Zuardy. Sandwich Structures Technology in Commercial Aviation. In *Sandwich Structures 7: Advancing with Sandwich Structures and Materials*, pages 13–26. Springer Netherlands, 2005.
- [66] R. Hill. Elastic properties of reinforced solids: Some theoretical principles. *Journal of the Mechanics and Physics of Solids*, 11(5):357–372, 1963.
- [67] R. Hill. The essential structure of constitutive laws for metal composites and polycrystals. *Journal of the Mechanics and Physics of Solids*, 15(2):79–95, 1967.
- [68] N. J. Hoff. The Buckling of Sandwich-Type Panels. *Journal of the Aeronautical Sciences*, 3:285–297, 1945.
- [69] J. Hohe and W. Becker. Effective stress-strain relations for two-dimensional cellular sandwich cores: Homogenization, material models, and properties. *Applied Mechanics Reviews*, 55(1):61–87, 2002.
- [70] S. J. Hollister and N. Kikuchi. A comparison of homogenization and standard mechanics analyses for periodic porous composites. *Computational Mechanics*, 10:73–95, 1992.
- [71] Z. Hou, X. Tian, J. Zhang, and D. Li. 3D printed continuous fibre reinforced composite corrugated structure. *Composite Structures*, 184:1005–1010, 2018.
- [72] O. F. Hughes, J. K. Paik, and B. Dominique. *Ship Structural Analysis and Design*. The Society of Naval Architects and Marine Engineers, 2010.
- [73] International Energy Agency. Energy efficiency indicators, Highlights. 2018.
- [74] J. Jelovica. *Global buckling response of web-core steel sandwich plates influenced by general corrosion*. PhD thesis, Aalto University, 2014.
- [75] J. Jelovica and J. Romanoff. Load-carrying behaviour of web-core sandwich plates in compression. *Thin-Walled Structures*, 73:264–272, 2013.
- [76] J. Jelovica and J. Romanoff. Buckling of sandwich panels with transversely flexible core: Correction of the equivalent single-layer model using thick-faces effect. *Journal of Sandwich Structures & Materials*, 22(5):1612–1634, 2018.
- [77] H. S. Ji, W. Song, and Z. J. Ma. Design, test and field application of a GFRP corrugated-core sandwich bridge. *Engineering Structures*, 32(9):2814–2824, 2010.
- [78] F. Jin, H. Chen, L. Zhao, H. Fan, C. Cai, and N. Kuang. Failure mechanisms of sandwich composites with orthotropic integrated woven corrugated cores: Experiments. *Composite Structures*, 98:53–58, 2013.
- [79] Ł. Kaczmarczyk, C. J. Pearce, and N. Bićanić. Scale transition and enforcement of RVE boundary conditions in second-order computational homogenization. *International Journal for Numerical Methods in Engineering*, 74(3):506–522, 2008.

- [80] P. Kanouté, D. P. Boso, J. L. Chaboche, and B. A. Schrefler. Multiscale methods for composites: A review. *Archives of Computational Methods in Engineering*, 16:31–75, 2009.
- [81] T. Kant and K. Swaminathan. Analytical solutions for free vibration of laminated composite and sandwich plates based on a higher-order refined theory. *Composite Structures*, 53(1):73–85, 2001.
- [82] A. T. Karttunen, M. Kanerva, D. Frank, J. Romanoff, H. Remes, J. Jelovica, S. Bossuyt, and E. Sarlin. Fatigue strength of laser-welded foam-filled steel sandwich beams. *Materials & Design*, 115:64–72, 2017.
- [83] A. T. Karttunen, J. N. Reddy, and J. Romanoff. Micropolar modeling approach for periodic sandwich beams. *Composite Structures*, 185:656–664, 2018.
- [84] A. T. Karttunen, J. N. Reddy, and J. Romanoff. Two-scale constitutive modeling of a lattice core sandwich beam. *Composites Part B: Engineering*, 160:66–75, 2019.
- [85] A. T. Karttunen, J. Romanoff, and J.N. Reddy. Exact microstructure-dependent Timoshenko beam element. *International Journal of Mechanical Sciences*, 111-112:35–42, 2016.
- [86] A.T. Karttunen, J. N. Reddy, and J. Romanoff. Two-scale micropolar plate model for web-core sandwich panels. *International Journal of Solids and Structures*, 170:82–94, 2019.
- [87] S. Kazemahvazi, D. Tanner, and D. Zenkert. Corrugated all-composite sandwich structures. Part 2: Failure mechanisms and experimental programme. *Composites Science and Technology*, 69(7-8):920–925, 2009.
- [88] S. Kazemahvazi and D. Zenkert. Corrugated all-composite sandwich structures. Part 1: Modeling. *Composites Science and Technology*, 69(7-8):913–919, 2009.
- [89] E. M. Knox, M. J. Cowling, and I. E. Winkle. Adhesively bonded steel corrugated core sandwich construction for marine applications. *Marine Structures*, 11(4-5):185–204, 1998.
- [90] W. T. Koiter. Couple stresses in the theory of elasticity, I and II. *Proceedings of the Koninklijke Nederlandse Akademie van Wetenschappen. Series B. Physical Sciences*, 67:17–44, 1964.
- [91] G. W. Kooistra, V. Deshpande, and H. N. G. Wadley. Hierarchical Corrugated Core Sandwich Panel Concepts. *Journal of Applied Mechanics*, 74(2):259–268, 2007.
- [92] M. Korgesaar, A. Kumiste, and J. Jelovica. Steel sandwich panels optimized for crashworthiness: the X- and Y-core. In *7th International Conference on Thin-walled structures ICTWS 2014*.
- [93] V. Kouznetsova, M. G.D. Geers, and W. A.M. Brekelmans. Multi-scale constitutive modelling of heterogeneous materials with a gradient-enhanced computational homogenization scheme. *International Journal for Numerical Methods in Engineering*, 54(8):1235–1260, 2002.

- [94] V. G. Kouznetsova, M. G. D. Geers, and W. A. M. Brekelmans. Multi-scale second-order computational homogenization of multi-phase materials: A nested finite element solution strategy. *Computer Methods in Applied Mechanics and Engineering*, 2004.
- [95] J. Kozac. Selected problems on application of steel sandwich panels to marine structures. *Polish Maritime Research*, 4:9–15, 2009.
- [96] I. Kreja. A literature review on computational models for laminated composite and sandwich panels. *Central European Journal of Engineering*, 1:59–80, 2011.
- [97] P. Kujala and A. Klanac. Steel sandwich panels in marine applications. *Brodogradnja*, 56(4):305–314, 2005.
- [98] R. S. Kumar and D. L. McDowell. Generalized continuum modeling of 2-D periodic cellular solids. *International Journal of Solids and Structures*, 41(26):7399–7422, 2004.
- [99] D. C. C Lam, F. Yang, A. C. M. Chong, J. Wang, and P. Tong. Experiments and theory in strain gradient elasticity. *Journal of the Mechanics and Physics of Solids*, 51(8):1477–1508, 2003.
- [100] J. Lei, Y. He, S. Guo, Z. Li, and D. Liu. Size-dependent vibration of nickel cantilever microbeams: Experiment and gradient elasticity. *AIP Advances*, 6(10):1477–508, 2009.
- [101] Z. Li, Y. He, J. Lei, S. Guo, D. Liu, and L. Wang. A standard experimental method for determining the material length scale based on modified couple stress theory. *International Journal of Mechanical Sciences*, 141:198–205, 2018.
- [102] Z. Li, Y. He, J. Lei, S. Han, S. Guo, and D. Liu. Experimental investigation on size-dependent higher-mode vibration of cantilever microbeams. *Microsystem Technologies*, 25:3005–3015, 2019.
- [103] C. C. Liang, M. F. Yang, and P. W. Wu. Optimum design of metallic corrugated core sandwich panels subjected to blast loads. *Ocean Engineering*, 28(7):825–861, 2001.
- [104] C. Libove and S. B. Batdorf. General small-deflection theory for flat sandwich plates. NACA Technical Note 1526. Technical report, NASA, 1948.
- [105] C. Libove and R.E. Hubka. Elastic constants for corrugated-core sandwich plates. Technical report, NACA, 1951.
- [106] C. Liebold and W. H. Müller. Comparison of gradient elasticity models for the bending of micromaterials. *Computational Materials Science*, 116:52–61, 2016.
- [107] H. Lindstad and G. S. Eskeland. Low carbon maritime transport: How speed, size and slenderness amounts to substantial capital energy substitution. *Transportation Research Part D: Transport and Environment*, 41:244–256, 2015.
- [108] S. Liu and W. Su. Effective couple-stress continuum model of cellular solids and size effects analysis. *International Journal of Solids and Structures*, 46(14-15):2787–2799, 2009.

- [109] T.-S. Lok and Q.-H. Cheng. Elastic stiffness properties and behavior of truss-core sandwich panel. *Journal of Structural Engineering*, 126(5):552–559, 2000.
- [110] T. J. Lu, J. W. Hutchinson, and A. G. Evans. Optimal design of a flexural actuator. *Journal of the Mechanics and Physics of Solids*, 49(9):2071–2093, 2001.
- [111] H. M. Ma, X-L Gao, and J. N. Reddy. A microstructure-dependent Timoshenko beam model based on a modified couple stress theory. *Journal of the Mechanics and Physics of Solids*, 56(12):3379–3391, 2008.
- [112] J. Mandel. Plasticité classique et viscoplasticité: Course held at the centre international des sciences mecaniques (CISM), udine, 1971.
- [113] International maritime organization. Third IMO Greenhouse Gas Study 2014. Technical report, 2015.
- [114] H. Matsunaga. Assessment of a global higher-order deformation theory for laminated composite and sandwich plates. *Composite Structures*, 56(3):279–291, 2002.
- [115] R. D. Mindlin and H. F. Tiersten. Effects of couple-stresses in linear elasticity. *Archive for Rational Mechanics and Analysis*, 11:415–448, 1962.
- [116] R.D. Mindlin. Second gradient of strain and surface-tension in linear elasticity. *International Journal of Solids and Structures*, 1(4):417–438, 1965.
- [117] G.R. Monforton and T.S. Wu. Matrix Analysis of Semi-Rigid Connected Frames. *Journal of the Structural Division*, 89(6):13–24, 1963.
- [118] A. P. Mouritz, E. Gellert, P. Burchill, and K. Challis. Review of advanced composite structures for naval ships and submarines. *Composite Structures*, 53(1):21–42, 2001.
- [119] H. Naar, P. Kujala, B. C. Simonsen, and H. Ludolph. Comparison of the crashworthiness of various bottom and side structures. *Marine Structures*, 15(4-5):443–460, 2002.
- [120] P. Nampally, A. T. Karttunen, and J. N. Reddy. Nonlinear finite element analysis of lattice core sandwich beams. *European Journal of Mechanics-A/Solids*, 74:431–439, 1996.
- [121] N.M. Newmark. A simple approximate formula for effective end-fixity of crolumns. *Journal of the Aeronautical Sciences*, 16(2), 1949.
- [122] V.P. Nguyen, M. Stroeven, and L.J. Sluys. Multiscale continuous and discontinuous modeling of heterogeneous materials: a review on recent developments. *Journal of Multiscale Modelling*, 3(4):229–270, 2012.
- [123] P. Nilsson. *Laser-welded corrugated core steel sandwich bridge decks*. PhD thesis, Chalmers University of Technology, 2020.
- [124] P. Nilsson, M. Al-Emrani, and S. R. Atashipour. Transverse shear stiffness of corrugated core steel sandwich panels with dual weld lines. *Thin-Walled Structures*, 117:98–112, 2017.

- [125] A. K. Noor. Continuum modeling for repetitive lattice structures. *Applied Mechanics Reviews*, 41(7):285–296, 1988.
- [126] A. K. Noor, W. S. Burton, and C. W. Bert. Computational Models for Sandwich Panels and Shells. *Applied Mechanics Reviews*, 49(3):155–199, 1996.
- [127] A. K. Noor and M. P. Nemeth. Micropolar beam models for lattice grids with rigid joints. *Computer Methods in Applied Mechanics and Engineering*, 21(2):249–263, 1980.
- [128] A. K. Noor and W. C. Russell. Anisotropic continuum models for beamlike lattice trusses. *Computer Methods in Applied Mechanics and Engineering*, 57(3):257–277, 1986.
- [129] T. M. Nordstrand and L. A. Carlsson. Evaluation of transverse shear stiffness of structural core sandwich plates. *Composite Structures*, 37(2):145–153, 1997.
- [130] C. Norris. *Spot Welded Corrugated-core Steel Sandwich Panels Subjected to Lateral Loading*. PhD thesis, University of Manchester, 1987.
- [131] American Bureau of Shipping. Ship energy efficiency measures, status and guidance. Technical report, 2013.
- [132] J.K. Paik and A.K. Thayamballi. *Ultimate limit state design of steel-plated structures*. John Wiley & Sons, 2003.
- [133] S. K. Park and X.-L. Gao. Bernoulli-euler beam model based on a modified couple stress theory. *Journal of Micromechanics and Microengineering*, 16:2355–2359, 2006.
- [134] S. K. Park and X.-L. Gao. Micromechanical modeling of honeycomb structures based on a modified couple stress theory. *Mechanics of Advanced Materials and Structures*, 15(8):574–593, 2008.
- [135] F. Penta. Buckling analysis of periodic vierendeel beams by a micro-polar homogenized model. *Acta Mechanica*, 231(6), 2020.
- [136] S. Percival, D. Hendrix, and F. Noblesse. Hydrodynamic optimization of ship hull forms. *Applied Ocean Research*, 23(6):337–355, 2001.
- [137] D. Peri, M. Rossetti, and E. Campana. Design Optimization of Ship Hulls via CFD Techniques. *Journal of Ship Research*, 45:140–149, 2001.
- [138] British Petroleum. Statistical Review of World Energy. Technical report, 2018.
- [139] F. J. Plantema. *Sandwich construction: the bending and buckling of sandwich beams, plates and shells*. Wiley, 1966.
- [140] T. Rabczuk, J. Y. Kim, E. Samaniego, and T. Belytschko. Homogenization of sandwich structures. *International Journal for Numerical Methods in Engineering*, 61:1009–1027, 2004.
- [141] J. N. Reddy. A Simple Higher-Order Theory for Laminated Composite Plates. *Journal of Applied Mechanics*, 51(4), 1984.

- [142] J N Reddy. *Mechanics of laminated composite plates and shells: theory and analysis*. 2003.
- [143] J. N. Reddy. Microstructure-dependent couple stress theories of functionally graded beams. *Journal of the Mechanics and Physics of Solids*, 59(11):2382–2399, 2011.
- [144] J.N. Reddy. *An Introduction to Nonlinear Finite Element Analysis: with applications to heat transfer, fluid mechanics, and solid mechanics*. Oxford University Press, 2015.
- [145] J. Romanoff, A. T. Karttunen, P. Varsta, H. Remes, and B. R. Goncalves. A review on non-classical continuum mechanics with applications in marine engineering. *Mechanics of Advanced Materials and Structures*, 27(13), 2020.
- [146] J. Romanoff, A. Laakso, and P. Varsta. Improving the shear properties of web-core sandwich structures using filling material. In *Analysis and Design of Marine Structures*, pages 133–138. Taylor & Francis, 2009.
- [147] J. Romanoff and J. N. Reddy. Experimental validation of the modified couple stress Timoshenko beam theory for web-core sandwich panels. *Composite Structures*, 111:130–137, 2014.
- [148] J. Romanoff, J.N. Reddy, and J. Jelovica. Using non-local timoshenko beam theories for prediction of micro- and macro-structural responses. *Composite Structures*, 156:410–420, 2016.
- [149] J. Romanoff, H. Remes, G. Socha, M. Jutila, and P. Varsta. The stiffness of laser stake welded T-joints in web-core sandwich structures. *Thin Walled Structures*, 45(4):453–462, 2007.
- [150] J. Romanoff and P. Varsta. Bending response of web-core sandwich plates. *Composite Structures*, 81(2):292–302, 2007.
- [151] J. Romanoff and P. Varsta. Stress analysis of homogenized web-core sandwich beams. *Composite Structures*, 79(3):411–422, 2007.
- [152] V. Rubino, V. S. Deshpande, and N. A. Fleck. The collapse response of sandwich beams with a Y-frame core subjected to distributed and local loading. *International Journal of Mechanical Sciences*, 50(2):233–246, 2008.
- [153] M. Ruzzene. Vibration and sound radiation of sandwich beams with honeycomb truss core. *Journal of Sound and Vibration*, 277:741–763, 2004.
- [154] Dassault Systèmes Simulia. ABAQUS 6.14 Documentation, 2014.
- [155] A.R. Srinivasa and J. N. Reddy. An Overview of Theories of Continuum Mechanics With Nonlocal Elastic Response and a General Framework for Conservative and Dissipative Systems. *Applied Mechanics Reviews*, 69(3), 2017.
- [156] L. St-Pierre, V.S. Deshpande, and N.A. Fleck. The low velocity impact response of sandwich beams with a corrugated core or a Y-frame core. *Composite Structures*, 91:71–80, 2015.
- [157] J Stamper. Time is Energy. *The Aeronautical Journal*, 79(772):169–178, 1975.

- [158] M. Stein and J. Mayers. Compressive buckling of simply supported curved plates and cylinders of sandwich construction. Technical report, NACA, 1952.
- [159] P. Steinmann. A micropolar theory of finite deformation and finite rotation multiplicative elastoplasticity. *International Journal of Solids and Structures*, 31(8):1063–1084, 1994.
- [160] C.T. Sun and R.S. Vaidya. Prediction of composite properties from a representative volume element. *Composites Science and Technology*, 56(2):171–179, 1996.
- [161] D.J. Sypeck. Cellular truss core sandwich structures. *Applied Composite Materials*, 12:229–246, 2005.
- [162] C. Tang and G. Alici. Evaluation of length-scale effects for mechanical behaviour of micro- and nanocantilevers: I. experimental determination of length-scale factors. *Journal of Physics D: Applied Physics*, 44(33), 2011.
- [163] C. Tang and G. Alici. Evaluation of length-scale effects for mechanical behaviour of micro- and nanocantilevers: II. experimental verification of deflection models using atomic force microscopy. *Journal of Physics D: Applied Physics*, 44(33), 2011.
- [164] T.R. Tauchert, T.Y. Chang, and A.C. Eringen. A lattice model for composite materials. Technical report, NASA, 1969.
- [165] The World Bank. Co2 emissions, 2019. data retrieved from World Development Indicators, <https://data.worldbank.org/indicator/EN.ATM.CO2E.KT>.
- [166] S. Timoshenko and J. Gere. *Theory of elastic stability*. McGraw-Hill, 1985.
- [167] R. A. Toupin. Theories of elasticity with couple-stress. *Archive for Rational Mechanics and Analysis*, 17(2):85–112, 1964.
- [168] M. Trancossi. What price of speed? A critical revision through constructal optimization of transport modes. *International Journal of Energy and Environmental Engineering*, 7(4):425–448, 2016.
- [169] UNCTAD. *UNCTAD Handbook of Statistics 2018*. 2018.
- [170] U.S. Energy Information Administration. International Energy Outlook 2017. 2017.
- [171] L. Valdevit, J. W. Hutchinson, and A. G. Evans. Structurally optimized sandwich panels with prismatic cores. *International Journal of Solids and Structures*, 41(18-19):5105–5124, 2004.
- [172] Det Norske Veritas. Extra high strength steel material NV47 for hull structural application in container ships. Technical report, 2011.
- [173] J. Vinson. *The Behavior of Sandwich Structures of Isotropic and Composite Materials*. Routledge, 1999.
- [174] H. N G Wadley, K. P. Dharmasena, M. R. O’Masta, and J. J. Wetzel. Impact response of aluminum corrugated core sandwich panels. *International Journal of Impact Engineering*, 62:114–128, 2013.

References

- [175] H.N.G. Wadley and D. Queheillalt. Thermal applications of cellular lattice structures. In *Materials Science Forum (5th International Conference on the Processing and Manufacturing of Advanced Materials – THERMEC'2006)*, pages 242–247. Trans Tech Publications, 2007.
- [176] R. D. Wood and O. C. Zienkiewicz. Geometrically nonlinear finite element analysis of beams, frames, arches and axisymmetric shells. *Comput. Struct.*, 7(6):725–735, 1977.
- [177] F. Yang, A. C. M. Chong, D. C. C. Lam, and P. Tong. Couple stress based strain gradient theory for elasticity. *International Journal of Solids and Structures*, 39(10):2731–2743, 2002.
- [178] T. Yokozeki, S. Takeda, T. Ogasawara, and T. Ishikawa. Mechanical properties of corrugated composites for candidate materials of flexible wing structures. *Composites Part A: Applied Science and Manufacturing*, 37(10):1578–1586, 2006.
- [179] D. Zenkert. *An introduction to sandwich construction*. Emas, 1995.
- [180] G. Zhang, B. Wang, L. Ma, L. Wu, S. Pan, and J. Yang. Energy absorption and low velocity impact response of polyurethane foam filled pyramidal lattice core sandwich panels. *Composite Structures*, 108:304–310, 2014.
- [181] X. Zhenyu and J. W. Hutchinson. Preliminary assessment of sandwich plates subject to blast loads. *International Journal of Mechanical Sciences*, 45(4), 2003.

A. Finite element definitions

A.1 Lagrangian linear and Hermitian cubic polynomials

The interpolation polynomials utilized in the finite element model of Section 3.6 can be written [144]

$$\psi_1 = 1 - \frac{x_e}{l_e}, \quad \psi_2 = \frac{x_e}{l_e} \quad (\text{A.1a})$$

$$\varphi_1 = 1 - 3\left(\frac{x_e}{l_e}\right)^2 + 2\left(\frac{x_e}{l_e}\right)^3, \quad \varphi_2 = -x_e\left(1 - \frac{x_e}{l_e}\right)^2 \quad (\text{A.1b})$$

$$\varphi_3 = 3\left(\frac{x_e}{l_e}\right)^2 - 2\left(\frac{x_e}{l_e}\right)^3, \quad \varphi_4 = -x_e\left[\left(\frac{x_e}{l_e}\right)^2 - \frac{x_e}{l_e}\right]$$

with x_e referring to the elemental local coordinate system and l_e denoting the element length.

A.2 Strain-displacement interpolation matrices for the present model

The strain-displacement matrices utilized in the sandwich model herein shown are given by

$$\mathbf{B} = \begin{bmatrix} \psi'_1 & 0 & 0 & 0 & \psi'_2 & 0 & 0 & 0 \\ 0 & \psi'_1 & 0 & 0 & 0 & \psi'_2 & 0 & 0 \\ 0 & \psi_1 & \varphi'_1 & \varphi'_2 & 0 & \psi_2 & \varphi'_3 & \varphi'_4 \\ 0 & 0 & -\varphi''_1 & -\varphi''_2 & 0 & 0 & -\varphi''_3 & -\varphi''_4 \end{bmatrix} \quad (\text{A.2})$$

$$\mathbf{B}_\sigma = \begin{bmatrix} 0 & 0 & \varphi'_1 & \varphi'_2 & 0 & 0 & \varphi'_3 & \varphi'_4 \\ 0 & 0 & 0 & 0 & 0 & 0 & 0 & 0 \\ 0 & 0 & 0 & 0 & 0 & 0 & 0 & 0 \\ 0 & 0 & 0 & 0 & 0 & 0 & 0 & 0 \end{bmatrix} \quad (\text{A.3})$$

with the prime (') denoting differentiation with respect to x .

A.3 Transformation matrix for the present model

The local-to-global transformation matrix for the couple stress-based model is given by

$$\hat{\mathbf{T}} = \begin{bmatrix} \cos \alpha^e & 0 & \sin \alpha^e & 0 & 0 & 0 & 0 & 0 \\ 0 & 1 & 0 & 0 & 0 & 0 & 0 & 0 \\ -\sin \alpha^e & 0 & \cos \alpha^e & 0 & 0 & 0 & 0 & 0 \\ 0 & 0 & 0 & 1 & 0 & 0 & 0 & 0 \\ 0 & 0 & 0 & 0 & \cos \alpha^e & 0 & \sin \alpha^e & 0 \\ 0 & 0 & 0 & 0 & 0 & 1 & 0 & 0 \\ 0 & 0 & 0 & 0 & -\sin \alpha^e & 0 & \cos \alpha^e & 0 \\ 0 & 0 & 0 & 0 & 0 & 0 & 0 & 1 \end{bmatrix} \quad (\text{A.4})$$

where α^e is the angle to which the finite element is rotated with respect to the global horizontal axis.

A.4 Linear stiffness matrix

The symmetric half ($K_{ji} = K_{ij}$) of the linearized couple stress stiffness matrix for one-scale problems is given in component form as follows

$$\begin{aligned} K_{11}^e &= \int_{x_a}^{x_b} A \frac{\partial \psi_1}{\partial x} \frac{\partial \psi_1}{\partial x} dx \\ K_{12}^e &= \int_{x_a}^{x_b} C_1 \frac{\partial \psi_1}{\partial x} \frac{\partial \psi_1}{\partial x} dx \\ K_{13}^e &= - \int_{x_a}^{x_b} C_2 \frac{\partial \psi_1}{\partial x} \frac{\partial^2 \psi_1}{\partial x^2} dx \end{aligned} \quad (\text{A.5})$$

$$K_{14}^e = - \int_{x_a}^{x_b} C_2 \frac{\partial \psi_1}{\partial x} \frac{\partial^2 \varphi_2}{\partial x^2} dx$$

$$K_{15}^e = \int_{x_a}^{x_b} A \frac{\partial \psi_1}{\partial x} \frac{\partial \psi_2}{\partial x} dx$$

$$K_{16}^e = \int_{x_a}^{x_b} C_1 \frac{\partial \psi_1}{\partial x} \frac{\partial \psi_2}{\partial x} dx$$

$$K_{17}^e = - \int_{x_a}^{x_b} C_2 \frac{\partial \psi_1}{\partial x} \frac{\partial^2 \varphi_3}{\partial x^2} dx$$

$$K_{18}^e = - \int_{x_a}^{x_b} C_2 \frac{\partial \psi_1}{\partial x} \frac{\partial^2 \varphi_4}{\partial x^2} dx$$

$$K_{22}^e = \int_{x_a}^{x_b} \left(D \frac{\partial \psi_1}{\partial x} \frac{\partial \psi_1}{\partial x} + D_Q \psi_1 \psi_1 \right) dx$$

$$K_{23}^e = \int_{x_a}^{x_b} \left(D_Q \psi_1 \frac{\partial \varphi_1}{\partial x} - C_3 \frac{\partial \psi_1}{\partial x} \frac{\partial^2 \varphi_1}{\partial x^2} \right) dx$$

$$K_{24}^e = \int_{x_a}^{x_b} \left(D_Q \psi_1 \frac{\partial \varphi_2}{\partial x} - C_3 \frac{\partial \psi_1}{\partial x} \frac{\partial^2 \varphi_2}{\partial x^2} \right) dx$$

$$K_{25}^e = \int_{x_a}^{x_b} C_1 \frac{\partial \psi_1}{\partial x} \frac{\partial \psi_2}{\partial x} dx$$

$$K_{26}^e = \int_{x_a}^{x_b} \left(D \frac{\partial \psi_1}{\partial x} \frac{\partial \psi_2}{\partial x} + D_Q \psi_1 \psi_2 \right) dx$$

$$K_{27}^e = \int_{x_a}^{x_b} \left(D_Q \psi_1 \frac{\partial \varphi_3}{\partial x} - C_3 \frac{\partial \psi_1}{\partial x} \frac{\partial^2 \varphi_3}{\partial x^2} \right) dx$$

$$K_{28}^e = \int_{x_a}^{x_b} \left(D_Q \psi_1 \frac{\partial \varphi_4}{\partial x} - C_3 \frac{\partial \psi_1}{\partial x} \frac{\partial^2 \varphi_4}{\partial x^2} \right) dx$$

$$K_{33}^e = \int_{x_a}^{x_b} \left(D_Q \frac{\partial \varphi_1}{\partial x} \frac{\partial \varphi_1}{\partial x} + S \frac{\partial^2 \varphi_1}{\partial x^2} \frac{\partial^2 \varphi_1}{\partial x^2} \right) dx$$

$$K_{34}^e = \int_{x_a}^{x_b} \left(D_Q \frac{\partial \varphi_1}{\partial x} \frac{\partial \varphi_2}{\partial x} + S \frac{\partial^2 \varphi_1}{\partial x^2} \frac{\partial^2 \varphi_2}{\partial x^2} \right) dx$$

$$K_{35}^e = - \int_{x_a}^{x_b} C_2 \frac{\partial^2 \varphi_1}{\partial x^2} \frac{\partial \psi_2}{\partial x} dx$$

$$K_{36}^e = \int_{x_a}^{x_b} \left(D_Q \psi_2 \frac{\partial \varphi_1}{\partial x} - C_3 \frac{\partial \psi_2}{\partial x} \frac{\partial^2 \varphi_1}{\partial x^2} \right) dx$$

$$K_{37}^e = \int_{x_a}^{x_b} \left(D_Q \frac{\partial \varphi_3}{\partial x} \frac{\partial \varphi_1}{\partial x} + S \frac{\partial^2 \varphi_1}{\partial x^2} \frac{\partial^2 \varphi_3}{\partial x^2} \right) dx$$

$$K_{38}^e = \int_{x_a}^{x_b} \left(D_Q \frac{\partial \varphi_1}{\partial x} \frac{\partial \varphi_4}{\partial x} + S \frac{\partial^2 \varphi_1}{\partial x^2} \frac{\partial^2 \varphi_4}{\partial x^2} \right) dx$$

$$K_{44}^e = \int_{x_a}^{x_b} \left(D_Q \frac{\partial \varphi_2}{\partial x} \frac{\partial \varphi_2}{\partial x} + S \frac{\partial^2 \varphi_2}{\partial x^2} \frac{\partial^2 \varphi_2}{\partial x^2} \right) dx$$

$$K_{45}^e = - \int_{x_a}^{x_b} C_2 \frac{\partial \psi_2}{\partial x} \frac{\partial^2 \varphi_2}{\partial x^2} dx$$

$$K_{46}^e = \int_{x_a}^{x_b} \left(D_Q \psi_2 \frac{\partial \varphi_2}{\partial x} - C_3 \frac{\partial \psi_2}{\partial x} \frac{\partial^2 \varphi_2}{\partial x^2} \right) dx$$

$$K_{47}^e = \int_{x_a}^{x_b} \left(D_Q \frac{\partial \varphi_2}{\partial x} \frac{\partial \varphi_3}{\partial x} + S \frac{\partial^2 \varphi_2}{\partial x^2} \frac{\partial^2 \varphi_3}{\partial x^2} \right) dx$$

$$K_{48}^e = \int_{x_a}^{x_b} \left(D_Q \frac{\partial \varphi_2}{\partial x} \frac{\partial \varphi_4}{\partial x} + S \frac{\partial^2 \varphi_2}{\partial x^2} \frac{\partial^2 \varphi_4}{\partial x^2} \right) dx$$

$$K_{55}^e = \int_{x_a}^{x_b} A \frac{\partial \psi_2}{\partial x} \frac{\partial \psi_2}{\partial x} dx$$

$$K_{56}^e = \int_{x_a}^{x_b} C_1 \frac{\partial \psi_2}{\partial x} \frac{\partial \psi_2}{\partial x} dx$$

$$K_{57}^e = - \int_{x_a}^{x_b} C_2 \frac{\partial \psi_2}{\partial x} \frac{\partial^2 \varphi_3}{\partial x^2} dx$$

$$K_{58}^e = - \int_{x_a}^{x_b} C_2 \frac{\partial \psi_2}{\partial x} \frac{\partial^2 \varphi_4}{\partial x^2} dx$$

$$K_{66}^e = \int_{x_a}^{x_b} \left(D \frac{\partial \psi_2}{\partial x} \frac{\partial \psi_2}{\partial x} + D_Q \psi_2 \psi_2 \right) dx$$

$$K_{67}^e = \int_{x_a}^{x_b} \left(D_Q \psi_2 \frac{\partial \varphi_3}{\partial x} - C_3 \frac{\partial \psi_2}{\partial x} \frac{\partial^2 \varphi_3}{\partial x^2} \right) dx$$

$$K_{68}^e = \int_{x_a}^{x_b} \left(D_Q \psi_2 \frac{\partial \varphi_4}{\partial x} - C_3 \frac{\partial \psi_2}{\partial x} \frac{\partial^2 \varphi_4}{\partial x^2} \right) dx$$

$$K_{77}^e = \int_{x_a}^{x_b} \left(D_Q \frac{\partial \varphi_3}{\partial x} \frac{\partial \varphi_3}{\partial x} + S \frac{\partial^2 \varphi_3}{\partial x^2} \frac{\partial^2 \varphi_3}{\partial x^2} \right) dx$$

$$K_{78}^e = \int_{x_a}^{x_b} \left(D_Q \frac{\partial \varphi_3}{\partial x} \frac{\partial \varphi_4}{\partial x} + S \frac{\partial^2 \varphi_3}{\partial x^2} \frac{\partial^2 \varphi_4}{\partial x^2} \right) dx$$

$$K_{88}^e = \int_{x_a}^{x_b} \left(D_Q \frac{\partial \varphi_4}{\partial x} \frac{\partial \varphi_4}{\partial x} + S \frac{\partial^2 \varphi_4}{\partial x^2} \frac{\partial^2 \varphi_4}{\partial x^2} \right) dx$$

A.5 Nonlinear secant stiffness matrix

The nonlinear secant stiffness matrix elements are presented as follows.

For linear microscale, replace \bar{A} , \bar{C}_1 and \bar{D} with A , C_1 and D .

$$\begin{aligned}
 K_{11}^e &= \int_{x_a}^{x_b} \bar{A} \frac{\partial \psi_1}{\partial x} \frac{\partial \psi_1}{\partial x} dx \\
 K_{12}^e &= \int_{x_a}^{x_b} \bar{C}_1 \frac{\partial \psi_1}{\partial x} \frac{\partial \psi_1}{\partial x} dx \\
 K_{13}^e &= \int_{x_a}^{x_b} \left(\frac{\bar{A}}{2} \frac{\partial w}{\partial x} \frac{\partial \psi_1}{\partial x} \frac{\partial \varphi_1}{\partial x} - C_2 \frac{\partial \psi_1}{\partial x} \frac{\partial^2 \varphi_1}{\partial x^2} \right) dx \\
 K_{14}^e &= \int_{x_a}^{x_b} \left(\frac{\bar{A}}{2} \frac{\partial w}{\partial x} \frac{\partial \psi_1}{\partial x} \frac{\partial \varphi_2}{\partial x} - C_2 \frac{\partial \psi_1}{\partial x} \frac{\partial^2 \varphi_2}{\partial x^2} \right) dx \\
 K_{15}^e &= \int_{x_a}^{x_b} \bar{A} \frac{\partial \psi_1}{\partial x} \frac{\partial \psi_2}{\partial x} dx \\
 K_{16}^e &= \int_{x_a}^{x_b} \bar{C}_1 \frac{\partial \psi_1}{\partial x} \frac{\partial \psi_2}{\partial x} dx \\
 K_{17}^e &= \int_{x_a}^{x_b} \left(\frac{\bar{A}}{2} \frac{\partial w}{\partial x} \frac{\partial \psi_1}{\partial x} \frac{\partial \varphi_3}{\partial x} - C_2 \frac{\partial \psi_1}{\partial x} \frac{\partial^2 \varphi_3}{\partial x^2} \right) dx \\
 K_{18}^e &= \int_{x_a}^{x_b} \left(\frac{\bar{A}}{2} \frac{\partial w}{\partial x} \frac{\partial \psi_1}{\partial x} \frac{\partial \varphi_4}{\partial x} - C_2 \frac{\partial \psi_1}{\partial x} \frac{\partial^2 \varphi_4}{\partial x^2} \right) dx \\
 K_{21}^e &= K_{12}^e \\
 K_{22}^e &= \int_{x_a}^{x_b} \left(\bar{D} \frac{\partial \psi_1}{\partial x} \frac{\partial \psi_1}{\partial x} + D_Q \psi_1 \psi_1 \right) dx \\
 K_{23}^e &= \int_{x_a}^{x_b} \left(\frac{\bar{C}_1}{2} \frac{\partial w}{\partial x} \frac{\partial \psi_1}{\partial x} \frac{\partial \varphi_1}{\partial x} + D_Q \psi_1 \frac{\partial \varphi_1}{\partial x} - C_3 \frac{\partial \psi_1}{\partial x} \frac{\partial^2 \varphi_1}{\partial x^2} \right) dx \\
 K_{24}^e &= \int_{x_a}^{x_b} \left(\frac{\bar{C}_1}{2} \frac{\partial w}{\partial x} \frac{\partial \psi_1}{\partial x} \frac{\partial \varphi_2}{\partial x} + D_Q \psi_1 \frac{\partial \varphi_2}{\partial x} - C_3 \frac{\partial \psi_1}{\partial x} \frac{\partial^2 \varphi_2}{\partial x^2} \right) dx \\
 K_{25}^e &= \int_{x_a}^{x_b} \bar{C}_1 \frac{\partial \psi_1}{\partial x} \frac{\partial \psi_2}{\partial x} dx \\
 K_{26}^e &= \int_{x_a}^{x_b} \left(\bar{D} \frac{\partial \psi_1}{\partial x} \frac{\partial \psi_2}{\partial x} + D_Q \psi_1 \psi_2 \right) dx \\
 K_{27}^e &= \int_{x_a}^{x_b} \left(\frac{\bar{C}_1}{2} \frac{\partial w}{\partial x} \frac{\partial \psi_1}{\partial x} \frac{\partial \varphi_3}{\partial x} + D_Q \psi_1 \frac{\partial \varphi_3}{\partial x} - C_3 \frac{\partial \psi_1}{\partial x} \frac{\partial^2 \varphi_3}{\partial x^2} \right) dx \\
 K_{28}^e &= \int_{x_a}^{x_b} \left(\frac{\bar{C}_1}{2} \frac{\partial w}{\partial x} \frac{\partial \psi_1}{\partial x} \frac{\partial \varphi_4}{\partial x} + D_Q \psi_1 \frac{\partial \varphi_4}{\partial x} - C_3 \frac{\partial \psi_1}{\partial x} \frac{\partial^2 \varphi_4}{\partial x^2} \right) dx
 \end{aligned} \tag{A.6}$$

[illegible]

$$\begin{aligned}
K_{45}^e &= \int_{x_a}^{x_b} \left[\bar{A} \frac{\partial w}{\partial x} \frac{\partial \psi_2}{\partial x} \frac{\partial \varphi_2}{\partial x} - C_2 \frac{\partial \psi_2}{\partial x} \frac{\partial^2 \varphi_2}{\partial x^2} - \bar{B}_1 \frac{\partial \psi_2}{\partial x} \frac{\partial^2 \varphi_2}{\partial x^2} \right] dx \\
K_{46}^e &= \int_{x_a}^{x_b} \left(\bar{C}_1 \frac{\partial w}{\partial x} \frac{\partial \psi_2}{\partial x} \frac{\partial \varphi_2}{\partial x} + D_Q \psi_2 \frac{\partial \varphi_2}{\partial x} - C_3 \frac{\partial \psi_2}{\partial x} \frac{\partial^2 \varphi_2}{\partial x^2} - \bar{B}_2 \frac{\partial \psi_2}{\partial x} \frac{\partial^2 \varphi_2}{\partial x^2} \right) dx \\
K_{47}^e &= \int_{x_a}^{x_b} \left[\frac{\bar{A}}{2} \left(\frac{\partial w}{\partial x} \right)^2 \frac{\partial \varphi_3}{\partial x} \frac{\partial \varphi_2}{\partial x} + D_Q \frac{\partial \varphi_3}{\partial x} \frac{\partial \varphi_2}{\partial x} + S \frac{\partial^2 \varphi_3}{\partial x^2} \frac{\partial^2 \varphi_2}{\partial x^2} \right. \\
&\quad \left. - C_2 \frac{\partial w}{\partial x} \left(\frac{\partial \varphi_2}{\partial x} \frac{\partial^2 \varphi_3}{\partial x^2} + \frac{1}{2} \frac{\partial \varphi_3}{\partial x} \frac{\partial^2 \varphi_2}{\partial x^2} \right) - \frac{\bar{B}_1}{2} \frac{\partial w}{\partial x} \frac{\partial \varphi_3}{\partial x} \frac{\partial^2 \varphi_2}{\partial x^2} \right] dx \\
K_{48}^e &= \int_{x_a}^{x_b} \left[\frac{\bar{A}}{2} \left(\frac{\partial w}{\partial x} \right)^2 \frac{\partial \varphi_4}{\partial x} \frac{\partial \varphi_2}{\partial x} + D_Q \frac{\partial \varphi_4}{\partial x} \frac{\partial \varphi_2}{\partial x} + S \frac{\partial^2 \varphi_4}{\partial x^2} \frac{\partial^2 \varphi_2}{\partial x^2} \right. \\
&\quad \left. - C_2 \frac{\partial w}{\partial x} \left(\frac{\partial \varphi_2}{\partial x} \frac{\partial^2 \varphi_4}{\partial x^2} + \frac{1}{2} \frac{\partial \varphi_4}{\partial x} \frac{\partial^2 \varphi_2}{\partial x^2} \right) - \frac{\bar{B}_1}{2} \frac{\partial w}{\partial x} \frac{\partial \varphi_4}{\partial x} \frac{\partial^2 \varphi_2}{\partial x^2} \right] dx \\
K_{51}^e &= K_{15}^e \\
K_{52}^e &= K_{25}^e \\
K_{53}^e &= \int_{x_a}^{x_b} \left(\frac{\bar{A}}{2} \frac{\partial w}{\partial x} \frac{\partial \psi_2}{\partial x} \frac{\partial \varphi_1}{\partial x} - C_2 \frac{\partial \psi_2}{\partial x} \frac{\partial^2 \varphi_1}{\partial x^2} \right) dx \\
K_{54}^e &= \int_{x_a}^{x_b} \left(\frac{\bar{A}}{2} \frac{\partial w}{\partial x} \frac{\partial \psi_2}{\partial x} \frac{\partial \varphi_2}{\partial x} - C_2 \frac{\partial \psi_2}{\partial x} \frac{\partial^2 \varphi_2}{\partial x^2} \right) dx \\
K_{55}^e &= \int_{x_a}^{x_b} \bar{A} \frac{\partial \psi_2}{\partial x} \frac{\partial \psi_2}{\partial x} dx \\
K_{56}^e &= \int_{x_a}^{x_b} \bar{C}_1 \frac{\partial \psi_2}{\partial x} \frac{\partial \psi_2}{\partial x} dx \\
K_{57}^e &= \int_{x_a}^{x_b} \left(\frac{\bar{A}}{2} \frac{\partial w}{\partial x} \frac{\partial \psi_2}{\partial x} \frac{\partial \varphi_3}{\partial x} - C_2 \frac{\partial \psi_2}{\partial x} \frac{\partial^2 \varphi_3}{\partial x^2} \right) dx \\
K_{58}^e &= \int_{x_a}^{x_b} \left(\frac{\bar{A}}{2} \frac{\partial w}{\partial x} \frac{\partial \psi_2}{\partial x} \frac{\partial \varphi_4}{\partial x} - C_2 \frac{\partial \psi_2}{\partial x} \frac{\partial^2 \varphi_4}{\partial x^2} \right) dx \\
K_{61}^e &= K_{16}^e \\
K_{62}^e &= K_{26}^e \\
K_{63}^e &= \int_{x_a}^{x_b} \left(\frac{\bar{C}_1}{2} \frac{\partial w}{\partial x} \frac{\partial \psi_2}{\partial x} \frac{\partial \varphi_1}{\partial x} + D_Q \psi_2 \frac{\partial \varphi_1}{\partial x} - C_3 \frac{\partial \psi_2}{\partial x} \frac{\partial^2 \varphi_1}{\partial x^2} \right) dx \\
K_{64}^e &= \int_{x_a}^{x_b} \left(\frac{\bar{C}_1}{2} \frac{\partial w}{\partial x} \frac{\partial \psi_2}{\partial x} \frac{\partial \varphi_2}{\partial x} + D_Q \psi_2 \frac{\partial \varphi_2}{\partial x} - C_3 \frac{\partial \psi_2}{\partial x} \frac{\partial^2 \varphi_2}{\partial x^2} \right) dx \\
K_{65}^e &= K_{56}^e \\
K_{66}^e &= \int_{x_a}^{x_b} \left(\bar{D} \frac{\partial \psi_2}{\partial x} \frac{\partial \psi_2}{\partial x} + D_Q \psi_2 \psi_2 \right) dx
\end{aligned}$$

$$\begin{aligned}
K_{84}^e &= \int_{x_a}^{x_b} \left[\frac{\bar{A}}{2} \left(\frac{\partial w}{\partial x} \right)^2 \frac{\partial \varphi_2}{\partial x} \frac{\partial \varphi_4}{\partial x} + D_Q \frac{\partial \varphi_2}{\partial x} \frac{\partial \varphi_4}{\partial x} + S \frac{\partial^2 \varphi_2}{\partial x^2} \frac{\partial^2 \varphi_4}{\partial x^2} \right. \\
&\quad \left. - C_2 \frac{\partial w}{\partial x} \left(\frac{\partial \varphi_4}{\partial x} \frac{\partial^2 \varphi_2}{\partial x^2} + \frac{1}{2} \frac{\partial \varphi_2}{\partial x} \frac{\partial^2 \varphi_4}{\partial x^2} \right) - \frac{\bar{B}_1}{2} \frac{\partial w}{\partial x} \frac{\partial \varphi_2}{\partial x} \frac{\partial^2 \varphi_4}{\partial x^2} \right] dx \\
K_{85}^e &= \int_{x_a}^{x_b} \left(\bar{A} \frac{\partial w}{\partial x} \frac{\partial \psi_2}{\partial x} \frac{\partial \varphi_4}{\partial x} - C_2 \frac{\partial \psi_2}{\partial x} \frac{\partial^2 \varphi_4}{\partial x^2} - \bar{B}_1 \frac{\partial \psi_2}{\partial x} \frac{\partial^2 \varphi_4}{\partial x^2} \right) dx \\
K_{86}^e &= \int_{x_a}^{x_b} \left(\bar{C}_1 \frac{\partial w}{\partial x} \frac{\partial \psi_2}{\partial x} \frac{\partial \varphi_4}{\partial x} + D_Q \psi_2 \frac{\partial \varphi_4}{\partial x} - C_3 \frac{\partial \psi_2}{\partial x} \frac{\partial^2 \varphi_4}{\partial x^2} - \bar{B}_2 \frac{\partial \psi_2}{\partial x} \frac{\partial^2 \varphi_4}{\partial x^2} \right) dx \\
K_{87}^e &= \int_{x_a}^{x_b} \left[\frac{\bar{A}}{2} \left(\frac{\partial w}{\partial x} \right)^2 \frac{\partial \varphi_3}{\partial x} \frac{\partial \varphi_4}{\partial x} + D_Q \frac{\partial \varphi_3}{\partial x} \frac{\partial \varphi_4}{\partial x} + S \frac{\partial^2 \varphi_3}{\partial x^2} \frac{\partial^2 \varphi_4}{\partial x^2} \right. \\
&\quad \left. - C_2 \frac{\partial w}{\partial x} \left(\frac{\partial \varphi_4}{\partial x} \frac{\partial^2 \varphi_3}{\partial x^2} + \frac{1}{2} \frac{\partial \varphi_3}{\partial x} \frac{\partial^2 \varphi_4}{\partial x^2} \right) - \frac{\bar{B}_1}{2} \frac{\partial w}{\partial x} \frac{\partial \varphi_3}{\partial x} \frac{\partial^2 \varphi_4}{\partial x^2} \right] dx \\
K_{88}^e &= \int_{x_a}^{x_b} \left[\frac{\bar{A}}{2} \left(\frac{\partial w}{\partial x} \right)^2 \frac{\partial \varphi_4}{\partial x} \frac{\partial \varphi_4}{\partial x} + D_Q \frac{\partial \varphi_4}{\partial x} \frac{\partial \varphi_4}{\partial x} + S \frac{\partial^2 \varphi_4}{\partial x^2} \frac{\partial^2 \varphi_4}{\partial x^2} \right. \\
&\quad \left. - \frac{3C_2}{2} \frac{\partial w}{\partial x} \frac{\partial \varphi_4}{\partial x} \frac{\partial^2 \varphi_4}{\partial x^2} - \frac{\bar{B}_1}{2} \frac{\partial w}{\partial x} \frac{\partial \varphi_4}{\partial x} \frac{\partial^2 \varphi_4}{\partial x^2} \right] dx
\end{aligned}$$

A.6 Nonlinear tangent stiffness matrix

The nonlinear tangent stiffness matrix elements are presented as follows.

$$T_{11}^e = K_{11}^e \quad (\text{A.7})$$

$$T_{12}^e = K_{12}^e$$

$$T_{13}^e = K_{13}^e + \int_{x_a}^{x_b} \frac{\bar{A}}{2} \frac{\partial w}{\partial x} \frac{\partial \psi_1}{\partial x} \frac{\partial \varphi_1}{\partial x} dx$$

$$T_{14}^e = K_{14}^e + \int_{x_a}^{x_b} \frac{\bar{A}}{2} \frac{\partial w}{\partial x} \frac{\partial \psi_1}{\partial x} \frac{\partial \varphi_2}{\partial x} dx$$

$$T_{15}^e = K_{15}^e$$

$$T_{16}^e = K_{16}^e$$

$$T_{17}^e = K_{17}^e + \int_{x_a}^{x_b} \frac{\bar{A}}{2} \frac{\partial w}{\partial x} \frac{\partial \psi_1}{\partial x} \frac{\partial \varphi_3}{\partial x} dx$$

$$T_{18}^e = K_{18}^e + \int_{x_a}^{x_b} \frac{\bar{A}}{2} \frac{\partial w}{\partial x} \frac{\partial \psi_1}{\partial x} \frac{\partial \varphi_4}{\partial x} dx$$

$$T_{21}^e = K_{21}^e$$

$$T_{22}^e = K_{22}^e$$

$$T_{23}^e = K_{23}^e + \int_{x_a}^{x_b} \frac{\bar{C}_1}{2} \frac{\partial w}{\partial x} \frac{\partial \psi_1}{\partial x} \frac{\partial \varphi_1}{\partial x} dx$$

$$T_{24}^e = K_{24}^e + \int_{x_a}^{x_b} \frac{\bar{C}_1}{2} \frac{\partial w}{\partial x} \frac{\partial \psi_1}{\partial x} \frac{\partial \varphi_2}{\partial x} dx$$

$$T_{25}^e = K_{25}^e$$

$$T_{26}^e = K_{26}^e$$

$$T_{27}^e = K_{27}^e + \int_{x_a}^{x_b} \frac{\bar{C}_1}{2} \frac{\partial w}{\partial x} \frac{\partial \psi_1}{\partial x} \frac{\partial \varphi_3}{\partial x} dx$$

$$T_{28}^e = K_{28}^e + \int_{x_a}^{x_b} \frac{\bar{C}_1}{2} \frac{\partial w}{\partial x} \frac{\partial \psi_1}{\partial x} \frac{\partial \varphi_4}{\partial x} dx$$

$$T_{31}^e = K_{31}^e$$

$$T_{32}^e = K_{32}^e$$

$$T_{33}^e = K_{33}^e + \int_{x_a}^{x_b} \left\{ \bar{A} \left[\frac{\partial u}{\partial x} + \left(\frac{\partial w}{\partial x} \right)^2 \right] \frac{\partial \varphi_1}{\partial x} \frac{\partial \varphi_1}{\partial x} + \bar{C}_1 \frac{\partial \phi}{\partial x} \frac{\partial \varphi_1}{\partial x} \frac{\partial \varphi_1}{\partial x} \right. \\ \left. + (C_2 + \bar{B}_1) \left(\frac{\partial^2 w}{\partial x^2} \frac{\partial \varphi_1}{\partial x} \frac{\partial \varphi_1}{\partial x} + \frac{1}{2} \frac{\partial w}{\partial x} \frac{\partial \varphi_1}{\partial x} \frac{\partial^2 \varphi_1}{\partial x^2} \right) \right\} dx$$

$$T_{34}^e = K_{34}^e + \int_{x_a}^{x_b} \left\{ \bar{A} \left[\frac{\partial u}{\partial x} + \left(\frac{\partial w}{\partial x} \right)^2 \right] \frac{\partial \varphi_1}{\partial x} \frac{\partial \varphi_2}{\partial x} + \bar{C}_1 \frac{\partial \phi}{\partial x} \frac{\partial \varphi_1}{\partial x} \frac{\partial \varphi_2}{\partial x} \right. \\ \left. + (C_2 + \bar{B}_1) \left(\frac{\partial^2 w}{\partial x^2} \frac{\partial \varphi_1}{\partial x} \frac{\partial \varphi_2}{\partial x} + \frac{1}{2} \frac{\partial w}{\partial x} \frac{\partial \varphi_2}{\partial x} \frac{\partial^2 \varphi_1}{\partial x^2} \right) \right\} dx$$

$$T_{35}^e = K_{35}^e$$

$$T_{36}^e = K_{36}^e$$

$$T_{37}^e = K_{37}^e + \int_{x_a}^{x_b} \left\{ \bar{A} \left[\frac{\partial u}{\partial x} + \left(\frac{\partial w}{\partial x} \right)^2 \right] \frac{\partial \varphi_1}{\partial x} \frac{\partial \varphi_3}{\partial x} + \bar{C}_1 \frac{\partial \phi}{\partial x} \frac{\partial \varphi_1}{\partial x} \frac{\partial \varphi_2}{\partial x} \right. \\ \left. + (C_2 + \bar{B}_1) \left(\frac{\partial^2 w}{\partial x^2} \frac{\partial \varphi_1}{\partial x} \frac{\partial \varphi_3}{\partial x} + \frac{1}{2} \frac{\partial w}{\partial x} \frac{\partial \varphi_3}{\partial x} \frac{\partial^2 \varphi_1}{\partial x^2} \right) \right\} dx$$

$$T_{38}^e = K_{38}^e + \int_{x_a}^{x_b} \left\{ \bar{A} \left[\frac{\partial u}{\partial x} + \left(\frac{\partial w}{\partial x} \right)^2 \right] \frac{\partial \varphi_1}{\partial x} \frac{\partial \varphi_4}{\partial x} + \bar{C}_1 \frac{\partial \phi}{\partial x} \frac{\partial \varphi_1}{\partial x} \frac{\partial \varphi_2}{\partial x} \right. \\ \left. + (C_2 + \bar{B}_1) \left(\frac{\partial^2 w}{\partial x^2} \frac{\partial \varphi_1}{\partial x} \frac{\partial \varphi_4}{\partial x} + \frac{1}{2} \frac{\partial w}{\partial x} \frac{\partial \varphi_4}{\partial x} \frac{\partial^2 \varphi_1}{\partial x^2} \right) \right\} dx$$

$$T_{41}^e = K_{41}^e$$

$$T_{42}^e = K_{42}^e$$

$$T_{43}^e = K_{43}^e + \int_{x_a}^{x_b} \left\{ \bar{A} \left[\frac{\partial u}{\partial x} + \left(\frac{\partial w}{\partial x} \right)^2 \right] \frac{\partial \varphi_1}{\partial x} \frac{\partial \varphi_2}{\partial x} + \bar{C}_1 \frac{\partial \phi}{\partial x} \frac{\partial \varphi_1}{\partial x} \frac{\partial \varphi_2}{\partial x} \right. \\ \left. + (C_2 + \bar{B}_1) \left(\frac{\partial^2 w}{\partial x^2} \frac{\partial \varphi_1}{\partial x} \frac{\partial \varphi_2}{\partial x} + \frac{1}{2} \frac{\partial w}{\partial x} \frac{\partial \varphi_1}{\partial x} \frac{\partial^2 \varphi_2}{\partial x^2} \right) \right\} dx$$

$$T_{44}^e = K_{44}^e + \int_{x_a}^{x_b} \left\{ \bar{A} \left[\frac{\partial u}{\partial x} + \left(\frac{\partial w}{\partial x} \right)^2 \right] \frac{\partial \varphi_2}{\partial x} \frac{\partial \varphi_2}{\partial x} + \bar{C}_1 \frac{\partial \phi}{\partial x} \frac{\partial \varphi_2}{\partial x} \frac{\partial \varphi_2}{\partial x} \right. \\ \left. + (C_2 + \bar{B}_1) \left(\frac{\partial^2 w}{\partial x^2} \frac{\partial \varphi_2}{\partial x} \frac{\partial \varphi_2}{\partial x} + \frac{1}{2} \frac{\partial w}{\partial x} \frac{\partial \varphi_2}{\partial x} \frac{\partial^2 \varphi_2}{\partial x^2} \right) \right\} dx$$

$$T_{45}^e = K_{45}^e$$

$$T_{46}^e = K_{46}^e$$

$$T_{47}^e = K_{47}^e + \int_{x_a}^{x_b} \left\{ \bar{A} \left[\frac{\partial u}{\partial x} + \left(\frac{\partial w}{\partial x} \right)^2 \right] \frac{\partial \varphi_3}{\partial x} \frac{\partial \varphi_2}{\partial x} + \bar{C}_1 \frac{\partial \phi}{\partial x} \frac{\partial \varphi_3}{\partial x} \frac{\partial \varphi_2}{\partial x} \right. \\ \left. + (C_2 + \bar{B}_1) \left(\frac{\partial^2 w}{\partial x^2} \frac{\partial \varphi_3}{\partial x} \frac{\partial \varphi_2}{\partial x} + \frac{1}{2} \frac{\partial w}{\partial x} \frac{\partial \varphi_3}{\partial x} \frac{\partial^2 \varphi_2}{\partial x^2} \right) \right\} dx$$

$$T_{48}^e = K_{48}^e + \int_{x_a}^{x_b} \left\{ \bar{A} \left[\frac{\partial u}{\partial x} + \left(\frac{\partial w}{\partial x} \right)^2 \right] \frac{\partial \varphi_4}{\partial x} \frac{\partial \varphi_2}{\partial x} + \bar{C}_1 \frac{\partial \phi}{\partial x} \frac{\partial \varphi_4}{\partial x} \frac{\partial \varphi_2}{\partial x} \right. \\ \left. + (C_2 + \bar{B}_1) \left(\frac{\partial^2 w}{\partial x^2} \frac{\partial \varphi_4}{\partial x} \frac{\partial \varphi_2}{\partial x} + \frac{1}{2} \frac{\partial w}{\partial x} \frac{\partial \varphi_4}{\partial x} \frac{\partial^2 \varphi_2}{\partial x^2} \right) \right\} dx$$

$$T_{51}^e = K_{51}^e$$

$$T_{52}^e = K_{52}^e$$

$$T_{53}^e = K_{53}^e + \int_{x_a}^{x_b} \frac{\bar{A}}{2} \frac{\partial w}{\partial x} \frac{\partial \psi_2}{\partial x} \frac{\partial \varphi_1}{\partial x} dx$$

$$T_{54}^e = K_{54}^e + \int_{x_a}^{x_b} \frac{\bar{A}}{2} \frac{\partial w}{\partial x} \frac{\partial \psi_2}{\partial x} \frac{\partial \varphi_2}{\partial x} dx$$

$$T_{55}^e = K_{55}^e$$

$$T_{56}^e = K_{56}^e$$

$$T_{57}^e = K_{57}^e + \int_{x_a}^{x_b} \frac{\bar{A}}{2} \frac{\partial w}{\partial x} \frac{\partial \psi_2}{\partial x} \frac{\partial \varphi_3}{\partial x} dx$$

$$T_{58}^e = K_{58}^e + \int_{x_a}^{x_b} \frac{\bar{A}}{2} \frac{\partial w}{\partial x} \frac{\partial \psi_2}{\partial x} \frac{\partial \varphi_4}{\partial x} dx$$

$$T_{61}^e = K_{61}^e$$

$$T_{62}^e = K_{62}^e$$

$$T_{63}^e = K_{63}^e + \int_{x_a}^{x_b} \frac{\bar{C}_1}{2} \frac{\partial w}{\partial x} \frac{\partial \psi_2}{\partial x} \frac{\partial \varphi_1}{\partial x} dx$$

$$T_{64}^e = K_{64}^e + \int_{x_a}^{x_b} \frac{\bar{C}_1}{2} \frac{\partial w}{\partial x} \frac{\partial \psi_2}{\partial x} \frac{\partial \varphi_2}{\partial x} dx$$

$$T_{65}^e = K_{65}^e$$

$$T_{66}^e = K_{66}^e$$

$$T_{67}^e = K_{67}^e + \int_{x_a}^{x_b} \frac{\bar{C}_1}{2} \frac{\partial w}{\partial x} \frac{\partial \psi_2}{\partial x} \frac{\partial \varphi_3}{\partial x} dx$$

$$T_{68}^e = K_{68}^e + \int_{x_a}^{x_b} \frac{\bar{C}_1}{2} \frac{\partial w}{\partial x} \frac{\partial \psi_2}{\partial x} \frac{\partial \varphi_4}{\partial x} dx$$

$$T_{71}^e = K_{71}^e$$

$$T_{72}^e = K_{72}^e$$

$$T_{73}^e = K_{73}^e + \int_{x_a}^{x_b} \left\{ \bar{A} \left[\frac{\partial u}{\partial x} + \left(\frac{\partial w}{\partial x} \right)^2 \right] \frac{\partial \varphi_1}{\partial x} \frac{\partial \varphi_3}{\partial x} + \bar{C}_1 \frac{\partial \phi}{\partial x} \frac{\partial \varphi_1}{\partial x} \frac{\partial \varphi_3}{\partial x} \right. \\ \left. + (C_2 + \bar{B}_1) \left(\frac{\partial^2 w}{\partial x^2} \frac{\partial \varphi_1}{\partial x} \frac{\partial \varphi_3}{\partial x} + \frac{1}{2} \frac{\partial w}{\partial x} \frac{\partial \varphi_1}{\partial x} \frac{\partial^2 \varphi_3}{\partial x^2} \right) \right\} dx$$

$$T_{74}^e = K_{74}^e + \int_{x_a}^{x_b} \left\{ \bar{A} \left[\frac{\partial u}{\partial x} + \left(\frac{\partial w}{\partial x} \right)^2 \right] \frac{\partial \varphi_2}{\partial x} \frac{\partial \varphi_3}{\partial x} + \bar{C}_1 \frac{\partial \phi}{\partial x} \frac{\partial \varphi_2}{\partial x} \frac{\partial \varphi_3}{\partial x} \right. \\ \left. + (C_2 + \bar{B}_1) \left(\frac{\partial^2 w}{\partial x^2} \frac{\partial \varphi_2}{\partial x} \frac{\partial \varphi_3}{\partial x} + \frac{1}{2} \frac{\partial w}{\partial x} \frac{\partial \varphi_2}{\partial x} \frac{\partial^2 \varphi_3}{\partial x^2} \right) \right\} dx$$

$$T_{75}^e = K_{75}^e$$

$$T_{76}^e = K_{76}^e$$

$$T_{77}^e = K_{77}^e + \int_{x_a}^{x_b} \left\{ \bar{A} \left[\frac{\partial u}{\partial x} + \left(\frac{\partial w}{\partial x} \right)^2 \right] \frac{\partial \varphi_3}{\partial x} \frac{\partial \varphi_3}{\partial x} + \bar{C}_1 \frac{\partial \phi}{\partial x} \frac{\partial \varphi_3}{\partial x} \frac{\partial \varphi_3}{\partial x} \right. \\ \left. + (C_2 + \bar{B}_1) \left(\frac{\partial^2 w}{\partial x^2} \frac{\partial \varphi_3}{\partial x} \frac{\partial \varphi_3}{\partial x} + \frac{1}{2} \frac{\partial w}{\partial x} \frac{\partial \varphi_3}{\partial x} \frac{\partial^2 \varphi_3}{\partial x^2} \right) \right\} dx$$

$$T_{78}^e = K_{78}^e + \int_{x_a}^{x_b} \left\{ \bar{A} \left[\frac{\partial u}{\partial x} + \left(\frac{\partial w}{\partial x} \right)^2 \right] \frac{\partial \varphi_3}{\partial x} \frac{\partial \varphi_4}{\partial x} + \bar{C}_1 \frac{\partial \phi}{\partial x} \frac{\partial \varphi_3}{\partial x} \frac{\partial \varphi_4}{\partial x} \right. \\ \left. + (C_2 + \bar{B}_1) \left(\frac{\partial^2 w}{\partial x^2} \frac{\partial \varphi_3}{\partial x} \frac{\partial \varphi_4}{\partial x} + \frac{1}{2} \frac{\partial w}{\partial x} \frac{\partial \varphi_3}{\partial x} \frac{\partial^2 \varphi_4}{\partial x^2} \right) \right\} dx$$

$$T_{81}^e = K_{81}^e$$

$$T_{82}^e = K_{82}^e$$

$$T_{83}^e = K_{83}^e + \int_{x_a}^{x_b} \left\{ \bar{A} \left[\frac{\partial u}{\partial x} + \left(\frac{\partial w}{\partial x} \right)^2 \right] \frac{\partial \varphi_1}{\partial x} \frac{\partial \varphi_4}{\partial x} + \bar{C}_1 \frac{\partial \phi}{\partial x} \frac{\partial \varphi_1}{\partial x} \frac{\partial \varphi_4}{\partial x} \right. \\ \left. + (C_2 + \bar{B}_1) \left(\frac{\partial^2 w}{\partial x^2} \frac{\partial \varphi_1}{\partial x} \frac{\partial \varphi_4}{\partial x} + \frac{1}{2} \frac{\partial w}{\partial x} \frac{\partial \varphi_1}{\partial x} \frac{\partial^2 \varphi_4}{\partial x^2} \right) \right\} dx$$

$$T_{84}^e = K_{84}^e + \int_{x_a}^{x_b} \left\{ \overline{A} \left[\frac{\partial u}{\partial x} + \left(\frac{\partial w}{\partial x} \right)^2 \right] \frac{\partial \varphi_2}{\partial x} \frac{\partial \varphi_4}{\partial x} + \overline{C}_1 \frac{\partial \phi}{\partial x} \frac{\partial \varphi_2}{\partial x} \frac{\partial \varphi_4}{\partial x} \right. \\ \left. + (C_2 + \overline{B}_1) \left(\frac{\partial^2 w}{\partial x^2} \frac{\partial \varphi_2}{\partial x} \frac{\partial \varphi_4}{\partial x} + \frac{1}{2} \frac{\partial w}{\partial x} \frac{\partial \varphi_2}{\partial x} \frac{\partial^2 \varphi_4}{\partial x^2} \right) \right\} dx$$

$$T_{85}^e = K_{85}^e$$

$$T_{86}^e = K_{86}^e$$

$$T_{87}^e = K_{87}^e + \int_{x_a}^{x_b} \left\{ \overline{A} \left[\frac{\partial u}{\partial x} + \left(\frac{\partial w}{\partial x} \right)^2 \right] \frac{\partial \varphi_3}{\partial x} \frac{\partial \varphi_4}{\partial x} + \overline{C}_1 \frac{\partial \phi}{\partial x} \frac{\partial \varphi_3}{\partial x} \frac{\partial \varphi_4}{\partial x} \right. \\ \left. + (C_2 + \overline{B}_1) \left(\frac{\partial^2 w}{\partial x^2} \frac{\partial \varphi_3}{\partial x} \frac{\partial \varphi_4}{\partial x} + \frac{1}{2} \frac{\partial w}{\partial x} \frac{\partial \varphi_3}{\partial x} \frac{\partial^2 \varphi_4}{\partial x^2} \right) \right\} dx$$

$$T_{88}^e = K_{88}^e + \int_{x_a}^{x_b} \left\{ \overline{A} \left[\frac{\partial u}{\partial x} + \left(\frac{\partial w}{\partial x} \right)^2 \right] \frac{\partial \varphi_4}{\partial x} \frac{\partial \varphi_4}{\partial x} + \overline{C}_1 \frac{\partial \phi}{\partial x} \frac{\partial \varphi_4}{\partial x} \frac{\partial \varphi_4}{\partial x} \right. \\ \left. + (C_2 + \overline{B}_1) \left(\frac{\partial^2 w}{\partial x^2} \frac{\partial \varphi_4}{\partial x} \frac{\partial \varphi_4}{\partial x} + \frac{1}{2} \frac{\partial w}{\partial x} \frac{\partial \varphi_4}{\partial x} \frac{\partial^2 \varphi_4}{\partial x^2} \right) \right\} dx$$

Weight-efficiency is central in reducing the ecological footprint of the transport industry. Advances in manufacturing allow the development of shape-optimized assemblies such as lightweight corrugated panels, which can significantly reduce the structural weight without compromising safety or other service requirements. Their discrete modeling is, however, computationally inefficient in describing the stiffness and strength behavior in large models. Therefore, homogenized descriptions are preferred in certain stages of the design process. This dissertation tackles challenges in the homogenized modeling of corrugated sandwich beams. A non-classical model is utilized to describe underlying size effects, whereas scale transitions are embedded to describe progressive global and local buckling in lightweight assemblies. Parametric studies investigate the accuracy of the model and parameter sensitivity in the geometric failure mechanisms and size-dependent behavior.



ISBN 978-952-64-0445-5 (printed)

ISBN 978-952-64-0446-2 (pdf)

ISSN 1799-4934 (printed)

ISSN 1799-4942 (pdf)

Aalto University
School of Engineering
Department of Mechanical Engineering
www.aalto.fi

**BUSINESS +
ECONOMY**

**ART +
DESIGN +
ARCHITECTURE**

**SCIENCE +
TECHNOLOGY**

CROSSOVER

**DOCTORAL
DISSERTATIONS**